Entropy Changes of Charging Processes of Hard Carbon and Sodium Vanadium Phosphate Composite Electrodes for Sodium-Ion Batteries

Zur Erlangung des akademischen Grades eines

DOKTORS DER NATURWISSENSCHAFTEN

(Dr. rer. nat.)

von der KIT-Fakultät für Chemie und Biowissenschaften

des Karlsruher Instituts für Technologie (KIT)

genehmigte

DISSERTATION

von

M. Sc. Laurin Gregor Derr

1. Referent: Prof. Dr. Rolf Schuster
2. Referent: Prof. Dr. Helmut Ehrenberg

Tag der mündlichen Prüfung: 04.02.2026

Abstract

Sodium-ion batteries (SIBs) are considered to be the most promising alternative to lithium-ion batteries (LIBs), due to the broad abundance of sodium and the direct compatibility with existing LIB manufacturing structure. Hard carbon (HC) is commonly used as active material for the negative electrode in SIBs, since it allows for the reversible insertion/extraction of Na^+ ions at potentials below 1 V vs. Na/Na^+. Among other material classes, polyanionic compounds, such as $Na_3V_2(PO_4)_3$, are being investigated for the positive electrode. At a potential of around 3.4 V vs. Na/Na^+, two sodium ions can be electrochemically extracted per $Na_3V_2(PO_4)_3$ formula unit to form $Na_1V_2(PO_4)_3$. During charging and discharging of a SIB, processes occur within a wide range of time scales, from milliseconds to minutes or even hours. Understanding the thermodynamics of these processes, for example by time-resolved measurements of the concomitant entropy changes, can provide valuable insights into their underlying mechanisms. In this work, two distinct methods covering different timescales were employed to determine the entropy change of the charging/discharging processes of HC and carbon-coated $Na_3V_2(PO_4)_3/C$ (NVP/C). With electrochemical microcalorimetry, the reversibly exchanged heat is measured at a single electrode, which enables to resolve the entropy production with millisecond time resolution. With entropy profiling, i.e., measuring the temperature dependence of the equilibrium cell voltage, the cell reaction entropy was determined, which also contained contributions of slow relaxation processes on the minutes timescale.

For both, the sodiation of HC and the insertion of Na^+ ions into NVP/C, the reaction entropy of the processes at the single electrode was dominated by the positive entropy change caused by the desolvation of the Na^+ ions. The second contribution to the reaction entropy was the entropy change of the active material, which led to the variation of the reaction entropy with the state of charge (SoC). For the sodiation of HC, the variation of the reaction entropy with increasing SoC could be explained by adsorption of Na^+ ions, followed by intercalation of Na^+ ions into graphitic layers, and ultimately filling of the pores of HC with sodium. At SoCs below 20 %, the sodiation of HC and consequently the desolvation of the Na^+ ions was found to significantly slow down, coinciding with a reduced reaction entropy. For NVP/C, at SoCs below 10 % and above 80 %, the charging/discharging could be described by a solid solution-type depletion/filling of a single phase. In the potential plateau (10 % to 80 % SoC) in the discharging cycle, the constant reaction entropy indicated a first-order phase transition within a two-phase regime. However, in the charging cycle at identical SoCs, a variation of the the reaction entropy with the SoC was found. This possibly points toward the occurrence of an intermediate phase.

Zusammenfassung

Natrium-Ionen Batterien gelten aufgrund der hohen Verfügbarkeit von Natrium und der einfachen Integration in bestehende Produktionsprozesse für Lithium-Ionen Batterien als die vielversprechendste Alternative zu Lithium-Ionen Batterien. Für die negative Elektrode wird üblicherweise Hard Carbon (HC) verwendet, da Na^+ Ionen bei Potentialen unter 1 V vs. Na/Na^+ reversibel ein- bzw. ausgelagert werden können. Für die positive Elektrode werden unter anderem polyanionische Verbindungen wie z.B. $Na_3V_2(PO_4)_3$ untersucht. Aus $Na_3V_2(PO_4)_3$ kann durch die elektrochemische Extraktion von Na^+ Ionen bei einem Potential von etwa 3.4 V vs. Na/Na^+ $Na_1V_2(PO_4)_3$ gebildet werden. Beim (Ent-)Laden einer Natrium-Ionen Batterie finden Prozesse auf unterschiedlichen Zeitskalen, von Millisekunden bis hin zu Stunden, statt. Das Aufklären der Thermodynamik dieser Prozesse, etwa durch zeitaufgelöste Messungen der einhergehenden Entropieänderungen, liefert wichtige Einblicke in die zugrunde liegenden Mechanismen. Um die Entropieänderungen bei den Lade-/Entladeprozessen von HC und kohlenstoffbeschichtetem $Na_3V_2(PO_4)_3/C$ (NVP/C) zu bestimmen, wurden in der vorliegenden Arbeit zwei Methoden verwendet, die Prozesse auf unterschiedlichen Zeitskalen erfassen. Zum einen wurde mit Hilfe elektrochemischer Mikrokalorimetrie die reversibel ausgetauschte Wärme an einer einzelnen Elektrode gemessen, womit die Entropieproduktion millisekundenaufgelöst bestimmt werden konnte. Außerdem wurde über die Temperaturabhängigkeit der Gleichgewichtsspannung die Zellreaktionsentropie ermittelt, welche auch Beiträge von langsameren Relaxationsprozessen beinhaltete.

Die Reaktionsentropie der Ladeprozesse einer einzelnen HC bzw. NVP/C Elektrode war von der Entropiezunahme durch die Desolvatisierung der Na^+ Ionen bestimmt. Zusätzlich führte die Entropieänderung des Aktivmaterials zur Variation der Reaktionsentropie mit dem Ladezustand der Elektrode. Der Verlauf der Reaktionsentropie für den Ladeprozess von HC konnte mit ansteigendem Ladezustand der Adsorption von Na^+ Ionen, gefolgt von der Interkalation von Na^+ Ionen in die graphitischen Schichten und schließlich dem Füllen der Poren von HC mit Natrium zugeordnet werden. Bei Ladezuständen unter 20 % wurde ein deutlich verlangsamter Ladeprozess und dadurch eine langsame Desolvatisierung der Na^+ Ionen beobachtet, welche mit einer reduzierten Reaktionsentropie einherging. Der Ladeprozess von NVP/C bei Ladezuständen unter 10 % und über 80 % konnte mit einem Einlagerungsprozess in eine einzelne Phase beschrieben werden. Die konstante Reaktionsentropie im Potentialplateau (10 % bis 80 %) im Entladezyklus konnte mit einem Phasenübergang erster Ordnung zwischen zwei Phasen erklärt werden. Dagegen deutete die Variation der Reaktionsentropie bei gleichen Ladezuständen im Ladezyklus auf eine Zwischenphase hin.

Contents

1

Introduction

Batteries are an indispensable part of everyday life. We use lithium-ion batteries (LIBs) not only to run laptops and smartphones, but increasingly to drive electric vehicles and to store intermittently generated renewable energy. Recent projections indicate an exponential growth in LIB production - by 2030 a total global LIB production corresponding to 2.4 TWh yr^{-1} is estimated.[1] However, demand for critical raw materials for LIBs, such as Li, Ni, Co or Cu, could exceed supply in the near future.[1, 2] Therefore, alternative battery technologies are needed. Sodium-ion batteries (SIBs) are already being commercialized and are considered to be the most promising alternative to LIBs, due to several reasons. Sodium is cheap and abundant all over the world,[3] Al can be used in SIBs as current collector instead of the more expensive and less abundant Cu required in LIBs,[4] SIBs can be produced using the LIB manufacturing infrastructure,[2] and lastly, the working principle of LIBs and SIBs is very similar, which promotes the development of SIBs.[4]

A SIB consists of a negative composite electrode, an organic electrolyte solution and a positive composite electrode. During charging of a SIB, electric energy has to be provided by the external circuit. Na^+ ions are electrochemically extracted from the positive electrode and inserted into the negative electrode. While the ions are transported through the electrolyte solution, the electrons flow through the external circuit from the positive electrode to the negative electrode. During discharging the reverse (spontaneous) process occurs. The resulting electric current in the external circuit can be used to power electric devices.

Hard carbon (HC) is commonly used as active material for the negative electrode in SIBs, since Na^+ ions can reversibly be inserted into or extracted from HC within a potential range of 1 to 0 V vs. Na/Na^+. HC denotes non-graphitizable carbon consisting of pseudo-graphitic domains, defects and pores and can be synthesized by pyrolysis of biomass or polymers.[5] Despite the extensive use of HC in SIBs, there is still a lack of comprehensive understanding of the underlying sodium storage mechanism, including at which potential and to which extent sodium is stored at the different sites (surface defects, layers or pores). For the positive electrode three different material classes are investigated and commercialized in SIBs: layered oxides, Prussian blue analogues and polyanionic compounds.[6] A typical representative of the polyanionic compounds is $Na_3V_2(PO_4)_3$ (NVP). It shows a high cycling stability, which is ascribed to the strong covalent bonds leading to a robust network within the material.[7] At a potential of around 3.4 V vs. Na/Na^+, two sodium ions can be electrochemically extracted per $Na_3V_2(PO_4)_3$ formula unit to form $Na_1V_2(PO_4)_3$.[8] However, the commonly accepted two-phase mechanism between $Na_3V_2(PO_4)_3$ and $Na_1V_2(PO_4)_3$ was recently challenged, since with *operando* synchrotron X-ray diffraction (XRD) an intermediate phase $Na_2V_2(PO_4)_3$ could be resolved during charging/discharging.[9] For the transport of the Na^+ ions between both electrodes, an organic electrolyte solution is used. It is composed of a conductive salt dissolved in one or more solvents. The salts most commonly employed in SIBs are $NaPF_6$ and $NaClO_4$. Typical solvent systems are esters and ethers, such as ethylene carbonate (EC), propylene carbonate (PC) or diglyme.

Although the general working principle of a SIB is fairly simple, in an actual cell considerably more processes occur within a wide range of time scales, from milliseconds to minutes or even hours. For instance, charging/discharging of the electrical double layer is a rather fast process, whereas the diffusion of Na^+ ions in the composite electrode or in the particles of active material is known to be a slow process. The time constants of other processes, such as charge transfer reactions or the diffusion of Na^+ ions in the electrolyte solution, fall somewhere in between. Many of the processes taking place in SIBs are not yet fully understood. Among others, the kinetics of the charge transfer reactions, the solvation/desolvation of Na^+ ions, or the formation and dissolution of the solid electrolyte interphase (SEI), which is formed on the HC electrode due to decomposition of the electrolyte solution. Understanding such processes is crucial for the development of new materials for SIBs, in order to improve the performance of SIBs, including fast charging, long lifetime or high energy density.

Electrochemical processes on different timescales can, e.g., be resolved with electrochemical impedance spectroscopy (EIS). As with other electrochemical methods, EIS measures the electrode potential as a function of current or charge. Since the equilibrium cell voltage is correlated with the free cell reaction enthalpy $\Delta_\mathrm{R} G_\mathrm{cell}$, electrochemical methods allow only to obtain information about $\Delta_\mathrm{R} G_\mathrm{cell}$. Another important thermodynamic quantity of electrochemical reactions is the reaction entropy $\Delta_\mathrm{R} S$. The reaction entropy of electrochemical processes can provide valuable insights into their underlying mechanisms. For instance, information about the solvation structure of the Na^+ ions or phase changes of the electrochemically active materials might be obtained. These insights can be expanded by measuring the entropy production over time.

In this work, the entropy change upon charging/discharging of HC and carbon-coated $Na_3V_2(PO_4)_3/C$ (NVP/C) is measured. The main questions, addressed for both materials, are: What are the contributions to the reaction entropy of charging/discharging, and what can be learned from the variation of the reaction entropy with the state of charge (SoC) about the charging mechanism? In addition, the possible influence of the kinetics on the entropy production will be investigated by measuring the reaction entropy with two distinct methods covering different timescales. With electrochemical microcalorimetry the reversibly exchanged heat upon electrochemical reactions is directly measured at a single electrode to determine the reaction entropy. This method enables millisecond time resolution of the entropy production, but is limited to processes that complete within about a second. In the second method, which is commonly referred to as entropy profiling, the temperature dependence of the equilibrium cell voltage is measured to obtain the cell reaction entropy. This method requires the cell to be in an equilibrium state and thus, also slow relaxation processes have to be completed. In conventional entropy profiling experiments the temperature variations take more than ten minutes. In contrast, in this work, temperature changes on the timescale of several seconds are applied to coin cells. With this approach the kinetics of the charging/discharging processes can additionally be accessed through the cell voltage response to the fast temperature changes.

For the sodiation of HC, the variation of the reaction entropy with the SoC is employed to obtain information about the sodiation mechanism, i.e., at which potential and to which extent sodium is stored at different sites. The entropy measurements on different timescales provide insight into the role of the desolvation of the Na^+ ions upon the sodiation of HC. Furthermore, the kinetics of the sodiation of HC can be accessed. In addition, X-ray photoelectron spectroscopy (XPS) is used to investigate the stability of the SEI, which is formed on the HC electrode due to decomposition of the electrolyte solution.

For the charging/discharging of carbon-coated NVP/C, the reaction entropy is determined with electrochemical microcalorimetry. The variation of the reaction entropy with the SoC allows conclusions to be drawn about the phase transitions, which take place in the NVP when its composition is changed due to charging/discharging. In addition, the cell reaction entropy of a complete SIB consisting of a HC and a NVP/C electrode is determined with entropy profiling. This allows to compare the results found for the charging/discharging of the HC and the NVP/C electrode, in order to evaluate which electrode reaction is dominating the cell reaction entropy and its variation with the SoC.

The work is structured as follows. In chapter 2 the theoretical foundations of entropy profiling, electrochemical microcalorimetry and XPS are provided. Thereafter, the experimental details are described in chapter 3. The results for the sodiation of HC and the charging of NVP/C are presented in the two main chapters 4 and 5, respectively.

2

Theoretical Foundations

Already in the 19th century the fields of electrochemistry and thermodynamics were treated together. It was, e.g., found by Gibbs [10] and Helmholtz [11] that during an electrochemical reaction heat is exchanged between the electrochemical cell and the surrounding. Along with this Helmholtz introduced the term "freie Energie" to describe the electrical work of an electrochemical reaction at constant pressure and temperature. Around the same time, Bouty observed temperature changes at single electrodes by using copper-plated thermometers as electrodes.[12] He found that the electrochemical deposition of Cu leads to cooling and its stripping leads to heating of the respective electrode. Analogous to the Peltier effect, which arises at the interface between two metals, he termed this phenomenon electrochemical Peltier effect. Its theoretical foundations were laid later by Lange *et al.* [13] and Eastman [14], and further developed by Agar.[15]

In the following chapter the theoretical foundations for the different experimental approaches used in this work are given. First, the thermodynamics of an electrochemical cell is shortly introduced. Then, the reversible and irreversible contributions to the heat exchange during an electrochemical half-cell reaction are explained together with the electrochemical Peltier effect. Finally, a brief introduction to the theory of XPS is provided.

2.1 Thermodynamics of an Electrochemical Cell

Consider an exemplary electrochemical cell consisting of a right (R) and a left (L) half-cell with the following electrode reactions.

$$\begin{aligned} \textbf{R:}\ & \mathrm{M^+ + e^- \rightleftharpoons M} \\ \textbf{L:}\ & \mathrm{B^+ + e^- \rightleftharpoons B} \\ \textbf{R-L:}\ & \mathrm{M^+ + B \rightleftharpoons M + B^+} \end{aligned}$$

The equilibrium cell voltage E_0 is given by the difference between both equilibrium electrode potentials ϕ_0, i.e., $E_0 = \phi_0(R) - \phi_0(L)$. From E_0, the free cell reaction enthalpy $\Delta_\mathrm{R} G_\mathrm{cell}$, and from its temperature dependence, the cell reaction entropy

$\Delta_\mathrm{R} S_\mathrm{cell}$ can be obtained.[16]

$$\Delta_\mathrm{R} G_\mathrm{cell} = -zFE_0 \tag{2.1}$$

$$\Delta_\mathrm{R} S_\mathrm{cell} = -\left(\frac{\partial \Delta_\mathrm{R} G_\mathrm{cell}}{\partial T}\right)_{p,n_i} = zF\left(\frac{\partial E_0}{\partial T}\right) \tag{2.2}$$

Herein F is the Faraday constant and z is the number of transferred electrons in the reaction.

It should be noted that experimentally only voltages, i.e., potential differences, can be measured. Still, the electrode potential of a working electrode (WE) can be accessed by measuring the voltage against an additional reference electrode (RE), which doesn't carry current and has a stable electrode potential. In this work such a three-electrode configuration was used in the microcalorimetric experiments and consequently the potential of the WE vs. the RE is reported. For the temperature step experiments a two-electrode configuration was used and consequently the cell voltage is reported.

2.2 Heat of Electrochemical Half-Cell Reactions

2.2.1 Reversible Heat Contributions

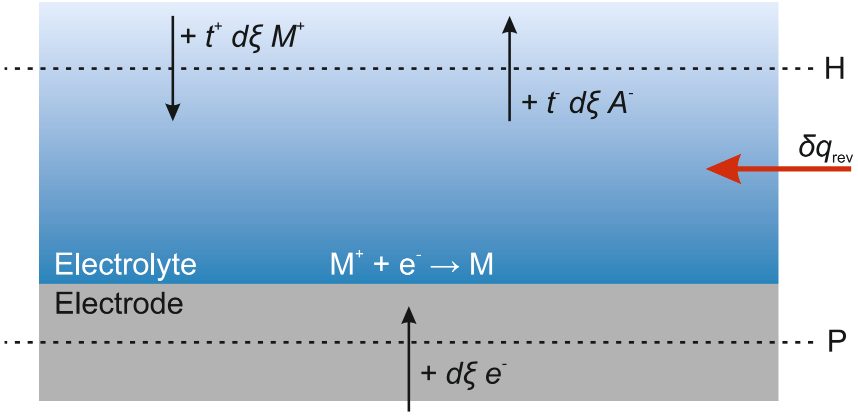

Figure 2.1: Half-cell reduction reaction at the electrode-electrolyte interface restricted by the Hittorf reference plane H and the plane P. The figure was adopted in a modified form from Gottfried *et al.*[17]

The reversibly exchanged heat during an electrochemical half-cell reaction can be described with the electrochemical Peltier effect. In the subsequent section, a formula for the Peltier heat will be derived, following the description of Agar,[15] Gottfried and Schuster.[17]

The half-cell reduction reaction $\mathrm{M}^{+} + \mathrm{e}^{-} \longrightarrow \mathrm{M}$, shown schematically in Figure 2.1, is considered. M^{+} is reduced at the electrode to M. The electrolyte solution contains anions A^- and cations M^+. The electrode-electrolyte interface is confined in the electrode by the plane P allowing electron transport and the so-called Hittorf reference plane H in the electrolyte. The plane H is chosen far enough from the electrode, so that bulk electrolyte solution properties can be assumed. During the reaction, the plane H can be moved to keep the amount of solvent between both planes constant.

At constant temperature and pressure, the reaction is driven by an infinitesimally small current, which leads to a change of the reaction variable $d\xi$. Thus, $d\xi$ M^+ are reduced with $d\xi$ electrons to M. To ensure charge neutrality $t^+d\xi$ cations M^+ enter and $t^-d\xi$ anions A^- leave the interface through the Hittorf plane. The transference numbers t^+ and t^- describe the contribution of the respective ions to the electric current in the electrolyte solution. The change of the entropy dS of the interface upon the reaction can be described with the molar entropies s_{M^+}, s_M, and s_{A^-}.

$$dS = (s_M - s_{M^+} + t^+ s_{M^+} - t^- s_{A^-})d\xi \tag{2.3}$$

This entropy change is caused by the heat exchange with the surrounding δq_{rev} and the transport of electrons and ions across the planes H and P. The heat, which is exchanged with the surrounding during the reversible process, is called Peltier heat and is usually normalized to the reaction conversion to yield the molar Peltier heat Π.

$$\Pi = \frac{\delta q_{\mathrm{rev}}}{d\xi} = q_{\mathrm{rev}} \tag{2.4}$$

In the following the reversibly exchanged molar heat q_{rev} is used synonymously with the molar Peltier heat Π. Its entropy contribution can be readily calculated to be $\frac{q_{\mathrm{rev}}}{T}d\xi = \frac{\Pi}{T}d\xi$. The common sign convention is used in this work, so that $\delta q > 0$ means heat uptake and $\delta q < 0$ heat release of the system.

Additionally, the transport of charge carriers across the boarders of the half-cell contribute to the entropy change. The transported entropy $\bar{\bar{S}}_i$ is composed of the respective molar entropy s_i and Eastman's entropy of transfer $\hat{s}_i$.

$$\bar{\bar{S}}_i = s_i + \hat{s}_i \tag{2.5}$$

Eastman's entropy of transfer can be explained with the influence of ions on the surrounding solvent molecules. Ions can either be structure-making (entropy decrease) or structure-breaking (entropy increase). When a structure-making ion is moved through a solution, heat is librated ahead and absorbed behind it. This leads to transport of heat through the solution, quantified as molar heat of transport $\hat{Q}_i$, which is used to calculate Eastman's entropy of transfer $\hat{s}_i = \frac{\hat{Q}_i}{T}$.

The total entropy change for the example shown in Figure 2.1 is the sum of the

Peltier heat and the transported entropy.

$$dS = \left(t^{+} \bar{\bar{\bar{S}}}_{M^{+}} - t^{-} \bar{\bar{\bar{S}}}_{A^{-}} + \bar{\bar{\bar{S}}}_{e^{-}} + \frac{\Pi}{T} \right) d\xi \tag{2.6}$$

The entropy change calculated in equation 2.3 and 2.6 must be equal, since the entropy is a state variable. By combining these equations, it can be shown that the Peltier heat is composed of the half-cell reaction entropy $\Delta_{\mathrm{R}} S$ and the entropy change $\Delta_{\mathrm{T}} S$ caused by the transport of the ions, which is called entropy of transport in the following.

$$\frac{\Pi}{T} = (s_M - s_{M^{+}} - s_{e^{-}}) - (t^{+} \hat{s}_{M^{+}} - t^{-} \hat{s}_{A^{-}} + \hat{s}_{e^{-}}) = \Delta_{\mathrm{R}} S - \Delta_{\mathrm{T}} S \tag{2.7}$$

This seems to be counterintuitive, since $T \Delta_{\mathrm{R}} S$ should be equal to the heat reversibly exchanged with the surrounding by definition. But when the entropy of transport is rephrased as an additional reversible heat exchange q_{trans}, it can match the classical thermodynamic description.

$$\Delta_{\mathrm{R}} S = \frac{q_{\mathrm{rev}} + q_{\mathrm{trans}}}{T} = \frac{\Pi}{T} + \Delta_{\mathrm{T}} S \tag{2.8}$$

Neglecting the small influence of $\hat{s}_{e^{-}}$,[15] the entropy of transport can be calculated with the charge number z_i, t_i and $\hat{Q}_i$ of the respective ions.

$$\Delta_{\mathrm{T}} S = \frac{z}{T} \sum_i \frac{t_i \hat{Q}_i}{z_i} \tag{2.9}$$

Since molar heats of transport are not reported for non-aqueous electrolyte solutions, they can only be estimated. To do so, Agar assumed a spherically symmetrical ion at infinite dilution and a solvent, which behaves as a simple dielectric.[15] Following this approach and assuming additionally that the Stokes radius r_s is equal to the nearest distance between the ion and a solvent molecule, it can be found in SI units that

$$\hat{Q}_i = -\frac{N_A e^2 z_i^2 T}{16 \pi \varepsilon_0 r_s \varepsilon_r} \frac{\partial \varepsilon_r}{\partial T} \tag{2.10}$$

with the Avogadro constant N_A, the elementary charge e, the vacuum permittivity ε_0, the relative permittivity ε_r and the Stokes radius of the ion r_s. The Stokes radius can be calculated with the Boltzmann constant k_B, the viscosity of the electrolyte solution η and the diffusion constant of the ion D_i.

$$r_{s,i} = \frac{k_B T}{6 \pi \eta D_i} \tag{2.11}$$

2.2.2 Irreversible Heat Contributions

In order to reach measurable temperature changes of the electrode-electrolyte interface, it is necessary to drive the electrochemical reaction with a considerable current. To do so, an overpotential η, which is the difference between the applied and the equilibrium half-cell potential, is needed. This leads to heating, irrespective of the sign of the overpotential.

$$\delta q_{\mathrm{pol}} = -zF|\eta|d\xi \tag{2.12}$$

Furthermore the current flow through the electrolyte solution leads to Joule heating. It is dependent on the resistance of the electrolyte solution R, the current i and the amount of time dt, in which current is flowing.

$$\delta q_{\mathrm{Joule}} = -Ri^2dt \tag{2.13}$$

With the Peltier heat, the overpotential heat and the Joule heat, the total heat exchanged with the surrounding during an electrochemical half-cell reaction can be expressed.

$$\delta q = \Pi d\xi - zF|\eta|d\xi - Ri^2dt \tag{2.14}$$

2.3 X-ray Photoelectron Spectroscopy

With XPS the electronic state of a material can be probed. It is based on the photoelectric effect, which was first found by Hertz,[19] and later described by Einstein.[20] The measurement principle is shown in Figure 2.2. The sample is irradiated with X-ray photons with a specific energy $E = h\nu$. This leads to the emission of core level electrons, which have to overcome the binding energy E_{bind} (referenced to the Fermi level E_{F}) and the work function of the sample Φ_{sample}. The remaining energy is converted into kinetic energy, which can be measured with a spectrometer. Since the spectrometer is electrically connected to the conductive sample, the Fermi levels align. The work function of the sample and the spectrometer might differ, so that the measured kinetic energy is dependent on Φ_{spec} and not on Φ_{sample}. When $h\nu$, $E_{\mathrm{kin,spec}}$ and Φ_{spec} are known, the binding energy can be calculated.[21]

$$E_{\mathrm{bind}} = h\nu - E_{\mathrm{kin,spec}} - \Phi_{\mathrm{spec}} \tag{2.15}$$

Since photoelectrons of different core levels are emitted when using X-ray photons with an energy $h\nu > E_{\mathrm{bind}} + \Phi_{\mathrm{spec}}$, the elementary composition of the sample can be probed. Due to the short inelastic mean free path (IMFP) of photoelectrons in solids, only the surface of the sample (5 nm to 10 nm) is probed. Siegbahn *et al.*

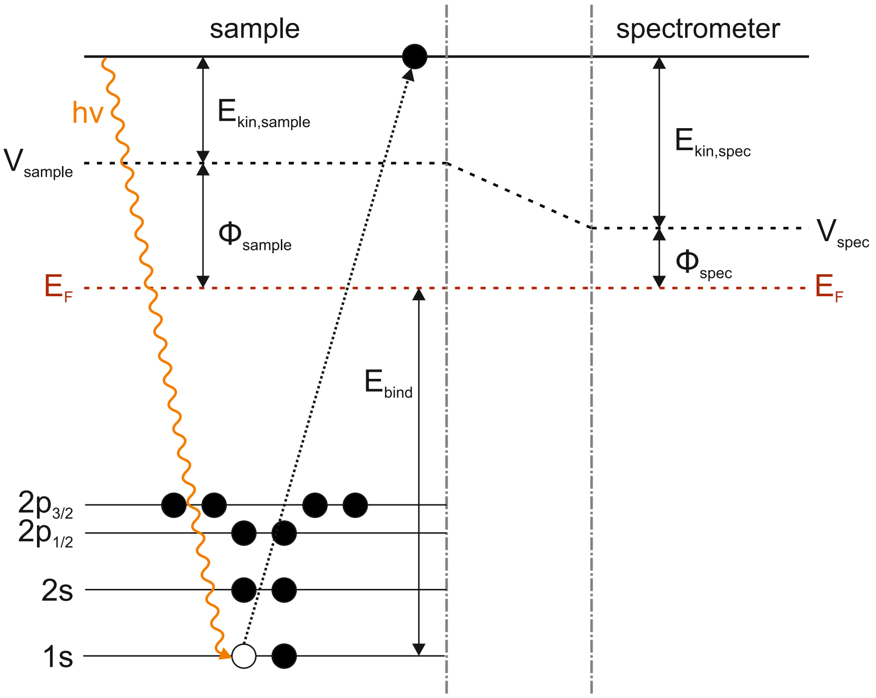

Figure 2.2: Illustration of the energy levels in the sample and the spectrometer adopted in a modified form from Källquist.[18] The conductive sample and the spectrometer are electrically connected, so that the Fermi levels E_F are aligned.

discovered that E_{bind} is not only dependent on the element and the specific core level, but can vary dependent on its local chemical environment and its oxidation state.[22] This allows, e.g., to differentiate between different carbon atoms within an organic molecule by probing the C 1s level.

3

Experimental

In the previous chapter it was shown that the reaction entropy of an electrochemical reaction can either be accessed by the temperature-dependence of the equilibrium cell voltage or the heat, which is evolved during an electrochemical reaction. With such kind of measurements electrochemical metal deposition reactions from aqueous electrolyte solutions were already investigated in the 1880s.[13] Thermocells, in which the temperature of one electrode is kept constant and the other one is changed, were used to determine the Peltier heat of the half-cell from the potential difference.[15] Alternatively, the heat flux caused by an electrochemical reaction in a half-cell was measured directly with calorimetry. With the advent of rechargeable LIBs almost one hundred years later, entropy measurements were, e.g., used by Dahn *et al.* to investigate insertion-type battery electrode materials. By changing the temperature of a Li|$LiTiS_2$ cell and measuring the voltage changes, he yielded the cell reaction entropy.[23] He also applied a calorimetric approach, where the complete battery cell was immersed in a calorimeter.[24]

For the mentioned calorimetric approaches rather high reaction conversions were needed to obtain measurable temperature changes. This can be overcome with the electrochemical microcalorimeter described in chapter 3.1, which allows the measurement of heat evolution on the order of µJ corresponding to electrochemical reaction conversions below a few percent of a metal monolayer. Furthermore an experimental setup for the measurement of the temperature coefficient of the equilibrium cell voltage of coin cells with fast temperature steps is presented in chapter 3.2. Lastly, the preparation of the used electrodes and electrolyte solutions and the experimental details of the XPS study are described.

3.1 Electrochemical Microcalorimetry

Electrochemical half-cell reactions lead to heat uptake or release at the electrode-electrolyte interface, as described in detail in chapter 2.2. To measure the heat evolution at low reaction conversions, an electrochemical microcalorimeter was developed and improved over several years in the group of Rolf Schuster. The main principle remained the same since the first publication in 2007.[25] The temperature change of a WE upon short electrochemical pulses is measured at its backside with a pyroelectric sensor. While in the beginning a polyvinylidene fluoride (PVDF) foil was used as pyroelectric sensor,[25, 26] it was later replaced by a $LiTaO_3$ single crystal to increase the sensitivity.[27] The herein used and described microcalorimeter is

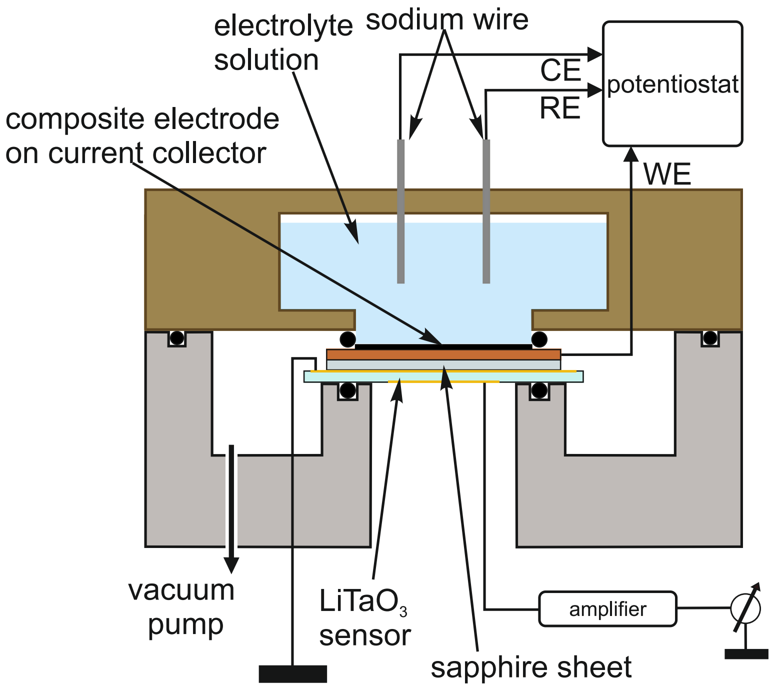

Figure 3.1: Schematic representation of the used electrochemical microcalorimeter.

based on the modifications of Karcher, which enabled measurements of non-aqueous systems in the absence of O_2 and H_2O in an Ar-containing glovebox.[28, 29]

3.1.1 Experimental Setup

The electrochemical microcalorimeter is shown schematically in Figure 3.1. Its centerpiece is the sensor-electrode stack consisting of a 25 µm thick $LiTaO_3$ single crystal (10 mm x 10 mm, DIAS Infrared) used as temperature sensor, a 50 µm thick sapphire sheet (Kyburz Sapphire) and the WE. $LiTaO_3$ shows pyroelectricity, due to its polar point symmetry.[30] Upon changing its temperature, the surface charge of the crystal changes, which can be measured after amplification. A thin layer of 2 nm Cr and 200 nm Au is vapor deposited onto each side of the crystal, so that the temperature sensor can be electrically contacted. Pyroelectric materials also show piezoelectricity. Thus, mechanical deformation of the sensor, e.g., caused by electrostriction can disturb the measurement.[25–27] To reduce the mechanical deformation of the sensor, a stiff sapphire sheet is placed in between the WE and the temperature sensor. To enhance the thermal conductivity of the sensor-electrode stack, vacuum pump oil is applied between the layers. Additionally, the middle compartment is evacuated to remove the air between the WE, sapphire sheet and the temperature sensor (10^{-1} mbar to 10^{-2} mbar). Thereby, the sensor-electrode stack is pressed together by the outer air pressure. In this work either a HC composite electrode, a NVP/C composite electrode or a dendritic Cu foil was used as WE (for details see chapter

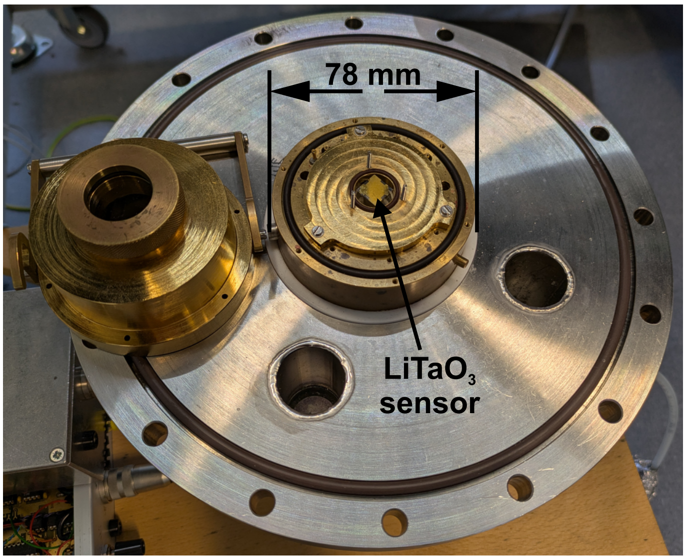

Figure 3.2: Microcalorimeter brass block (without the electrochemical cell) embedded in the stainless-steel flange used for the connection to the glovebox. On the left side the brass lid can be seen.

3.3.1). The WE is contacted from the top side with a Cu ring and a Cu spring and is grounded to prevent any crosstalk affecting the sensor signal. In the Cu ring a Perlast® O-ring (5 mm diameter) seals the electrochemical cell, which is mounted on top. The cell is made out of polyether ether ketone (PEEK), has a volume of 0.5 mL and restricts the electrochemically active geometric area to about 0.2 cm^2. The preparations of the electrolyte solutions used in this work are described in chapter 3.3.2. As counter electrode (CE) and RE 1 mm diameter Na wires (99.95 %, Alfa Aesar) are used. They are prepared by extrusion from a glass syringe, described in detail by Karcher.[28] To avoid electrolyte evaporation during the experiment the complete cell is closed and the CE and the RE are fed through the lid.

The microcalorimeter is mounted in a brass block, which is embedded into a stainless-steel flange (see Figure 3.2). This allows to attach the microcalorimeter to a glovebox (O_2 and H_2O < 1 ppm) from below. The typical workflow of setting up the microcalorimeter starts with assembling the sensor-electrode stack, the contacts of the WE and the bottom part of the PEEK cell outside of the glovebox. Thereafter, the flange is attached to the glovebox and vacuum is applied in the complete load-lock chamber for at least 1 h to avoid any water residues. After several repetitions of applying vacuum in the lock chamber and flushing it with the atmosphere of the glovebox, it can be opened inside the glovebox. The respective electrolyte solution is filled in the cell and the freshly prepared Na wires are attached and electrically connected by pressing the Na metal onto stainless steel pins. The brass block can be closed with a brass lid, which allowed to detach the microcalorimeter flange from the glovebox while maintaining the O_2 and H_2O free atmosphere around the electrochemical cell. This was, e.g., used for the laser pulse measurements described in chapter 3.1.2 and reduces the noise of the sensor signal, which is mainly caused by the gas circulation inside the glovebox. Detaching the microcalorimeter flange was not feasible for the experiments with the battery electrodes (which took several days), because leaving the microcalorimeter outside of the glovebox for several hours led to uncommon charging/discharging behavior most likely from increasing O_2 and H_2O content. For this reason the experiments with battery electrodes were performed inside the glovebox. For the experiments with the NVP/C composite electrodes, an additional feature was implemented, which stopped the gas circulation inside the glovebox automatically during the microcalorimetric pulse measurements to reduce background noise.

After the experiment, the microcalorimeter is completely disassembled and only the sensor is left in the brass block (as shown in Figure 3.2). All parts, which were in contact with the electrolyte solution, are cleaned in an ultrasonic bath in ultrapure water (18.2 MΩcm, Sartorius Arium) and subsequently boiled in ultrapure water before they are left to dry at 100 °C for more than 12 h.

The experimental control, data acquisition and data evaluation is performed with Igor Pro® from Wavemetrics®. A detailed block diagram of the setup is shown in the appendix in Figure C.1. The main components are two data acquisition boards from NI™ used to input and output the signals, a charge amplifier to measure the surface charge of the $LiTaO_3$ sensor and a potentiostat. The potentiostat was developed by Schuster and allows to either control the potential between the WE and the RE (potentiostatic mode), control the current flowing between the WE and the CE (galvanostatic mode) or measure the open circuit voltage (OCV).

3.1.2 Microcalorimetric Pulse Measurements

In chapter 2.2 it was shown that there are different contributions to the heat exchanged during an electrochemical half-cell reaction. They have to be separated in order to determine the reaction entropy. While the Peltier heat and the polarization heat are produced at the electrode-electrolyte interface, the Joule heat is produced along the complete distance between the WE and the CE in the electrolyte solution. Since the thin sensor-electrode stack has a small heat capacity and a higher heat conductivity than the electrolyte solution, the sensor equilibrates thermally fast with the electrode-electrolyte interface. The Joule heat in contrast is transferred much slower through the electrolyte solution and can be neglected when the electrochemical reaction is only driven within a short period of time. Thus, short (10 ms) electrochemical pulses are used, so that it can be assumed that the measured heat consists only of the Peltier heat and the polarization heat.[26] In the following, an example of such microcalorimetric pulse measurements is presented and the separation of the remaining two heat contributions is explained.

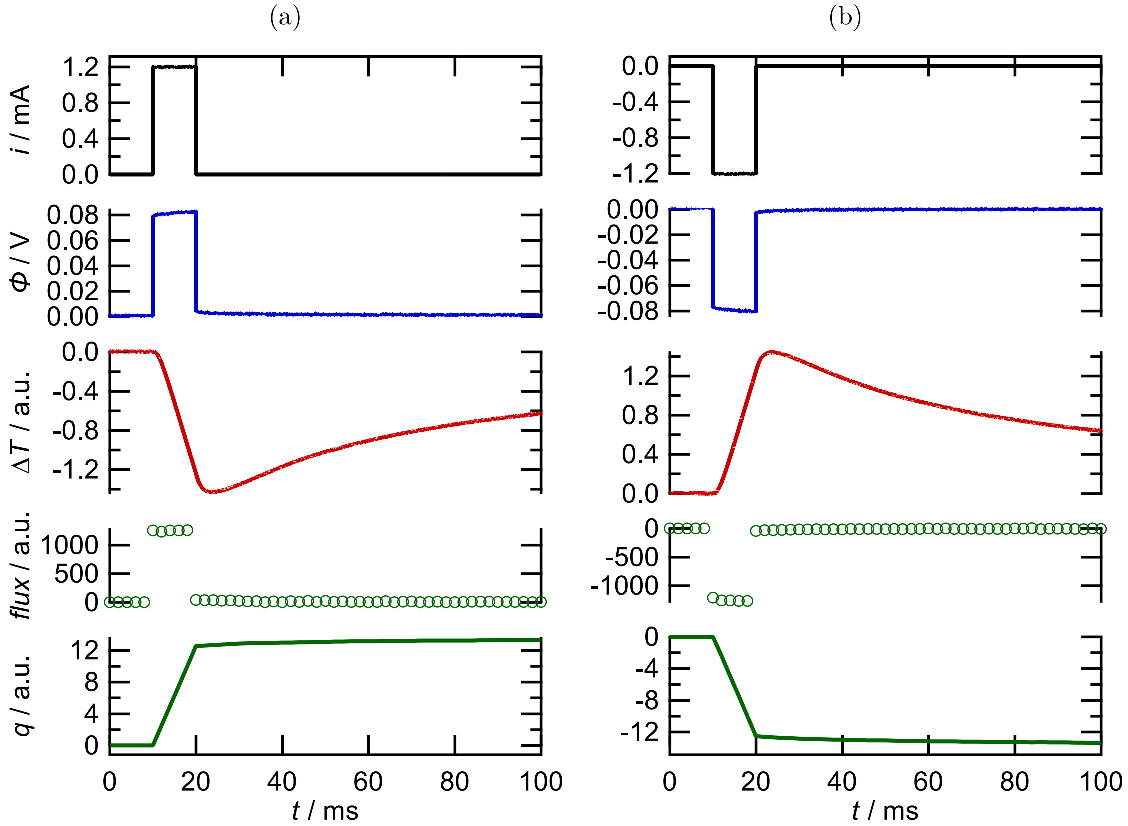

Figure 3.3: Current i, potential ϕ and temperature ΔT transients and the heat flux and the heat q resulting from a 10 ms (a) positive and (b) negative current pulse of a gold-plated dendritic Cu electrode in 0.1 M $K_3[Fe(CN)_6]/K_4[Fe(CN)_6]$ aqueous electrolyte solution.

In Figure 3.3 the measured (current, potential and temperature) and the calculated (heat flux and heat) signals resulting from a 10 ms positive and negative current pulse of a gold-plated dendritic Cu electrode in 0.1 M $K_3[Fe(CN)_6]/K_4[Fe(CN)_6]$ aqueous electrolyte solution are shown. During the positive current pulse (oxidation of Fe^{2+}) the temperature decreases and reaches a minimum at $t = 23$ ms, before it relaxes back to the initial temperature. Reversed behavior can be seen for the negative current pulse (reduction of Fe^{3+}), indicating a highly reversible reaction as expected. Still, it remains unclear why the minimum or maximum appears some milliseconds after the current pulse is stopped. It can be a result of delayed heat transfer through the sensor-electrode stack or of heat inputs from a slow or a subsequent reaction. To distinguish between those, the temperature transient is disentangled with the thermal response function of the microcalorimeter to obtain the heat flux and subsequently the heat.

Since heat conduction is generally described by a parabolic partial differential equation, temporally separated heat inputs add up to the measured temperature transient. This allows to reconstruct the measured temperature transient $T(t)$ with a sum of thermal response functions $P(t)$ resulting from a short and defined heat input by adjusting their respective amplitudes a_i.[31]

$$T(t) = \sum_{i=0}^{n} a_i P(t - i\Delta t) \tag{3.1}$$

The thermal response function is obtained by irradiation of the WE with laser pulses ($\Delta t = 2\,\mathrm{ms}$) from a blue laser diode (405 nm, CS4050205M, Laser Components). It has to be measured in every experiment, as it depends on the used WE as well as the assembly of the sensor-electrode stack. The amplitudes correspond to the heat flux and they can be summed up to obtain the exchanged heat with a time resolution of $\Delta t = 2\,\mathrm{ms}$. See Figure C.3 in the appendix for an illustration of a proof of concept experiment, in which the thermal responses to 10 ms laser irradiation on two different WEs were disentangled with the respective thermal response to 2 ms laser irradiation. In the above introduced example (Figure 3.3) significant heat flux (green circles) is only observed during the current pulse and the heat (green line) increases linearly from $t = 10\,\mathrm{ms}$ to $t = 20\,\mathrm{ms}$. This means that the probed electrochemical reaction and its heat input are fast and it is the delayed heat transfer through the sensor-electrode stack, which causes the shift of the temperature maximum or minimum in this example.
With the charge in the external circuit Q the extent of reaction can be calculated.

$$d\xi = -\frac{dQ}{zF} \tag{3.2}$$

Note here, that in this work all values are given in cathodic direction. The molar heat q_m, consisting of the Peltier heat and the polarization heat, is obtained by dividing the heat by the extent of reaction.

$$q_\mathrm{m} = \frac{\delta q}{d\xi} = \Pi + zF\eta \tag{3.3}$$

By determining the molar heat upon pulses with different positive and negative amplitudes, i.e., overpotentials, starting from the same potential, the Peltier heat can be obtained by interpolation to zero overpotential (see, e.g., Figure 4.6).

3.1.3 Calibration

The electrochemical microcalorimeter has to be calibrated after every experiment, since every sensor-electrode stack assembly shows a different thermal response. To do so a reaction with a known Peltier heat is measured after the experiment and a calibration factor is calculated. In general, the redox reaction of $\mathrm{Fe}^{2+}/\mathrm{Fe}^{3+}$ in $0.1\,\mathrm{M}$ $\mathrm{K_3[Fe(CN)_6]/K_4[Fe(CN)_6]}$ aqueous electrolyte solution, for which Boudeville measured $-45.1\,\mathrm{kJ\,mol^{-1}}$, is used.[32] In the case of the HC composite electrodes a different calibration reaction was employed, which is described in the following.

Calibration of the Microcalorimetric Experiments with HC

Since the binder of the HC composite electrodes was soluble in water, the aqueous Fe^{2+}/Fe^{3+} solution couldn't be used for the calibration of the microcalorimeter in these experiments. Similar problems were already faced by Schmid, who performed microcalorimetric experiments of Li intercalation into graphite.[33] He tried, e.g., to use ferrocene, which is soluble in non-aqueous electrolyte solutions, as redox pair, but the Peltier heat of the electrochemical redox reaction of ferrocene was too low. Herein, two different redox pairs were tested for their application as calibration reaction. The first one was a bipyridine complex with Ru(II). This idea was dropped, as no stable equilibrium state, i.e., no stable OCV, could be achieved. The other one was the organic redox molecule 2,5-di-tertbutyl-1,4-bis(methoxyethoxy)benzene (DBBB), which showed promising behavior (reversible electrochemical reaction, high Peltier heat) in a test experiment with an Au electrode, but this behavior couldn't be reproduced on the HC composite electrode. This might be a general problem, because the calibration has to be conducted after the experiment, where the HC composite electrode is covered with an SEI, which reduces the electronic conductivity of the electrode surface significantly.[34] To circumvent this problem, the electrochemical Na metal deposition reaction, which was measured with electrochemical microcalorimetry by Karcher *et al.* with 1 M $NaClO_4$/PC and 1 M $NaPF_6$/diglyme electrolyte solution,[29] was used as an *in situ* calibration. The experimental procedure is described in the following.

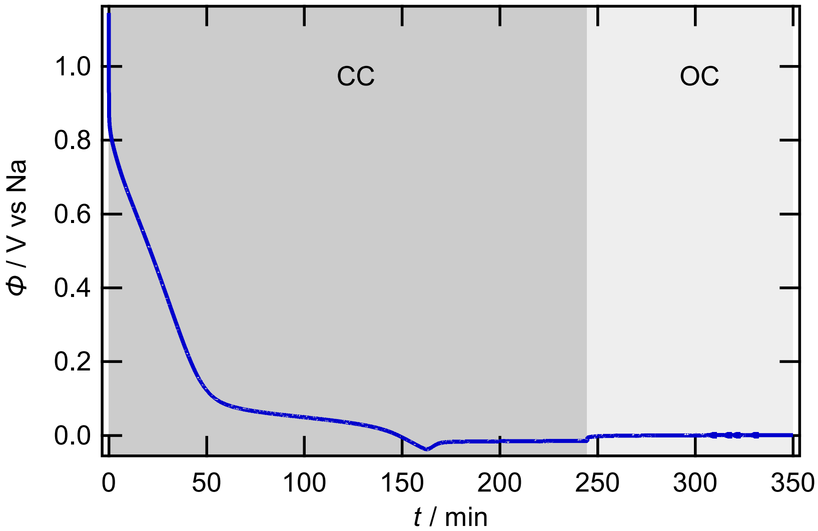

Figure 3.4: Potential during overcharging and Na metal plating on a thin HC electrode (20 µm) in 1 M $NaClO_4$/PC with a constant current (CC) of −40 µA to prepare the electrode for the calibration. The beginning of Na metal plating is indicated by the minimum at $t \approx 160$ min.

When the investigations with the HC composite electrode were completed, the electrode was galvanostatically overcharged, so that Na metal plating occurred on the electrode. The potential during the overcharging is shown in Figure 3.4. The typical charging curve of HC is followed by a minimum of the potential of ca. −40 mV, which indicates the beginning of Na plating. After reaching the minimum, the current was applied continuously and the potential stabilized around −15 mV. In a similar experiment, Gotoh *et al.* could clearly identify metallic Na on the HC with solid-state nuclear magnetic resonance (NMR).[35] After switching to open circuit (OC) conditions, the potential relaxed toward 0 V vs. Na/Na$^+$ as expected, when the surface is covered with metallic Na.

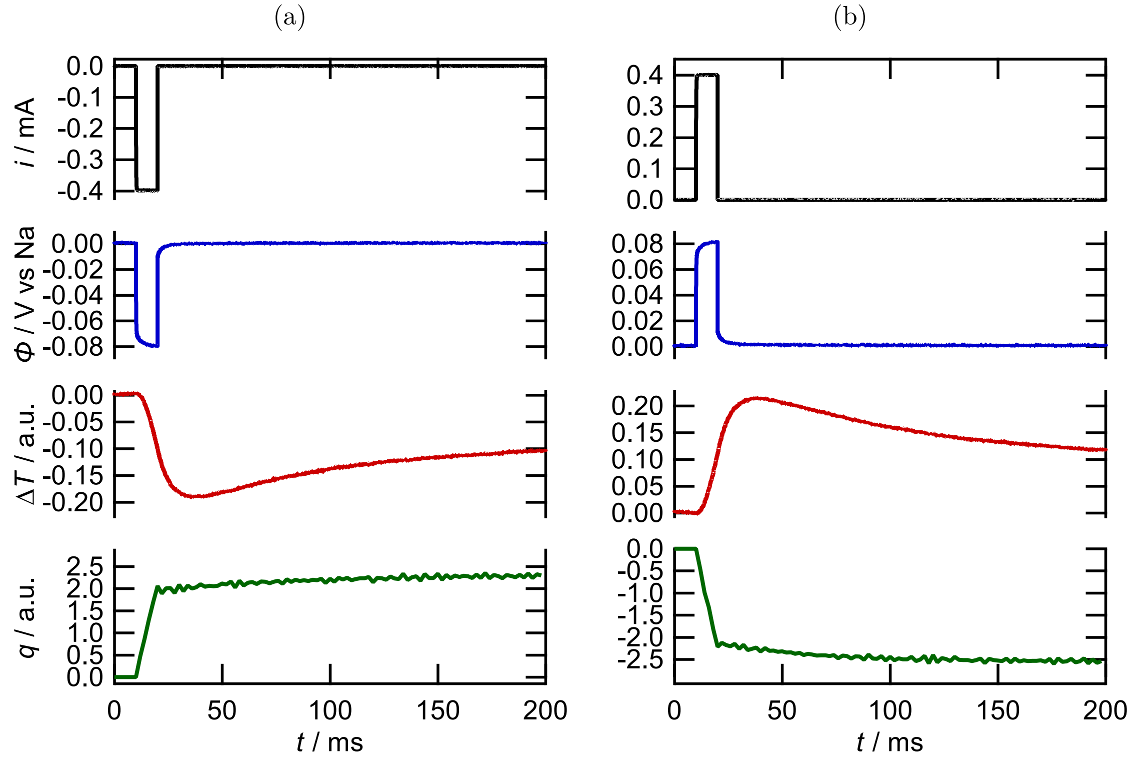

Figure 3.5: Current i, potential ϕ and temperature ΔT transients and the heat q resulting from a 10 ms (a) Na plating and (b) Na stripping pulse on an overcharged, thin HC electrode (20 µm) in 1 M $NaClO_4$/PC.

On the prepared Na metal surface, microcalorimetric pulse measurements were performed in the respective electrolyte solution. The current, potential, temperature and heat transients for Na plating and stripping are shown exemplary in Figure 3.5. The overpotential during the pulse is mostly dominated by the iR-drop in the electrolyte solution and after the pulse the potential relaxes to its initial value within 10 ms. As expected, the temperature decreases during Na plating and increases during Na stripping. The heat exchange is not fully complete at $t = 20$ ms, which was explained by Karcher *et al.* with continuous desolvation of the Na$^+$ ions.[36] Thus, the heat at times above $t > 500$ ms was used to determine the reversibly exchanged heat by interpolation to zero overpotential and subsequently to calculate a calibration factor.

Since the HC composite electrodes were porous and were wetted with the electrolyte solution during the experiment, the calibration measurement had to be conducted with the same electrolyte solution. For the Na metal deposition from 1 M $NaPF_6$/EC,PC + fluoroethylene carbonate (FEC) electrolyte solution no data on the Peltier heat existed. To be able to calibrate the respective HC experiments, the Peltier heat of this reaction was measured herein, akin to the experiments of Karcher *et al.*[29] The microcalorimetric pulse measurements were performed on a thick Na metal film (around 6000 monolayers), which was electrochemically deposited on a dendritic Cu foil. These experiments could be calibrated with the aqueous Fe^{2+}/Fe^{3+} solution. Before doing so, the Na film was removed by rinsing the cell with water. Then, the bare Cu foil was plated electrochemically with a thin layer of Au. Au was electrochemically plated for 10 min with a current of −2 mA from a Au-containing electrolyte solution (Autronex C, Dürrwächter). From three experiments the Peltier heat of the Na metal deposition from 1 M $NaPF_6$/EC,PC + FEC electrolyte solution was determined to be $\Pi = (36.7 \pm 1.2)\,\mathrm{kJ\,mol^{-1}}$, corresponding to a reaction entropy of $\Delta_\mathrm{R}S = (113 \pm 4)\,\mathrm{J\,mol^{-1}\,K^{-1}}$ considering $\Delta_\mathrm{T}S = -10\,\mathrm{J\,mol^{-1}\,K^{-1}}$ (see Table 4.1).

Difficulties with the Thick HC Electrodes

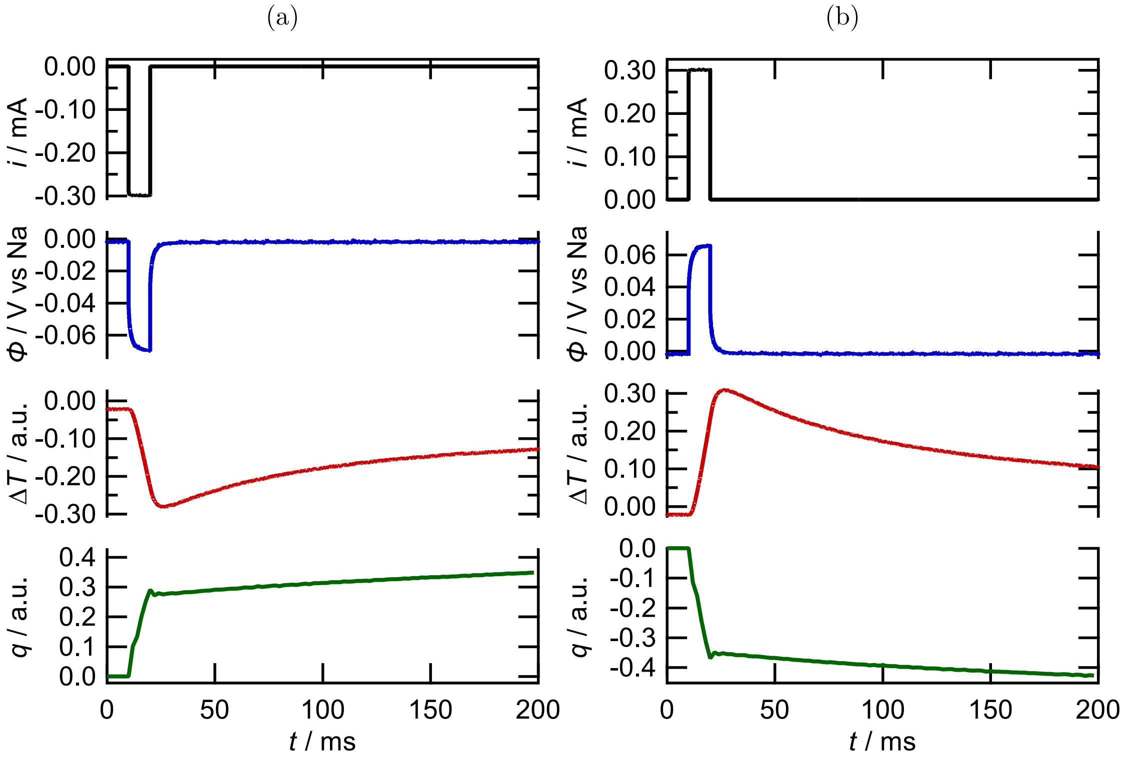

Figure 3.6: Current i, potential ϕ and temperature ΔT transients and the heat q resulting from a 10 ms (a) Na plating and (b) Na stripping pulse on an overcharged, thick HC electrode (46 µm) in 1 M $NaPF_6$/EC,PC + FEC.

For the calibration of the microcalorimetric experiments with the thick HC electrodes (46 µm), the same procedure as for the thin HC electrodes (20 µm) was employed. The thick HC electrode was overcharged, so that Na metal was plated on the electrode. Subsequently, microcalorimetric pulse measurements of the Na metal plating/stripping reaction were performed. In Figure 3.6 the current, potential, temperature and heat transients of an exemplary (a) Na plating and (b) Na stripping pulse are shown. As expected, the overpotential during the pulse was rather constant and after the current pulse the potential relaxed toward the initial potential within 5 ms. A steep in-/decrease of the heat was observed during the current pulse. After the current pulse ($t > 20$ ms) heat was still exchanged and the heat did not reach a steady value within $t = 1000$ ms. A possible reason might be, that the porous HC electrode was not uniformly plated with Na metal and consequently the Na plating/stripping pulses led to heat inputs, which were inhomogeneously distributed across the HC composite electrode. Such heat inputs could possibly lead to a delayed thermal equilibration of the electrode. As a result, a reliable calibration factor for the microcalorimetric experiments with the thick HC electrodes could not be determined. Still, an estimation of the order of magnitude could be given (see chapter 4.2.3).

Calibration of the Microcalorimetric Experiments with NVP/C

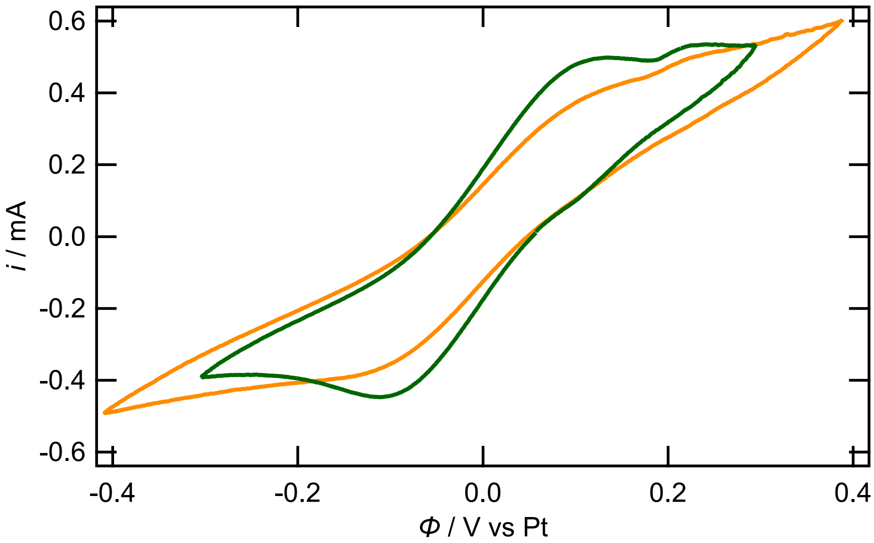

Figure 3.7: Cyclic voltammograms with a scan rate of 88 mV s^{1-} of a NVP/C electrode in 0.1 M $K_3[Fe(CN)_6]/K_4[Fe(CN)_6]$ aqueous electrolyte solution after the microcalorimetric experiments with 1 M $NaPF_6$/EC,PC + FEC (green) and 1 M $NaPF_6$/diglyme (orange).

The microcalorimetric experiments with the NVP/C electrodes were calibrated using the electron transfer reaction in the $[Fe(CN)_6]^{4-}/[Fe(CN)_6]^{3-}$ redox system. After the microcalorimetric experiment, the organic electrolyte solution was removed and the cell was rinsed five times with water. Thereafter, 0.1 M $K_3[Fe(CN)_6]/K_4[Fe(CN)_6]$ aqueous electrolyte solution was filled in the cell. For the CE and RE a Pt wire was used. Before the microcalorimetric pulse measurements, a cyclic voltammogram (CV) was recorded. In Figure 3.7 the CVs of NVP/C in 0.1 M $K_3[Fe(CN)_6]/K_4[Fe(CN)_6]$ aqueous electrolyte solution after the microcalorimetric experiments with 1 M $NaPF_6$/EC,PC + FEC (green) and 1 M $NaPF_6$/diglyme (orange) are compared. The CV after the experiments with $NaPF_6$/EC,PC + FEC (green line) has a clearly identifiable positive and negative peak at around 0.1 V and −0.1 V, respectively. At potentials exceeding 0.2 V an additional positive peak was found, which is not expected for the Fe^{2+}/Fe^{3+} redox system. In the CV after the experiments with $NaPF_6$/diglyme (orange line) such distinct peaks could not be observed, but the current is in the same order of magnitude. At a potential of around 0.2 V a small shoulder can be seen, which might correspond to the additional peak observed in the CV after the experiments with the ester-based electrolyte solution. The differences between the two CVs as well as the additional peak might be caused by remaining organic electrolyte solution in the porous NVP/C composite electrode.

In Figure 3.8 the current, potential, temperature and heat transients of exemplary current pulses of NVP/C in 0.1 M $K_3[Fe(CN)_6]/K_4[Fe(CN)_6]$ aqueous electrolyte solution after the microcalorimetric experiments with 1 M $NaPF_6$/EC,PC + FEC ((a) and (b)), and 1 M $NaPF_6$/diglyme ((c) and (d)) are shown. No significant differences were found in the potential transients. In contrast, the shape of the temperature transients is different, dependent on which organic electrolyte solution was used in the experiment. However, the differences in the temperature transients are not reflected in the heat transients. This can be readily explained, because the thermal response functions used for the deconvolution of the temperature transients were generated from Fe^{2+}/Fe^{3+} temperature transients of the respective experiment (see chapter 5.4).

The microcalorimetric pulse measurements for the calibration do not show noticeable problems. Nevertheless, different calibration factors were obtained in the microcalorimetric experiments with NVP/C in 1 M $NaPF_6$/diglyme. Consequently, the reaction entropy found for NVP/C in 1 M $NaPF_6$/diglyme three experiments differed by up to $100\,\mathrm{J\,mol^{-1}\,K^{-1}}$, i.e., around 50 % (cf. Figure 5.8). This was not the case for the microcalorimetric experiments of NVP/C in 1 M $NaPF_6$/EC,PC + FEC, where the deviation between two experiments was below 10 %. It could not be clarified conclusively, why the reproducibility of the calibration of the microcalorimetric experiments of NVP/C in $NaPF_6$/diglyme was so low. Presumably, remaining organic electrolyte solution as well as other impurities, which might have been dissolved with water from the NVP/C composite electrode, caused these difficulties of the calibration.

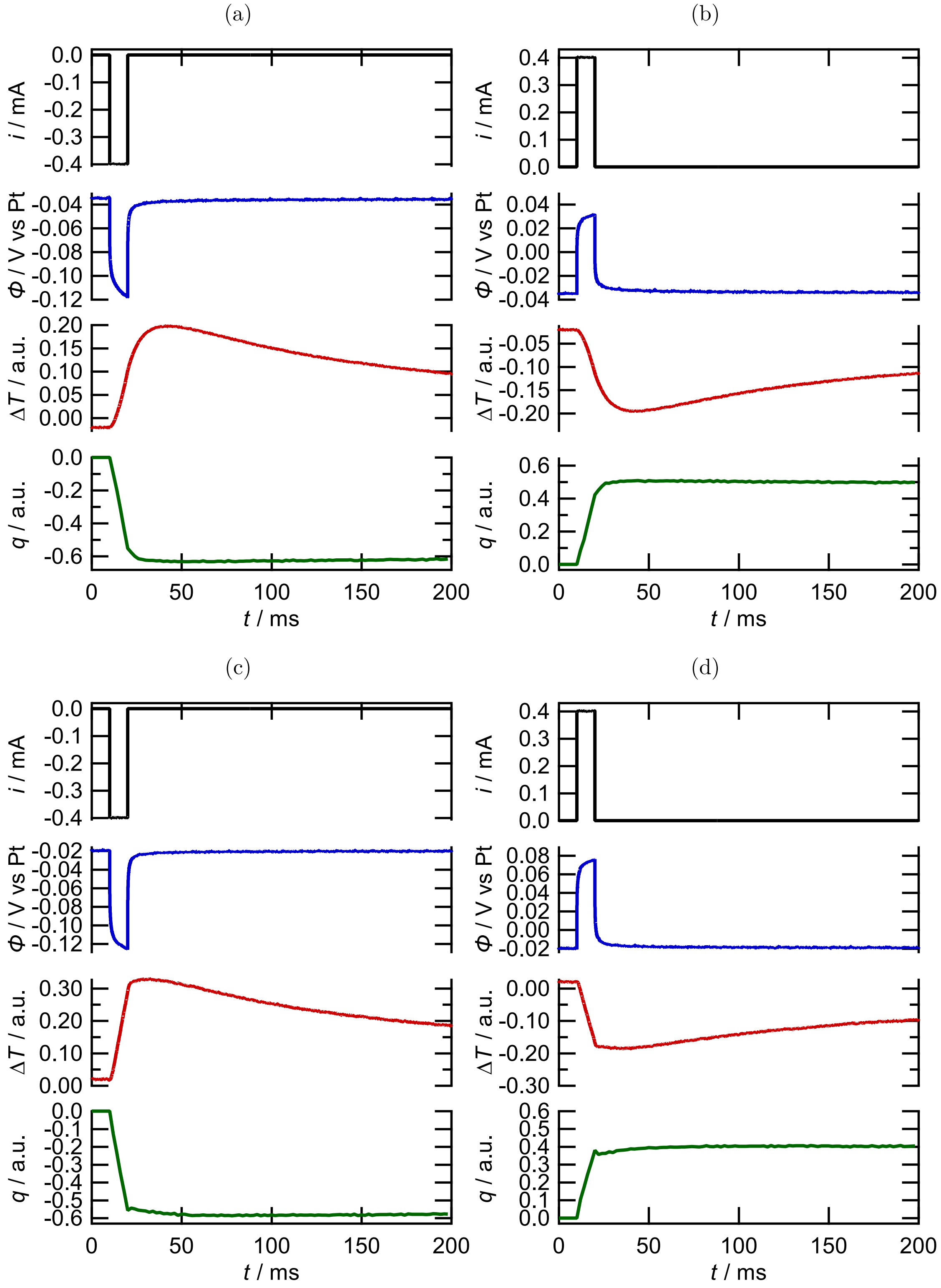

Figure 3.8: Current i, potential ϕ and temperature ΔT transients and the heat q resulting from 10 ms current pulses of a NVP/C composite electrode in 0.1 M $K_3[Fe(CN)_6]/K_4[Fe(CN)_6]$ aqueous electrolyte solution after the microcalorimetric experiments with (a),(b) 1 M $NaPF_6$/EC,PC + FEC and (c), (d) 1 M $NaPF_6$/diglyme.

3.1.4 Reproducibility and Error Estimation

Different errors can alter the microcalorimetric results. External influences, such as the temperature and the pressure can change from experiment to experiment but as well within a single experiment. Vibrations, e.g., induced by the circulation within the glovebox, lead to an increased noise of the sensor signal. Thus, typically 60 pulses are recorded at each measuring point, i.e., at each SoC of the composite electrodes. To evaluate the reproducibility, the experiments were repeated. In this work a microcalorimetric experiment refers to all measurements performed with one microcalorimeter assembly, i.e., all measurements, which were calibrated with the same calibration factor. The calibration of the microcalorimeter leads to an additional error of the absolute heat values, since measured values, which themselves have an uncertainty, are used to calculate the calibration factors.

The microcalorimetric experiments with the HC electrodes were repeated three times for the 1 M $NaClO_4$/PC, 1 M $NaClO_4$/PC+FEC and the 1 M $NaPF_6$/diglyme electrolyte solution and measured once for the 1 M $NaPF_6$/EC,PC + FEC electrolyte solution. As described in the previous chapter, the HC experiments had to be calibrated with Peltier heats for the Na metal deposition from the respective electrolyte solution, which introduced another error since, e.g., the values determined by Karcher *et al.* for 1 M $NaClO_4$/PC and 1 M $NaPF_6$/diglyme have a standard deviation of around $\pm 3\,\mathrm{kJ\,mol^{-1}}$. Overall the error of the HC experiments sums up to about ±10 %.

The microcalorimetric experiments with the NVP/C electrodes, as well as the Na metal deposition from 1 M $NaPF_6$/EC,PC + FEC electrolyte solution, were calibrated with the aqueous Fe^{2+}/Fe^{3+} electrolyte solution. For this system Boudeville measured a value of $-45.1\,\mathrm{kJ\,mol^{-1}}$,[32] which is used herein. But, it should be noted that different values are reported for this system. Wang *et al.*, e.g., found a Peltier heat of $-41.5\,\mathrm{kJ\,mol^{-1}}$.[37]. The reproducibility of the Na metal deposition from the 1 M $NaPF_6$/EC,PC + FEC electrolyte solution was checked by repeating the measurement three times and a standard deviation below 4 % was found. The measurements with the NVP/C electrode in 1 M $NaPF_6$/EC,PC + FEC electrolyte solution were repeated two times with a maximum deviation below 10 % between both measurements. The measurements with the NVP/C electrode in 1 M $NaPF_6$/diglyme electrolyte solution were repeated three times and the deviation was up to 50 % due to difficulties in the calibration measurements (see chapter 3.1.3).

3.2 Entropy Profiling with Stepwise Temperature Changes

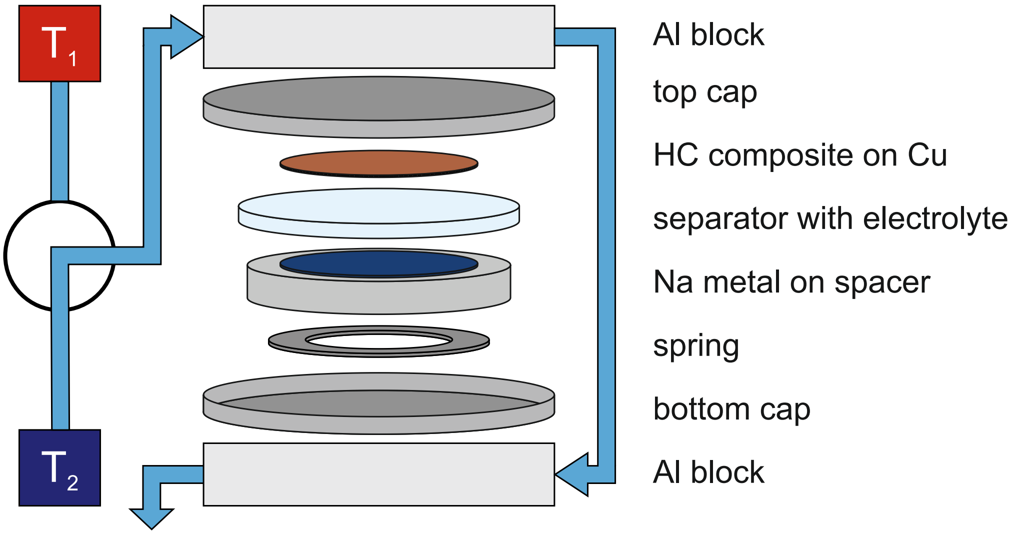

Figure 3.9: Experimental setup used for the temperature step experiments. The stainless-steel coin cell (shown exemplarily for the HC|Na metal cell) was clamped between two Al blocks, which were flushed with water either from a warm or cool reservoir.

In chapter 2.1 it was shown that from the temperature dependence of the equilibrium cell voltage the cell reaction entropy of an electrochemical cell can be obtained (c.f equation 2.2). Dahn *et al.* applied this approach already in the early 80s to investigate Li|$LiTiS_2$ cells,[23] and more recently this so-called entropy profiling was used by several groups to determine $\Delta_R S_{cell}$ of HC|Na metal cells. All these studies have in common that the temperature of the cells was changed by heating or cooling the cell with a single thermostat or measurement chamber. Thus, changing the temperature of the cell was limited by the heating or cooling rate of the thermostat or the measurement chamber and temperature changes by, e.g., 5 K took at least 10 min. Consequently, it might be difficult to separate the variations of the equilibrium cell voltage, due to the temperature change, from drift of the cell voltage, caused by, e.g., slow diffusion processes. To overcome these difficulties, an experimental setup is presented herein, which allows to change the temperature of coin cells within less than 60 s by switching between two thermostats at different temperatures. In the following the experimental setup and the coin cells employed for the temperature step experiments are described. The measurement procedure and the results are presented later in chapter 4.3.

For the temperature step experiments stainless-steel CR2032 2-electrode coin cells, either with HC and Na metal or HC and NVP/C, were used. The HC|Na metal cells were assembled by Krishnaveni Palanisamy (IABC, Ulm University) in an Ar-containing glovebox (MBraun, O_2 and H_2O $<$ 0.1 ppm). The HC composite electrode (diameter 12 mm) was combined with Na metal (Alfa Aesar, Germany) pressed on a stainless-steel spacer as CE (diameter 12 mm). The glass fiber separator (diameter 15 mm, Whatman GF/F, United Kingdom) was soaked with 130 µl 1 M $NaPF_6$/diglyme electrolyte solution. A stainless-steel spring was used to press the electrodes together to ensure low electric contact resistances.

The NVP/C|HC cells were assembled by Salimeh Saleh (IABC, Ulm University) analogously to the HC|Na metal cells. The HC composite electrode (diameter 12 mm) was combined with a NVP/C composite electrode (diameter 12 mm). QMA glass fiber was used as separator and 1 M $NaPF_6$/EC,PC as electrolyte solution.

The experimental setup used for the temperature step experiments is shown schematically in Figure 3.9 exemplary with the HC|Na metal cell. The coin cell was clamped between two Al blocks, which were flushed with water from a thermostat. Two thermostats (Haake F3/K and Lauda M3) were used and set to different temperatures (25.0 °C and 20.7 °C or 29.5 °C and 20.3 °C). By switching the water flow between the two thermostats with magnetic valves, the temperature of the Al block was changed within less than 10 s. The temperature of the Al block was measured with a thermocouple, which was mounted at the outside of the lower Al block. The cell potential and the temperature was measured with a data logger (Agilent 34970A) and a custom-built galvanostat was used to apply current to charge or discharge the cell. Experimental control and data acquisition were realized with Igor Pro® from Wavemetrics®. A block diagram of the temperature step experiment is shown in the appendix in Figure C.2.

3.3 Electrodes and Electrolyte Solutions

3.3.1 Electrodes

Three different composite electrodes were used in this work.

(1) A spray-coated HC composite electrode with a final composite thickness of 20 µm, hereafter referred to as **thin HC electrode**.

(2) A HC composite electrode with a final composite thickness of 46 µm, hereafter referred to as **thick HC electrode**.

(3) A NVP/C composite electrode with a final composite thickness of 99 µm, hereafter referred to as **NVP/C electrode**.

The thick HC and the NVP/C electrode were the two composite electrodes of the SIB reference system of the Post Lithium Storage (POLiS) Cluster of Excellence. In the following the preparation of all composite electrodes is described. Thereafter, specific preparations of the composite electrodes for the application in the different experimental approaches are outlined.

(1) The thin HC composite electrodes were prepared by Krishnaveni Palanisamy (IABC, Ulm University) as described in detail in reference.[38] In short, a water-based slurry consisting of 85 % HC (Kuranode, 5 µm (type II), Kurary, Japan) active material, 5 % Na carboxymethyl cellulose (CMC, molecular weight 124000, Sigma-Aldrich, Germany) as binder and 10 % carbon black (Vulcan XC72R, Cabot Corporation, USA) as conductive carbon was spray-coated onto a 50 µm thick Cu foil (99.995 %, Advent). The coating thickness was around 20 µm and the mass loading was about 1.8 mg cm^{-2}. The electrodes were dried overnight at RT and subsequently dried under vacuum at 80 °C for 12 h.

(2) The thick HC composite electrodes were prepared by Julian Klemens (TFT, KIT) as described in reference.[39] The composite electrodes consisted of 93 wt% HC (Kuraray Kuranode Type II (9 µm)), 1.4 wt% carbon black (TIMCAL C-NERGY Super C65 (Imersy)), 1.87 wt% carboxymethyl cellulose (MAC500LC (Nippon Paper)) and 3.73 wt% styrene-butadiene rubber (BM-4xx (Zeon)). For the current collectors Al foil (20 µm) was used. The active mass loading was 3.67 mg cm^{-2} and the final thickness of the coating was 46 µm.

(3) The NVP/C composite electrodes were prepared as described in reference.[39] The NVP/C was synthesized in the group of Joachim Binder (IAM-ESS, KIT) and the composite electrodes were processed by Marcus Müller (IAM-ESS, KIT). The NVP/C active material was synthesized with a two-step spray-drying process starting from Na_2CO_3, $NH_4H_2PO_4$, NH_4VO_3 and β-lactose. The slurry for the NVP/C composite electrodes consisted of 90.5 wt% NVP/C, 3.0 wt% carbon black (C65, C-Nergy), 2.0 wt% graphite (KS6L, Timical-Imerys) and 4.5 wt% PVDF (Solef 5130, Solvay). The slurry was coated onto 16 µm thick Al foil. The final thickness of the coating after drying and calendering was 99 µm.

Microcalorimetric Experiments

For the use of thin HC electrodes in electrochemical microcalorimetry, electrodes with a diameter of 9 mm were punched out. The composite coating covered only an inner circle with a diameter of 5 mm of the electrodes. The bare current collector at the edge was used for the electrical contact in the electrochemical microcalorimeter. The final electrodes were additionally dried for 2 h under vacuum at 80 °C, before they were assembled in the electrochemical microcalorimeter cell.

The thick HC and the NVP/C electrodes were fully coated. For the microcalorimetric experiments, electrodes with 9 mm diameter were punched out and the coating was removed on the outside by fixing the electrode on a spinning disk and using a glass fiber pencil to scrape off the coating. A spot with 5 mm diameter was left and the electrode could be electrically contacted from the top side as described in chapter 3.1.1.

For the measurements of Na metal bulk deposition, a dendritic Cu foil (diameter 9 mm, Carl Schlenk, Roth) was flattened at the edge with a hammer, so that the 5 mm O-ring could reliably tighten the electrochemical microcalorimeter cell. Before the electrode was assembled, it was cleaned with ethanol and dried under N_2 flow.

Temperature Step Experiments

For the HC|Na metal cells the thin HC composite electrodes were used. They were prepared by spray-coating as the ones used for the microcalorimetric experiments. However, fully coated electrodes with a diameter of 12 mm and a mass loading between 1.2 mg cm^{-2} to 1.3 mg cm^{-2} were used.

For the NVP/C|HC cells, the NVP/C composite electrodes and the thick HC electrodes were used.

XPS Study

For the XPS study the thick HC electrodes were used.

3.3.2 Electrolyte Solutions

Microcalorimetric Experiments

The 1 M $NaClO_4$/PC electrolyte solution was prepared by Krishnaveni Palanisamy (IABC, Ulm University) as described in reference [38] by mixing 1 M $NaClO_4$ (Alfa Aesar, Germany) with anhydrous PC (Sigma-Aldrich, Germany) and adding 2 wt% FEC (Sigma-Aldrich, Germany) if required.

The 1 M $NaPF_6$/diglyme electrolyte solution was prepared in the group of Reiner Mönig (IAM-MMI, KIT) by mixing 1 M $NaPF_6$ (99+ %, Alfa Aesar), which was dried under vacuum at 100 °C for at least 24 h, with diglyme (99.5 %, Sigma-Aldrich).

The 1 M $NaPF_6$/EC, PC + FEC electrolyte solution was prepared in the group of Anna Smith (IAM-ESS, KIT) as described in reference [40] by mixing 1 M $NaPF_6$ (Chemfish, 99.9 %) with EC (Gotion, >99.5 %) and PC (Gotion, >99.5 %) in a 1:1 wt. ration and adding 5 wt% FEC (Gotion, >99.5 %).

The electrolyte solution for the calibration of the electrochemical microcalorimeter was prepared by mixing 0.1 M $K_3[Fe(CN)_6]$ (>99 %, Thermo Scientific) and 0.1 M $K_4[Fe(CN)_6]$ (>99 %, Thermo Scientific) in ultrapure water (18.2 MΩcm, Sartorius Arium).

Temperature Step Experiments

The electrolyte solution for the HC|Na metal cells was prepared by Krishnaveni Palanisamy (IABC, Ulm University) by mixing 1 M $NaPF_6$ (Sigma Aldrich, Germany) in anhydrous diglyme (Sigma Aldrich, Germany).

The 1 M $NaPF_6$/EC,PC electrolyte solution for the NVP/C|HC cells was prepared as the one for the microcalorimetric experiments without adding FEC.

XPS Study

The electrolyte solutions were prepared by mixing 1 M $NaPF_6$ (Fluorochem, 99.9 %) with diglyme (Sigma-Aldrich, ≥99 %) or with PC (Gotion, 99.99 %) and EC (Gotion, 99.98 %) in a 1:1 wt. ratio and adding 5 wt% FEC (Solvionic, battery grade).

3.4 X-ray Photoelectron Spectroscopy

The pouch cells for the XPS study were assembled in an Ar-containing glovebox (O_2 and $H_2O < 1$ ppm). Na metal (Sigma-Aldrich, ACS reagent) on Al foil was used as counter electrode (12 mm diameter). The HC working electrodes (10 mm diameter) were dried under vacuum at 120 °C for 20 h. For the $NaPF_6$/diglyme cells Celgard 2400 (25 µm) and for the $NaPF_6$/EC, PC cells Solupor (E-8P01E, DSM) were used as separators (16 mm diameter), which were dried under vacuum at 70 °C for 6 h. The galvanostatic cycling was performed at a Neware cycler.

After the different cycling protocols (see chapter 4.5), the pouch cells were disassembled in an Ar-containing glovebox (O_2 and $H_2O < 1$ ppm). To prepare the samples, the HC electrodes were dipped into 300 µl dimethyl carbonate (DMC) for 10 s, dried for 30 mins in the Ar-atmosphere and then dried for 1 h under vacuum. DMC was used for the cleaning procedure as it shouldn't change the amount of carbonaceous species present in the SEI.[41] The sample transfer was performed without exposing the samples to air. The samples were grounded and no charge neutralization was used. The XP spectra were recorded with a Kratos AXIS Supra$^+$ equipped with an Al (1486.7 eV) and an Ag (2984.3 eV) source.

The XPS study, including the cell assembly and cycling, was conducted in the group of Maria Hahlin at the Ångström Advanced Battery Centre at Uppsala University.

4

Sodiation of Hard Carbon

In commercially available SIBs, HC is commonly used as active material in the negative composite electrode. Nonetheless, a comprehensive understanding of the underlying sodiation mechanism of HC is still missing. Thermodynamic information on different timescales might help to identify and understand the processes taking place during the sodiation of HC. In the following chapter different aspects of the sodiation of HC will be examined. First, an overview of the current state of research is given in chapter 4.1. Thereafter the determination of the reaction entropy of the sodiation of HC with electrochemical microcalorimetry is explained in chapter 4.2. The determination of the cell reaction entropy of HC|Na metal cells by measuring the temperature dependence of the equilibrium cell voltage is presented in chapter 4.3. In chapter 4.4 the reaction entropy of the sodiation of HC on different timescales is compared. The contributions to the reaction entropy, the variation of the reaction entropy with the SoC and kinetic limitations of the sodiation of HC are discussed. The last chapter 4.5 is an excursus to XPS measurements of HC electrodes to assess the stability of the SEI formed on the HC electrodes. It should be noted that parts of the microcalorimetric results were published by Derr *et al.* as a paper titled "Role of Desolvation upon the Sodiation of Hard Carbon in Sodium-Ion Batteries: A Microcalorimetric Study of the Sodiation Entropy" in the Journal of Physical Chemistry C.[42] The entropy profiling results were accepted by Batteries & Supercaps as a paper by Derr *et al.* titled "Entropy Profiling of Hard Carbon/Na Metal Cells with Stepwise Temperature Changes: Influence of the Sodiation Kinetics on the Cell Voltage Response".[43] Herein, the results are explained in more detail and the combination of the results of both methods opens up new perspectives in the interpretation of the ongoing processes during the sodiation of HC.

4.1 Current State of Research

Hard carbon denotes carbonaceous material, which cannot be graphitized even at temperatures above 3000 °C - thus, it is also called non-graphitizable carbon.[44] It consists of pseudo-graphitic domains with high interlayer spacing (around 0.37 nm), surface defects, hetero atoms, and open and closed micropores.[4] It is generally synthesized by pyrolyzing a precursor in the absence of oxygen. The range of precursors is broad and can be classified into biomass, biopolymers and synthetic polymers.[5] Out of curiosity some reported biomass precursors for HC (from the review article by Ghimbeu *et al.*[5]) are listed here: apple waste, asparagus peel, ginkgo leaves, macadamia nut shell, papaya seed, ddA. The broad range of precursors naturally results in a broad range of HC materials with different constitutions of their microstructure. Various experimental techniques are used to characterize the microstructure of HCs.[4, 5, 44] XRD patterns of HC show broad peaks, since they don't have a crystalline structure. Still, the (002) peak resulting from the graphene sheets can be used to estimate the interlayer spacing. At low scattering angles the background signal increases, which is due to diffuse scattering of the X-rays originating from the fine structure microporosity of HC. With small-angle X-ray scattering (SAXS) experiments, average particle and pore sizes of HCs can be obtained. The surface area and porosity can be probed with gas adsorption/desorption. Such measurements are highly dependent on the size of the gas molecules. In HC, there exist closed pores, which might not be accessible by gases, but can still be reached by Na^+ ions through solid diffusion and thus contribute to the capacity of HCs. Lastly, Raman spectroscopy is used to characterize defects in HC by determining the intensity ratio of the D and G peak, corresponding to the defect-induced mode and the graphitic mode, respectively.

The use of HC as material for the negative electrode in SIBs was presented for the first time by Stevens and Dahn and in 2000, who achieved reversible insertion of Na into HC with a capacity of up to $300\,\mathrm{mAh\,g^{-1}}$.[45] The potential profile during charging of HC, i.e., sodiation of HC, can be generally divided into two regions. In the sloping region the potential is steadily decreasing from 2 V (vs. Na/Na^+) to about 0.1 V. In the subsequent plateau region below 0.1 V, the potential only slowly decreases with increasing SoC (see, e.g., Figure 4.3). While such a potential profile is generally found for different HCs, the ratio between the capacities of the sloping and the plateau regions can differ.

Sodiation Mechanism of Hard Carbon

Extensive research was and is dedicated to the understanding of the sodiation mechanism of HC. In general, three main processes and sites, which are illustrated in Figure 4.1, are discussed: adsorption at defects and heteroatoms, intercalation into

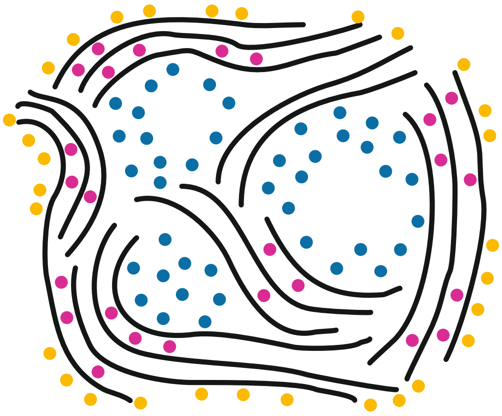

Figure 4.1: Schematic illustration of the microstructure of HC and the main processes and sites for Na storage: adsorption at defects (orange), intercalation into pseudo-graphitic domains (pink) and filling of the pores (blue) (adapted from Ref.[46]).

the layers of the pseudo-graphitic domains and filling of the micro- and nanopores.[4] The assignment of the different processes to certain potential ranges is still a matter of discussion, which is enhanced by the diverse microstructure of HCs and the various applied characterization techniques.[5] In the following an overview of the four most prominent models for the sodiation mechanism of HC is provided, without claiming to be complete.

- The **intercalation-pore filling model** was initially presented by Stevens and Dahn, who followed the structural changes of HC during charging with wide-angle X-ray scattering (WAXS) and SAXS.[47] They attributed the increase of the interlayer spacing in the sloping region to intercalation between graphene sheets and a decreasing scattering intensity in the plateau region to filling of the nanopores. This model was corroborated with dilatometric thickness measurements by Escher *et al.*[48]. Additionally, they found that Na plating takes place at the end of the plateau region.

- In the **adsorption-intercalation-pore filling** model Na storage at defect sites (such as vacancies or hetero atoms) in the sloping region is followed by intercalation of Na in the beginning of the plateau region. Ultimately pore filling takes place. This was proposed, among others, by Bommier *et al.*, who found that the capacity in the sloping region increases with increasing concentration of defects.[49] The concentration of defects was controlled by the synthesis temperature and determined with Raman spectroscopy. This model was supported by, e.g., Reddy *et al.* on the basis of *in situ* Raman scattering measurements and ab initio density functional theory (DFT) calculations, but they ascribed parts of the capacity in the sloping region to intercalation and the whole capacity in the plateau region to pore filling.[50]

- The **adsorption-intercalation** model includes adsorption of Na^+ ions at defects and heteroatoms in the sloping region and intercalation into the graphitic layers in the plateau region. It was presented by Qiu *et al.*, who considered pore filling of Na in HC unlikely, since they found metallic and quasimetallic Na only when the potential was below 0 V.[51]
- In the **adsorption-pore filling** model, intercalation is excluded and the capacity in the plateau region is ascribed to Na pore filling. This was, e.g., suggested by Bai *et al.*, who found no evidence for Na^+ ion intercalation into the graphitic layers with XRD and Raman spectroscopy.[52] With pair distribution function (PDF) analysis and solid-state NMR, Stratford *et al.* investigated the local atomic environment of Na stored in HC.[53] They observed that in the plateau region metallic Na clusters are formed and that the capacity of the plateau region rather depends on the number of pores with a suitable size and not the total pore volume.

Complimentary to the investigations of structural changes, electrochemical impedance spectroscopy (EIS) was intensively employed to study the electrochemical processes during the sodiation of HC on different time scales.[54–60] Linsenmann *et al.* used a partially sodiated tin wire as RE in order to differentiate the contributions of the HC WE and the Na metal CE to the impedance and found that the charge transfer resistance at the HC electrode is rapidly decreasing with increasing SoC during the sloping region and remains rather constant in the plateau region.[54] Similar results were reported by Aniskevich *et al.*[55] Correspondingly, they derived from temperature-dependent EIS measurements that the activation energy of the charge-transfer process is decreasing with increasing SoC. Schutjajew *et al.* analyzed the distribution of relaxation times of impedance spectra and found electrochemical processes with time constants ranging from ms up to several seconds.[56] Especially at low SoCs the impedance was dominated by slow processes, which they ascribed to Na^+ ion transport by diffusion. Furthermore, thermodynamic studies were conducted, as they can provide more information about the underlying mechanisms of the charging processes. In particular, the reaction entropy of HC|Na metal cells was measured by different groups with entropy profiling.[61–64] Mercer *et al.* explained the found variation of the entropy with increasing SoC with a solid solution model in which Na fills first the interlayers and subsequently the nanopores.[61] In a follow-up study with HCs synthesized at different temperatures, the pore filling and its energetics were investigated further.[62]

Electrolyte Solutions and the SEI

The electrolyte solution directly influences the electrochemical processes taking place at and in the HC composite electrode. Typically, linear or cyclic esters and ethers are used as solvents in SIBs. They are combined with Na salts with rather large anions, such as $NaPF_6$, $NaClO_4$ and NaTFSI. The herein used solvents and salts are

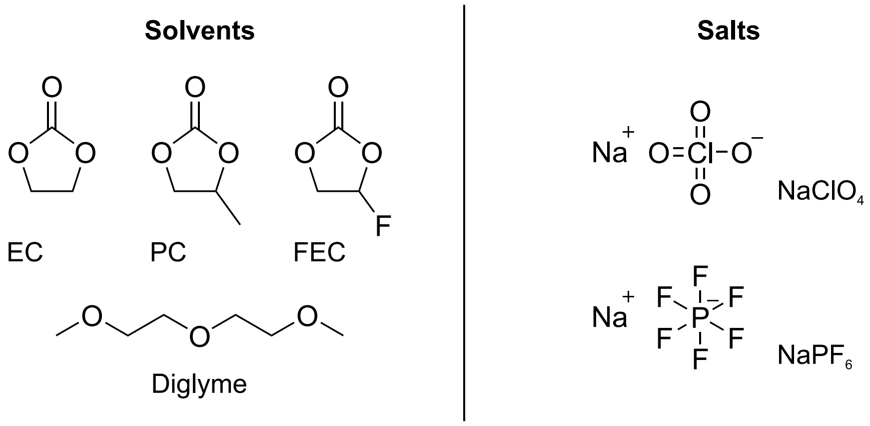

Figure 4.2: Solvents and salts used for the herein investigated electrolyte solutions.

shown in Figure 4.2. The resulting electrolyte solutions should have a low viscosity, a high ionic conductivity (in the order of $\mathrm{mS\,cm^{-1}}$) and a wide electrochemical stability window.[65] During the first sodiation of HC, decomposition of the electrolyte solution occurs, which leads to the formation of a so-called solid electrolyte interphase (SEI), a well known concept in LIBs. The ideal SEI is an electronic insulator to prevent further decomposition of the electrolyte solution, but a good Na^+ ion conductor to allow for fast charging and discharging.[5] Additionally, it should be mechanically and chemically stable, so that it doesn't have to be reformed during operation, which would lead to capacity loss. The composition of the SEI on HC is highly dependent on the electrolyte solution, but is in general composed of organic (e.g. Na ethlyene dicarbonate, Na alkyl carbonates ($ROCO_3Na$), Na alkoxides (RONa)) and inorganic species (e.g. NaF, Na_2CO_3, Na_2O).[41, 66, 67]

Mogensen *et al.* found that in contrast to the SEI in LIBs, the SEI in SIBs suffers from dissolution leading to self-discharge of the HC electrode.[68] By adding FEC to the electrolyte solution they could mitigate this problem. Fondard *et al.* explained this with a higher amount of NaF in the SEI detected with XPS. They found enhanced electrochemical performance of their HC|Na metal cells with FEC.[41] However, in cells without Na metal (e.g. NVP/C|HC) the additive FEC caused detrimental effects,[39] indicating that Na metal, typically used as CE and RE for testing SIB electrode materials, influences the electrochemical performance. This was, e.g., investigated by Bommier *et al.*, who claimed that the degradation of the electrolyte solution at the Na metal electrode is the main reason for capacity fading of HC|Na metal cells.[69] Thus, FEC rather stabilizes the Na metal electrode by passivation than being beneficial for the electrochemical performance of the HC electrode itself.

Research Questions

From the overview of the current state of research on the sodiation of HC, it becomes evident that the working principle of HC in SIBs is still not fully understood. By taking into account the capabilities of the methods presented in chapter 3 (electrochemical microcalorimetry, entropy profiling and XPS), the following questions can be posed and will be addressed among others in the following subchapters.

- What are the main contributions to the reaction entropy of the sodiation of HC?
- How does the reaction entropy of the sodiation of HC vary with the SoC and can this contribute to the understanding of the sodiation mechanism of HC?
- During the sodiation of HC processes on a broad range of timescales take place. Is it possible to differentiate their contributions to the reaction entropy? What can be learned about the kinetics of the sodiation of HC?
- Can the stability of the SEI formed on HC electrodes be assessed with XPS measurements?

4.2 Microcalorimetric Measurements

4.2.1 Measurement Procedure

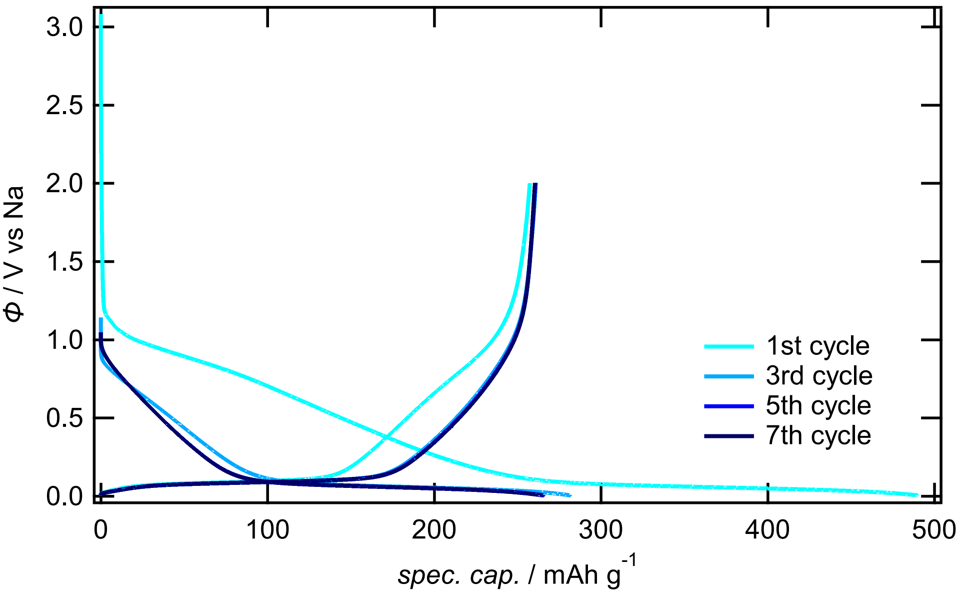

Figure 4.3: Charging and discharging curves of consecutive cycles with a current of ±15 µA (≈C/6) of a thin HC electrode (20 µm) in 1 M $NaClO_4$/PC with a lower potential limit of 0.005 V and an upper potential limit of 2 V.

The microcalorimetric measurement protocol for the thin HC composite electrodes consisted of 8 charging/discharging cycles with a lower potential limit of 0.005 V and an upper potential limit of 2 V vs. Na/Na^+. In Figure 4.3 the charging/sodiation and discharging/desodiation curves of cycle number 1, 3, 5 and 7 with a charging rate of about C/6 are shown. In the first cycle a large irreversible capacity loss of 47 % was detected. This can be ascribed to electrolyte decomposition and the formation of the SEI.[67] In the following cycles the SEI stabilized and from the 5^{th} cycle on symmetric charging/discharging with the typical sloping and plateau region was observed.

In the 2^{nd} and 8^{th} cycle the charging/discharging was interrupted in intervals to perform the microcalorimetric pulse measurements to obtain the reaction entropy of the sodiation of HC at different SoCs. In Figure 4.4 the potential during the 8^{th} is shown exemplarily for such a GITT-type experiment. Twenty minutes CC charging blocks with a charging rate of C/9 were followed by forty minutes relaxation at OC conditions. The microcalorimetric pulse measurements were performed at the end of the relaxation phase so that the WE was close to its equilibrium state. During the three minutes of pulse measurements, the OCV changed by less than 2 mV.

The current, potential, temperature and heat transients of an exemplary sodiation (a) and desodiation (b) pulse of a thin HC electrode at a SoC of 74 % in 1 M $NaClO_4$/PC are shown in Figure 4.5. Current flow in the external circuit was only

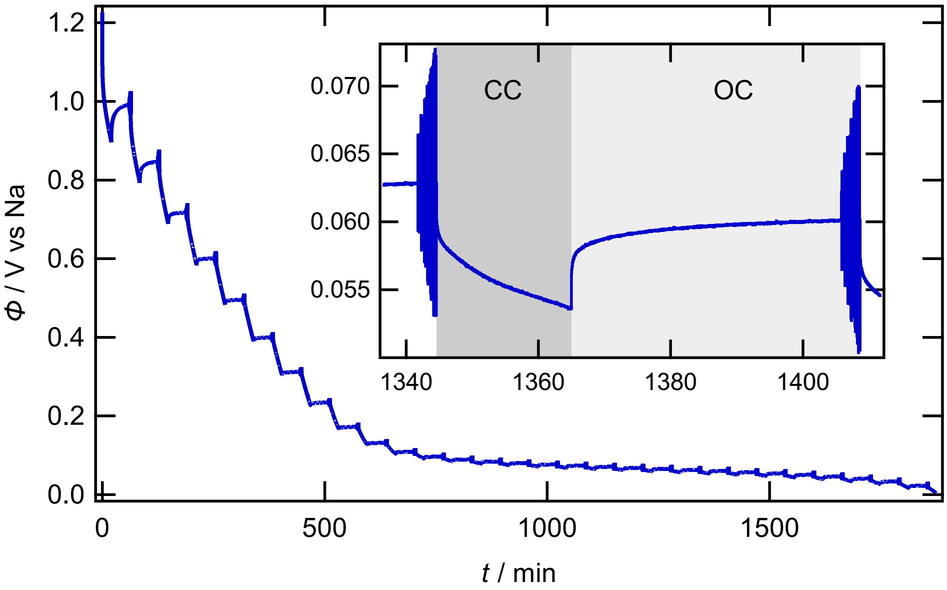

Figure 4.4: Potential during the galvanostatic intermittent titration technique (GITT)-type charging in the 8th cycle of a thin HC electrode (20 µm) in 1 M $NaClO_4$/PC. In the inset a 20 min CC charging block and the consecutive 40 min relaxation phase at OC conditions is depicted. The spikes in the potential are caused by the microcalorimetric pulse measurements.

allowed during the current pulse from $t = 10\,\mathrm{ms}$ to 20 ms and OC conditions were applied before and after the pulse. Since short pulses were used, the SoC of the electrode only changed by about 10^{-5} of the full capacity with a single current pulse. When the current was applied the potential de-/increased stepwise, followed by a shallow de-/increase during the pulse. When the current was switched off, reversed behavior was found and the potential reached its initial potential at around $t = 50\,\mathrm{ms}$. The stepwise potential changes can be attributed to iR-drop in the electrolyte solution due to the current flow. The gradual variation during and after the pulse may be explained with concentration overpotential caused by enrichment or depletion of Na^+ ions in the pores filled with electrolyte solution or Na in the HC grains (a detailed discussion will follow in chapter 4.4.2). The temperature (red line, Figure 4.5) decreased upon sodiation and increased upon desodiation. After the temperature minimum/maximum, which was reached 15 ms to 20 ms after the current was switched off, the temperature relaxed toward the initial temperature, due to heat exchange with the surrounding. Since the temperature response is reversed almost quantitatively by switching between charging and discharging, the sodiation/desodiation of HC with short current pulses is a highly reversible reaction. The slightly larger temperature difference upon desodiation (warming) compared to sodiation (cooling) can be explained with the polarization heat, which leads to heating independent of the pulse polarity.

The thermal response of the cell to 10 ms lasers pulses was added with an adjusted

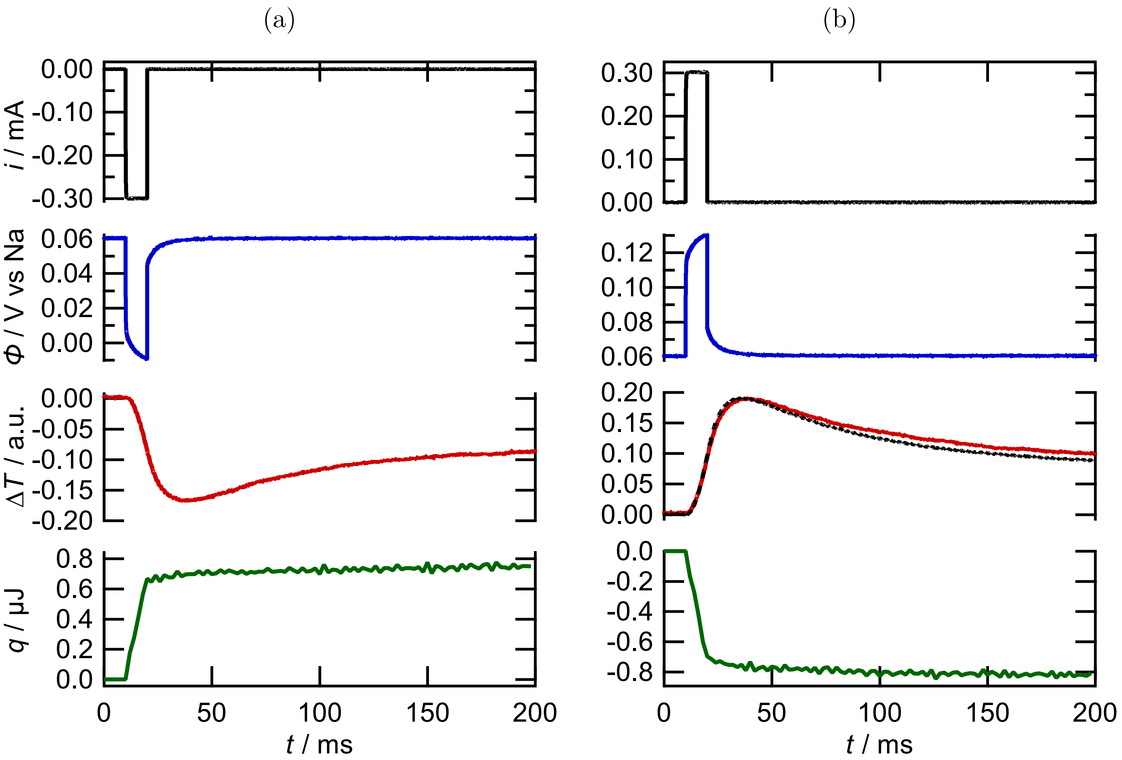

Figure 4.5: Current i, potential ϕ and temperature ΔT transients and the heat q resulting from a 10 ms (a) sodiation and (b) desodiation pulse of a thin HC electrode (20 µm) at a SoC of 74 % in 1 M $NaClO_4$/PC. The black dashed line is the thermal response to 10 ms blue laser irradiation with an adjusted amplitude.

amplitude in Figure 4.5 (b) (black dashed lined). For the laser heat input, the temperature decreased faster after its maximum. Hence, there must be ongoing heat exchange after the sodiation/desodiation pulse ($t > 20$ ms) without external current flow. This is also reflected in the heat transient (green line). More than 80 % of the heat was exchanged during the current pulse, but the heat continued to decrease/increase after the current pulse. Such a delayed heating/cooling, without external current flow, was, e.g., described by Bickel *et al.* for the electrochemical Ag deposition.[31] They explained the delayed heat with ongoing electrochemical reactions driven by discharging of the interface capacitance during equilibration of the electrode-electrolyte interface. Since significant potential relaxation was also found after the sodiation/desodiation of HC, this interpretation seems to be applicable here as well. Alternatively, a chemical process, such as the slow desolvation of Na^+ ions, which are incorporated in the SEI during the electrochemical process, could lead to delayed heat exchange.[36] A detailed analysis of the sodiation of HC with short current pulses will be given in chapter 4.4.2.

As outlined in the experimental section in chapter 3.1 the heat measured with the microcalorimetric pulse measurements consists of the reversibly exchanged heat (Peltier heat) and the polarization heat, which depends linearly on the overpotential

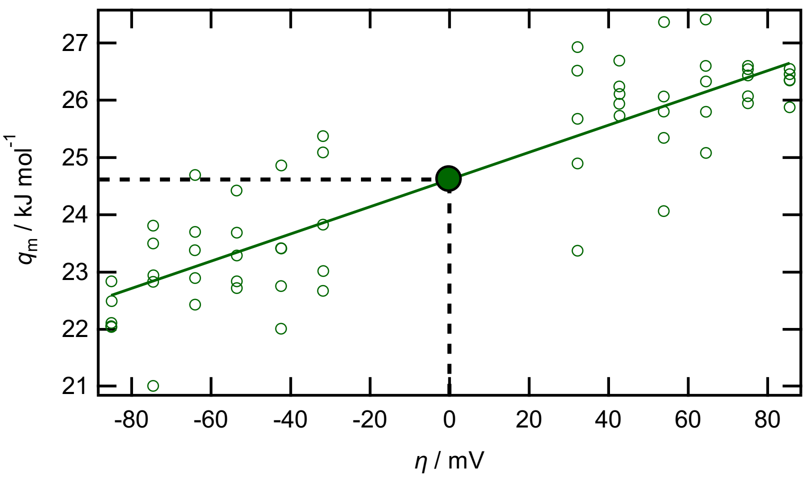

Figure 4.6: Molar heat obtained for the sodiation/desodiation of a thin HC electrode (20 µm) in 1 M $NaClO_4$/PC at an OCV of 60 mV (SoC 74 %) at $t = 100$ ms with current pulses with alternating amplitudes (±150 µA to ±400 µA). With interpolation to $\eta = 0$ V the reversibly exchanged molar heat upon sodiation of HC at this SoC is found.

η (compare equation 3.3). The reversibly exchanged molar heat can be separated by measuring the molar heat at different current pulse amplitudes, i.e., different overpotentials, and subsequent interpolation to zero overpotential. In Figure 4.6 the molar heat exchanged up to $t = 100$ ms obtained for 60 current pulses with alternating amplitudes, ranging from ±150 µA to ±400 µA, is shown dependent on the overpotential. With the linear interpolation to zero overpotential, a reversibly exchanged molar heat of $q_{m,rev} = 24.6\,\mathrm{kJ\,mol^{-1}}$ was determined at a SoC of 74 %. Note that the experimental scattering is visually exaggerated, as the y-axis spans a heat interval of only 6 kJ mol^{-1}.

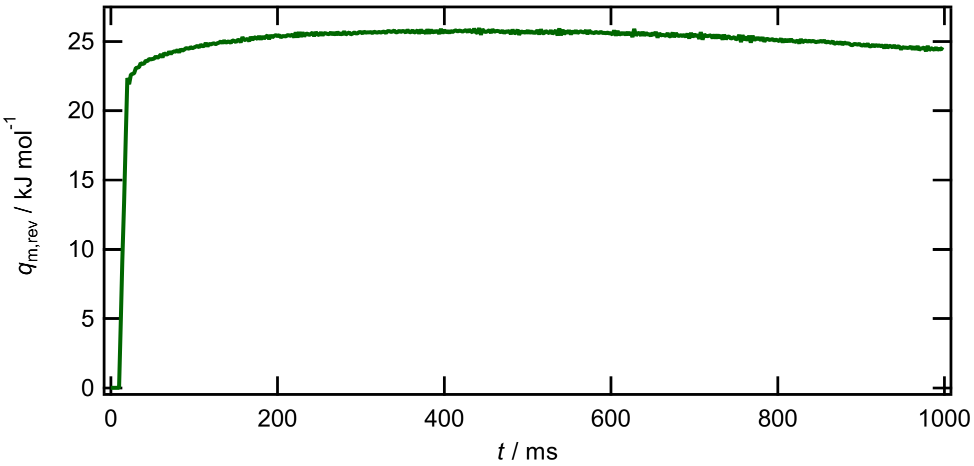

Figure 4.7: Reversibly exchanged molar heat $q_{m,rev}$ as a function of time upon 10 ms sodiation/desodiation pulses of a thin HC electrode (20 µm) in 1 M $NaClO_4$/PC at a SoC of 74 % and an OCV of 60 mV.

The signals of the microcalorimetric pulses were recorded up to $t = 1000$ ms and the heat upon a single pulse was reconstructed in 2 ms time steps from 0 ms to

1000 ms. Subsequently, the interpolation procedure with the molar heat values at $t = 0$ ms to 1000 ms was repeated to yield the the time-dependent reversibly exchanged molar heat $q_{\mathrm{m,rev}}(t)$. It should be noted that this procedure is only justified, when the charging/discharging process is equally advanced at all points of time, i.e., that the relaxation times are independent of the direction of the reaction (see Ref.[36]). For the sodiation/desodiation of HC with short current pulses this can be assumed, due to two reasons. The 10 ms current pulses only cause a minor perturbation to the equilibrium state (the SoC is only changed by about 10^{-5} of the full capacity), i.e., a near equilibrium process is considered. In addition, the potential response and the temperature transients are reversed almost quantitatively by switching between charging and discharging, which indicates a highly reversible reaction. In Figure 4.7 $q_{\mathrm{m,rev}}(t)$ is shown for the thin HC electrode at a SoC of 74 % and an OCV of 60 mV. Similar to the heat transient upon a single pulse discussed above, the main contribution to $q_{\mathrm{m,rev}}$ is exchanged during the pulse ($t = 10$ ms to 20 ms). At about $t = 400$ ms $q_{\mathrm{m,rev}}$ approached a steady value. For $t > 400$ ms, $q_{\mathrm{m,rev}}$ slightly decreases which is ascribed to thermal drift progressively disturbing the measurement with increasing time. In the following $q_{\mathrm{m,rev}}(400\,\mathrm{ms})$, which is 25.8 kJ mol^{-1} in the shown example, is used as the total reversibly exchanged molar heat of the sodiation process of HC.

Entropy of Transport

	$\hat{Q}_+$/kJ mol^{-1}	$\hat{Q}_-$/kJ mol^{-1}	$\Delta_{\mathrm{T}}S$/J mol^{-1} K^{-1}
1 M $NaClO_4$/PC (+FEC)[29]	1.6	1.9	-1
1 M $NaPF_6$/diglyme[29]	14.2	18.3	-18
1 M $NaPF_6$/EC,PC + FEC	1.9	4.9	-10

Table 4.1: Heats of transport $\hat{Q}_i$ of the anions and cations and the resulting entropy of transport $\Delta_{\mathrm{T}}S$ of the electrolyte solutions used in the microcalorimetric experiments.

In chapter 2.2.1 it was shown, that the entropy of transport $\Delta_{\mathrm{T}}S$ has to be added to the reversibly exchanged molar heat, in order to determine the reaction entropy $\Delta_{\mathrm{R}}S$ (cf. equation 2.8). The entropy of transport can be estimated with equation 2.9 and 2.10. The values for the electrolyte solutions used in this work are shown in Table 4.1. For the 1 M $NaClO_4$/PC and the 1 M $NaPF_6$/diglyme electrolyte solution, the values calculated by Karcher *et al.* were used.[29] For the 1 M $NaPF_6$/EC,PC+FEC electrolyte solution, $\varepsilon_r = 77.6$ [70], $\frac{\partial \varepsilon_r}{\partial T} = -0.385\,\mathrm{K}^{-1}$ [71] and $\eta = 6.77\,\mathrm{mPa\,s}$, $D(\mathrm{PF_6}^-)=2.4 \times 10^{-10}\,\mathrm{m^2s^{-1}}$, $D(\mathrm{Na}^+)=0.94 \times 10^{-10}\,\mathrm{m^2s^{-1}}$, $t^+ = 0.281$ and $t^- = 0.719$ [72] were used to calculate $\Delta_{\mathrm{T}}S$. Note that those parameters weren't found for the exact same composition of the electrolyte solution, so that the resulting entropy of transport has to be regarded as an approximation.

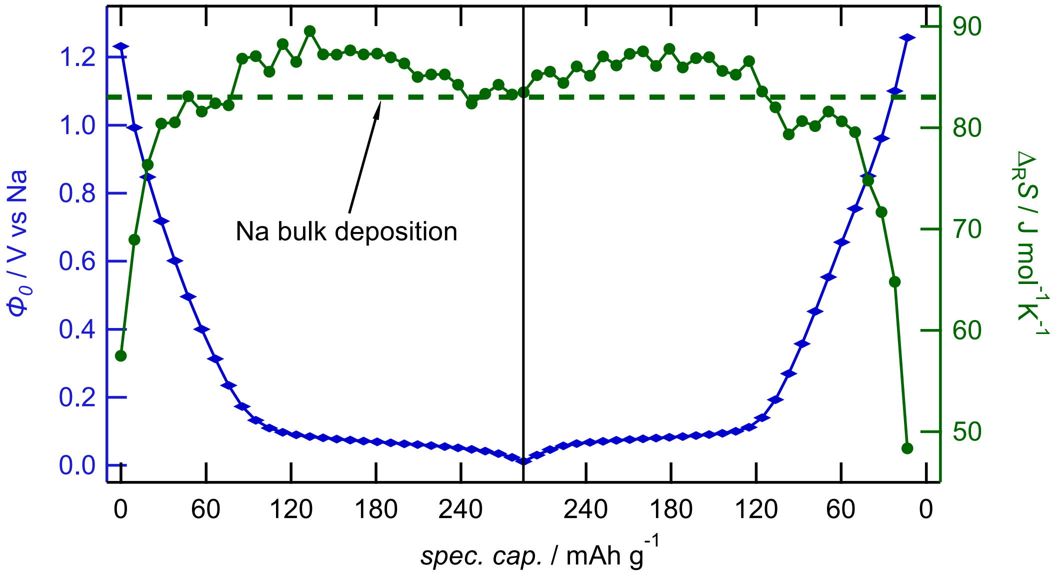

Figure 4.8: Reaction entropy $\Delta_{\mathrm{R}}S$ and equilibrium potential ϕ_0 in the 8th charging/discharging cycle of a thin HC electrode (20 µm) in 1 M $NaClO_4$/PC. The reaction entropy of Na metal deposition from 1 M $NaClO_4$/PC ($83\,\mathrm{J\,mol^{-1}\,K^{-1}}$[29]) is indicated for comparison with the horizontal dashed line.

With the reversibly exchanged molar heat and the entropy of transport, the reaction entropy of the sodiation of HC was determined for the above discussed example at a SoC of 74 % to be $\Delta_{\mathrm{R}}S = 85\,\mathrm{J\,mol^{-1}\,K^{-1}}$. The reaction entropy for all SoCs in the 8th charging and discharging cycle of a thin HC electrode in 1 M $NaClO_4$/PC is shown together with the equilibrium potential in Figure 4.8. The reaction entropy increases steeply with increasing SoC and then reaches a broad maximum between $40\,\mathrm{mAh\,g^{-1}}$ and $280\,\mathrm{mAh\,g^{-1}}$. The reversed behavior was found in the discharging cycle. In the broad maximum, the reaction entropy varies between $80\,\mathrm{J\,mol^{-1}\,K^{-1}}$ and $90\,\mathrm{J\,mol^{-1}\,K^{-1}}$, very close to the reaction entropy for Na metal deposition from the same electrolyte solution ($83\,\mathrm{J\,mol^{-1}\,K^{-1}}$,[29] shown with the dashed line in Figure 4.8). The reaction entropy obtained in the 2nd charging/discharging cycle resembles the one obtained in the 8th charging/discharging cycle (see Figure 4.38 and the discussion in chapter 4.5.4). Hence, in the following, the results of the 8th charging/discharging cycle are presented and discussed.

4.2.2 Influence of the Electrolyte Solution

Karcher *et al.* found that the reaction entropy of Na metal deposition is highly dependent on the electrolyte solution, in particular on the solvent.[28, 36] Thus, the microcalorimetric measurements of the sodiation of the thin HC electrode were repeated with different electrolyte solutions. The results are shown in Figure 4.9 and are compared with the reaction entropies for the Na metal deposition from the respective electrolyte solutions ($83\,\mathrm{J\,mol^{-1}\,K^{-1}}$ for 1 M $NaClO_4$/PC,[29] $113\,\mathrm{J\,mol^{-1}\,K^{-1}}$

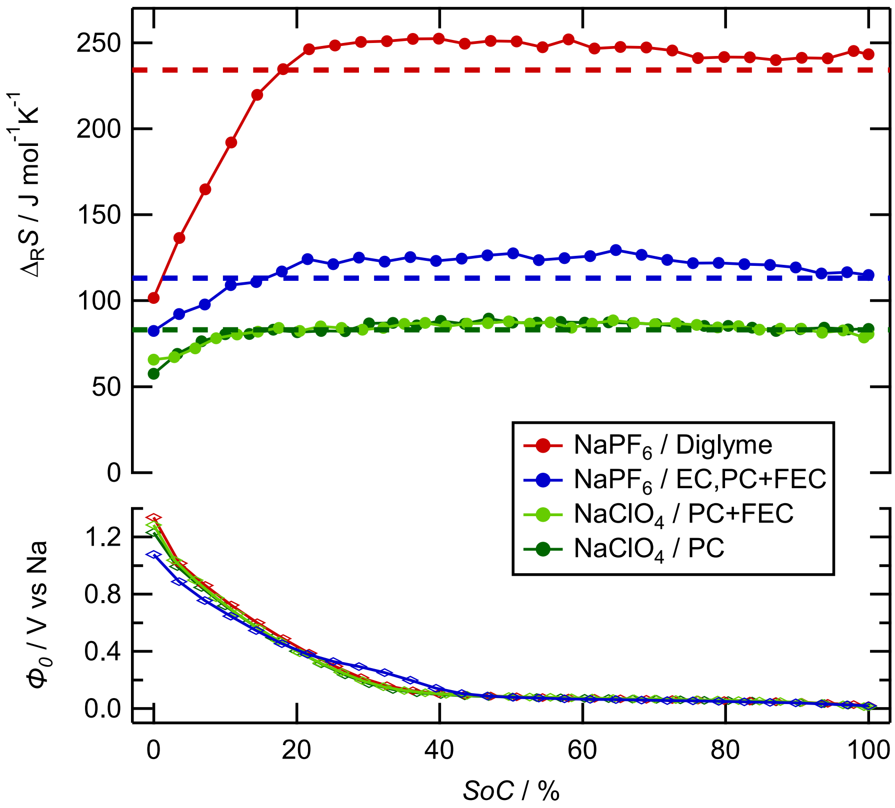

Figure 4.9: Comparison of the reaction entropy $\Delta_R S$ and ϕ_0 in the charging cycle of a thin HC electrode (20 µm) in 1 M NaPF$_6$/diglyme, 1 M NaPF$_6$/EC,PC+FEC, 1 M NaClO$_4$/PC and 1 M NaClO$_4$/PC+FEC electrolyte solution. The reaction entropies of Na metal deposition from the respective electrolyte solutions are indicated with the horizontal dashed lines.

for 1 M NaPF$_6$/EC,PC+FEC (see chapter 3.1.3) and 234 J mol^{-1} K^{-1} for 1 M NaPF$_6$ /diglyme[29]).

As expected, $\Delta_R S$ of the sodiation of HC is strongly influenced by the electrolyte solution. This is attributed to the differences of the solvation shell of the Na$^+$ ions in the different electrolyte solutions, as it will be described in detail in chapter 4.4.1. For instance, for the fully sodiated HC, $\Delta_R S$ in 1 M NaPF$_6$/diglyme is three times as large as in 1 M NaClO$_4$/PC. Nevertheless, the variation of the entropy with the SoC is similar for the different electrolyte solutions. From 0 % to 20 % SoC the reaction entropy increases, with the steepest and largest increase found for the 1 M NaPF$_6$/diglyme electrolyte solution. This is followed by a broad maximum for SoCs above 20 %, with entropy values close to the one found for Na metal deposition from the respective electrolyte solution. The addition of 2 wt % FEC to the 1 M NaClO$_4$/PC electrolyte solution didn't influence the reaction entropy (compare bright and dark green in Figure 4.9). Consequently, the microcalorimetric results for HC in 1 M NaClO$_4$/PC electrolyte solution with and without the additive FEC will be considered together.

4.2.3 Measurements with Thick Hard Carbon Electrodes

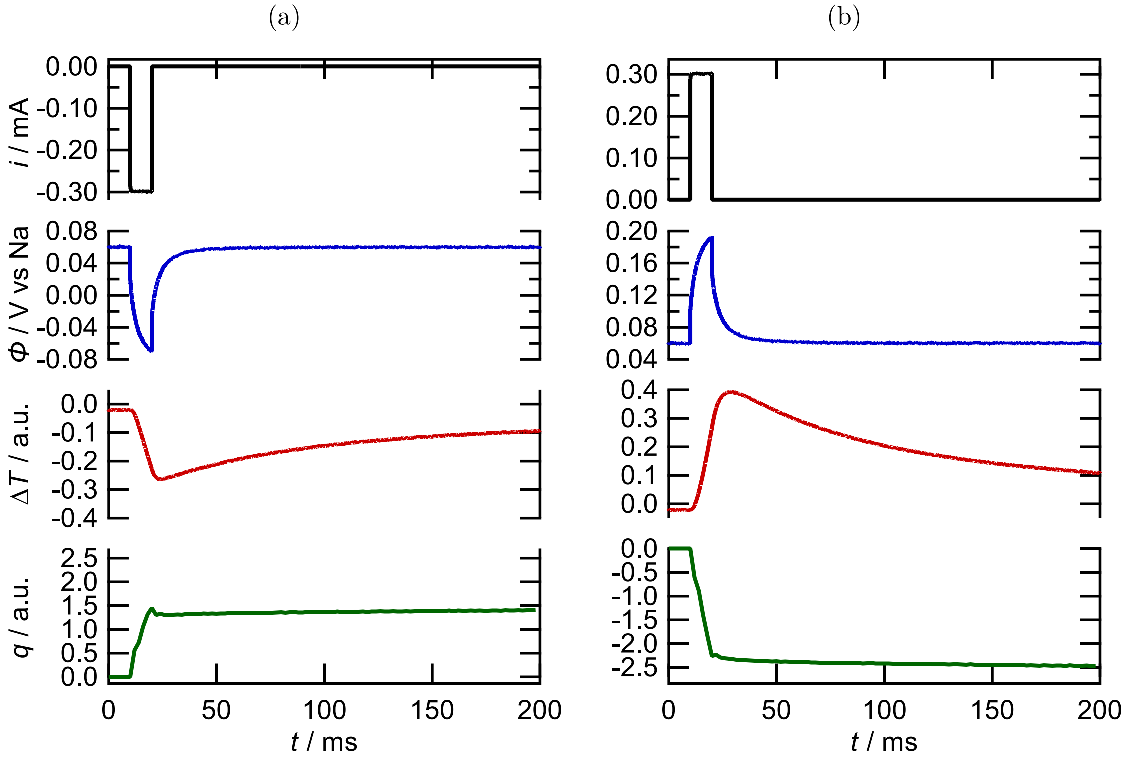

Figure 4.10: Current i, potential ϕ and temperature ΔT transients and the heat q resulting from a 10 ms (a) sodiation and (b) desodiation pulse of a thick HC composite electrode (46 µm) at a SoC of 74 % in 1 M $NaPF_6$/EC,PC+FEC.

The microcalorimetric results shown hitherto were obtained with the thin spray-coated HC electrodes, which were specifically made for the usage in the electrochemical microcalorimeter as described by Palanisamy *et al.*[38] A Cu current collector was used for good thermal and electric conductivity, the coating was only sprayed onto the center part of the current collector, so that the edge could be used for the electric connection, and most importantly the final thickness of the coating was reduced to 20 µm to ensure fast heat transfer to the sensor. However, in practical applications of SIBs thicker HC electrodes with higher mass loading and Al current collectors are used. Such composite electrodes were prepared within the POLiS Cluster of Excellence as material for a SIB reference system,[40] to enhance the comparability between the results obtained with different experimental methods, which is crucial to allow for multiscale studies.[65]

In order to assess the influence of the HC composite electrode on the microcalorimetric measurements, the experiments were repeated with the thick HC electrodes of the SIB reference system of the POLiS Cluster of Excellence. The HC composite was 46 µm thick and HC material from the same supplier as the one employed in the spray-coated electrodes was used (the exact composition and preparation is described in chapter 3.3). Al foil was used as current collector. The electrolyte solution was 1 M $NaPF_6$/EC,PC+FEC, which is the electrolyte solution for the SIB reference system.

In Figure 4.10 the current, potential, temperature and heat transients of an exemplary (a) sodiation and (b) desodiation pulse at a SoC of 74 % are shown. The general characteristics of the transients are rather similar to the ones obtained with the thinner electrodes (cf. Figure 4.5). After the current is switched off, the potential relaxes toward its initial potential in around 50 ms and cooling was observed during sodiation and heating during desodiation. However, the overpotential during the pulse is almost doubled compared to the pulses with the thin HC electrodes. This leads to more overpotential heating, which is directly reflected in the temperature and the heat transients. The amplitude of the temperature minimum during sodiation is significantly smaller than the temperature maximum during desodiation. Although it might be expected that the heat exchange is delayed due to, e.g., slow diffusion in the thick electrode, the heat transients indicate that almost the complete heat was already exchanged during the pulse.

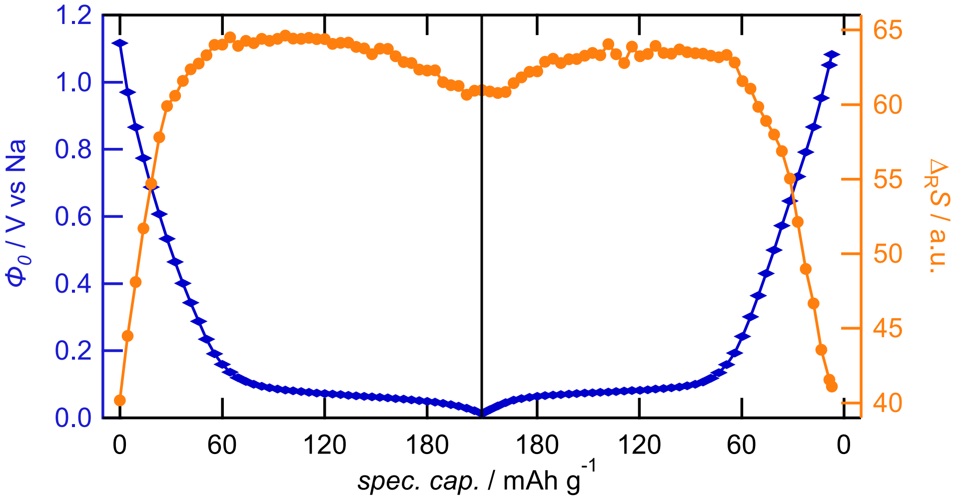

Figure 4.11: Reaction entropy $\Delta_R S$ in arbitrary units and equilibrium potential ϕ_0 in the 6th charging/discharging cycle of a thick HC electrode (46 µm) in 1 M $NaPF_6$/EC,PC+FEC. Due to experimental difficulties a reliable calibration of the values of $\Delta_R S$ was not possible.

As already discussed in chapter 3.1.3 an exact calibration of the microcalorimetric experiments with the thick HC electrodes was not possible, since the heat exchange upon Na metal plating/stripping on the overcharged, thick HC electrode was not completed within the measurement time of 1000 ms. Still, the change of the reaction entropy with the SoC can be qualitatively discussed and an estimation of the absolute values can be given. In Figure 4.11 the reaction entropy in arbitrary units together with the equilibrium potential is shown for the charging and the discharging cycle. It can be clearly seen, that the variation of the reaction entropy with the SoC resembles the ones measured for the thin HC electrodes with different electrolyte solutions. The steep increase at low SoCs is followed by a broad maximum during charging and the reversed behavior is found during discharging. From the calibration it was estimated that $\Delta_\mathrm{R}S = 60\,\mathrm{a.u.}$ corresponds to a value of $(96 \pm 35)\,\mathrm{J\,mol^{-1}\,K^{-1}}$. This means that the broad maximum of $\Delta_\mathrm{R}S$ is also close to the value found for Na metal deposition from the respective electrolyte solution ($113\,\mathrm{J\,mol^{-1}\,K^{-1}}$, see chapter 3.1.3). Ultimately, it can be said that although a reliable calibration of the microcalorimetric experiments with the the thick HC electrodes was not possible, the variation of $\Delta_\mathrm{R}S$ with the SoC and the magnitude of the obtained values is in accordance with the results obtained for the thin HC electrodes.

4.3 Entropy Profiling with Temperature Steps

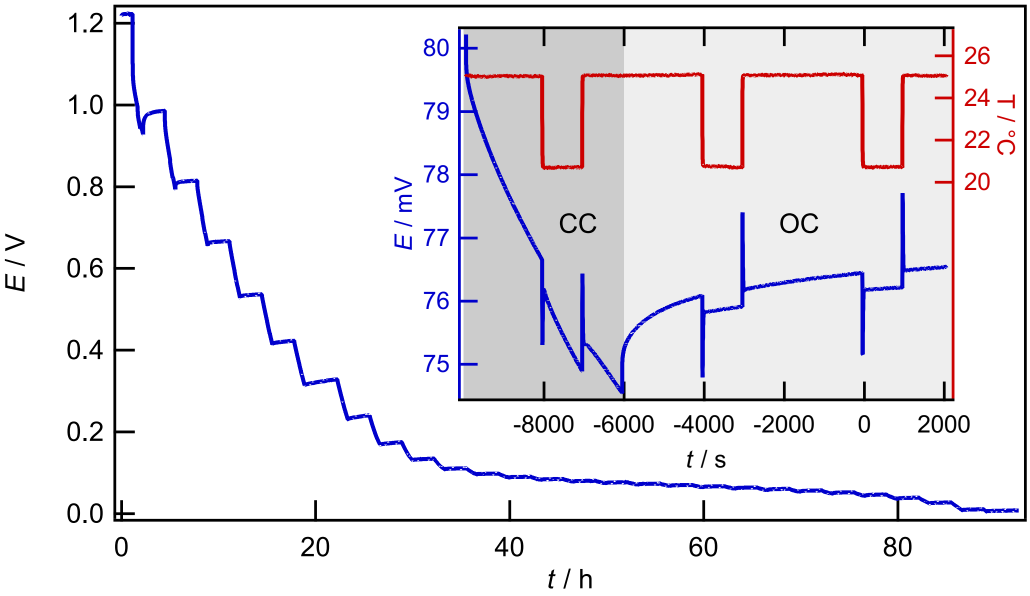

Figure 4.12: Cell voltage of a HC|Na metal cell during the GITT-type charging with a charging rate of about 0.05 C. The CC phases are followed by OC phases, as depicted in the inset, in which also the temperature of the cell block is shown. The curve in the inset is x-shifted, so that $t = 0$ s at the second negative temperature step in the OC phase.

As already mentioned, the cell reaction entropy of an electrochemical cell can be determined from the temperature coefficient of the equilibrium cell voltage. This approach is commonly called entropy profiling. In the following, such experiments with HC|Na metal coin cells are presented. In contrast to typical entropy profiling studies where changing the temperature of the cell takes more than 10 min, herein the temperature of the coin cell is changed within less than one minute.

Before the HC|Na metal coin cells were used for the temperature step experiments, they were cycled galvanostatically 5 times between 0.005 V and 2.0 V with a rate of 0.1 C. Subsequently, a GITT-type charging protocol with a lower voltage limit of 0.005 V and an upper voltage limit of 2.0 V, similar to the one used for the microcalorimetric experiments, was applied. In the charging/discharging phases a rate of 0.05 C was used. During the OC phases the temperature was varied by switching between the water of the two thermostats (see chapter 3.2). The resulting cell voltage in the charging cycle is shown in Figure 4.12. In the inset an exemplary CC and OC phase is depicted together with the temperature of the cell block. The current was applied for 3900 s and afterwards the cell was set to OC conditions for 8100 s. During the OC phase the temperature was switched twice between the upper and lower temperature. The phases at the lower temperature lasted 1000 s. In the following, only the cell voltage response to the second negative temperature step (at $t = 0$ s) at the different SoCs is shown and discussed.

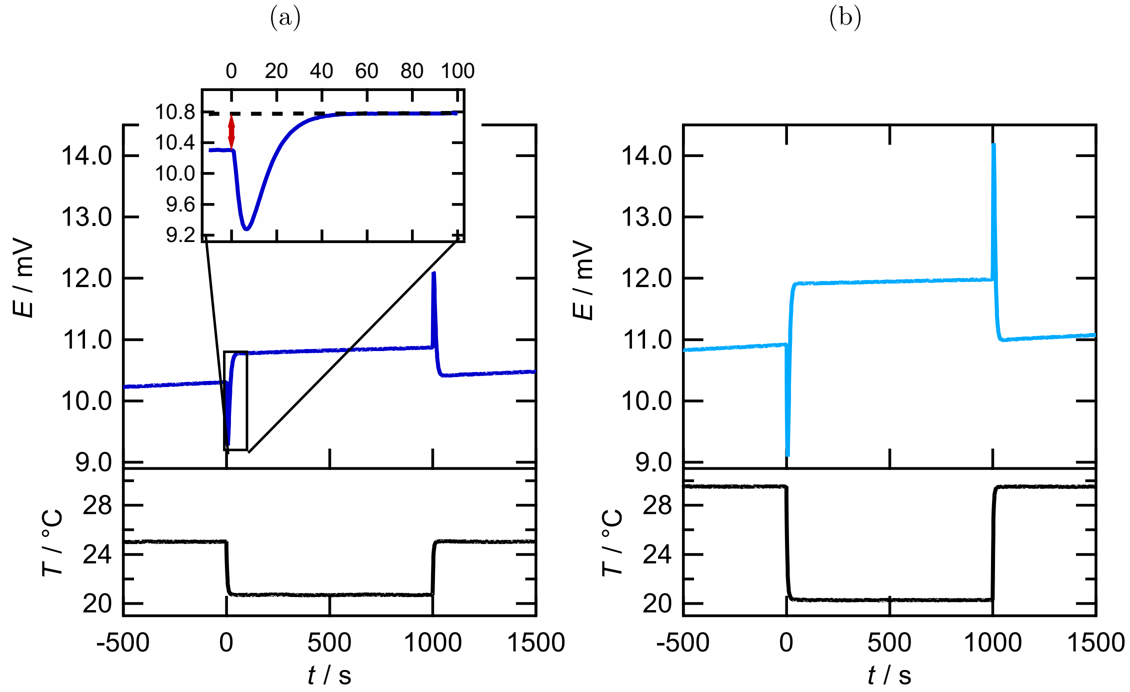

Figure 4.13: Cell voltage transients of a HC|Na metal cell at OC conditions at a SoC of 99 % in the charging cycle due to the shown temperature steps of (a) $\Delta T = -4.3\,\mathrm{K}$ and (b) $\Delta T = -9.2\,\mathrm{K}$. The black dashed line in the inset indicates the cell voltage drift at the lower temperature (linear fit from $t = 300\,\mathrm{s}$ to $t = 1000\,\mathrm{s}$). The red arrow shows the cell voltage difference ΔE_0 used for the determination of $\Delta_\mathrm{R} S_\mathrm{cell}$.

In Figure 4.13 the variations of the OCV of a fully sodiated HC|Na metal cell due to temperature steps with different heights ((a) $\Delta T = -4.3\,\mathrm{K}$ and (b) $\Delta T = -9.2\,\mathrm{K}$) are shown. For $t > 60\,\mathrm{s}$ the voltage reached a new plateau, 0.46 mV and 0.98 mV higher than the initial plateau for the small and the large temperature step respectively. Immediately after the temperature change, sharp negative voltage spikes with a minimum of (a) $-1.0\,\mathrm{mV}$ and (b) $-1.8\,\mathrm{mV}$ at $t = 6\,\mathrm{s}$ occurred. These sharp voltage spikes can most likely be attributed to temperature gradients inside the coin cells during switching of the temperature, which will be discussed in detail in chapter 4.4.3. The steady state voltage change for $t > 60\,\mathrm{s}$ is presumably linked to the reaction entropy of the complete HC|Na metal cell, which is correlated to the temperature coefficient of the equilibrium cell voltage by equation 2.2. Independent of the height of the temperature step a reaction entropy of $-10.3\,\mathrm{J\,mol^{-1}\,K^{-1}}$ was determined for both experiments shown in Figure 4.13. At $t \geq 1000\,\mathrm{s}$, when the temperature step is reversed, the voltage variation reverses correspondingly. Such voltage transients were typical for all SoCs in the plateau region (30 % to 100 %). About 60 s after the temperature was switched, a steady state voltage was reached and with the well-defined voltage shifts the cell reaction entropy could be determined. Values between $-10\,\mathrm{J\,mol^{-1}\,K^{-1}}$ and $6\,\mathrm{J\,mol^{-1}\,K^{-1}}$ were found and will be discussed in detail in chapter 4.4.1.

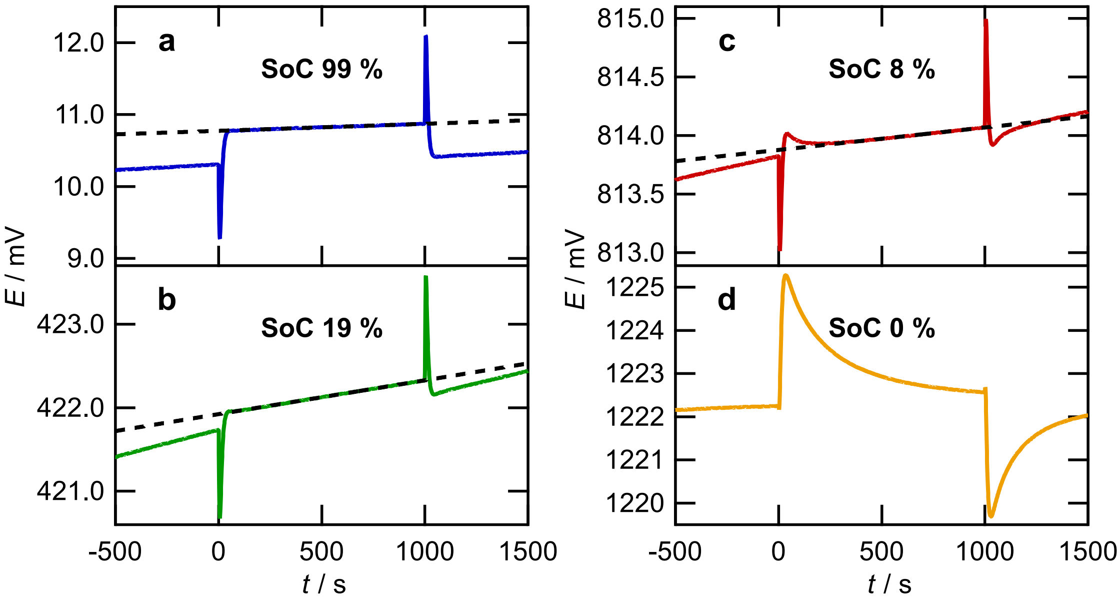

Figure 4.14: Cell voltage transients of a HC|Na metal cell at OC conditions at different SoCs in the charging cycle due to temperature steps with $\Delta T = -4.3\,\mathrm{K}$ (cf. with Figure 4.13 (a)). The dashed lines in (a)-(c) indicate the OCV drift at the lower temperature (linear fit from $t = 300\,\mathrm{s}$ and $t = 1000\,\mathrm{s}$).

However, at SoCs in the sloping region (below 30 %) the characteristics of the cell voltage response changed, as it can be seen in Figure 4.14. At 19 % SoC (Fig. 4.14 (b)), the overall shape of the cell voltage response (sharp spike followed by a plateau) remained the same, but the drift of the OCV increased to about $0.6\,\mathrm{\mu V\,s^{-1}}$. This made a clear identification of the temperature-induced cell voltage shift difficult. At a SoC of 8 % (Fig. 4.14 (c)) an additional small maximum at around $t = 40\,\mathrm{s}$ evolved, which leveled off for $t > 300\,\mathrm{s}$. With decreasing SoC this maximum became even more pronounced and at a SoC of 0 % (Fig. 4.14 (d)) it dominated the cell voltage response. The initial, sharp voltage minimum almost vanished and a new voltage plateau was not reached within 1000 s. In conclusion, the cell voltage response strongly depends on the SoC of the HC electrode and the deviations from ideal stepwise behavior can be divided into three characteristics: (I) drift of the OCV on a long timescale, (II) a sharp voltage spike for $t < 10\,\mathrm{s}$ after the temperature step and (III) a wide maximum ca. 40 s after the temperature step, which evolves at lower SoCs and dominates the voltage response at 0 % SoC. Upon reversal of the temperature step at $t = 1000\,\mathrm{s}$, the sign of the extrema is changed. The reason of these characteristics of the cell voltage response will be discussed with a simple model including temperature gradients across the coin cell as well as different kinetics at the HC and the Na metal electrode in chapter 4.4.3. The influence of the drift of the OCV and how it can be corrected for will be examined in the following paragraph.

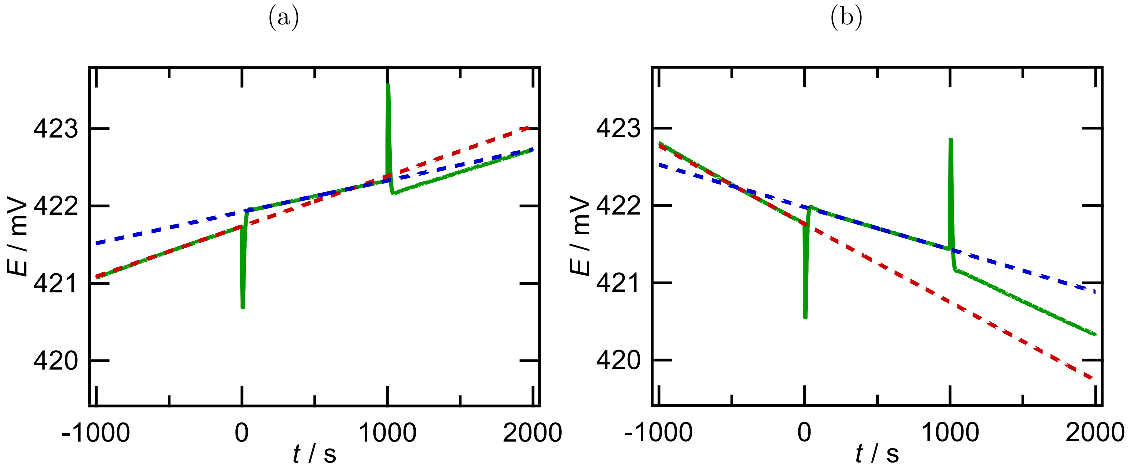

Figure 4.15: Cell voltage transients at OC conditions at an SoC of 19 % due to temperature steps during the (a) charging cycle and the (b) discharging cycle. The red dashed lines indicate the drift of the cell voltage at the initial temperature (25.0 °C, linear fit from $t = -500\,\mathrm{s}$ to $t = 0\,\mathrm{s}$), and the blue dashed lines the drift at the lower temperature (20.7 °C, linear fit from $t = 300\,\mathrm{s}$ to $t = 1000\,\mathrm{s}$).

Drift of the OCV

At SoCs in the sloping region (0-30 %), the exact determination of the cell reaction entropy was impeded by the drift of the OCV, which was significant even 6000 s after the charging/discharging was stopped. To discuss this problem, the cell voltage transients at a SoC of 19 % measured during the (a) charging cycle and the (b) discharging cycle are exemplarily shown in Figure 4.15. In both cases, upon switching the temperature, the cell voltage exhibits a sharp voltage spike before at $t > 60\,\mathrm{s}$ a linear regime is reached. With the dashed lines the drift of the OCV at the initial temperature (red, linear fit from $t = -500\,\mathrm{s}$ to $t = 0\,\mathrm{s}$) and the lower temperature (blue, linear fit from $t = 300\,\mathrm{s}$ to $t = 1000\,\mathrm{s}$) is indicated. While the drift of the OCV is positive in the charging cycle, it is negative in the charging cycle. Independent of the direction of the drift of the OCV, it is less steep, when the cell is at the lower temperature ($0.4\,\mu\mathrm{V\,s^{-1}}$ vs. $0.6\,\mu\mathrm{V\,s^{-1}}$ during the charging cycle and $-0.5\,\mu\mathrm{V\,s^{-1}}$ vs. $-1.0\,\mu\mathrm{V\,s^{-1}}$ during the discharging cycle). The temperature dependence of the drift of the OCV is expected, as it is presumably caused by thermally activated equilibration processes, such as, e.g., the equilibration of concentration gradients of the Na species in the HC particles by diffusion processes. In addition, when the temperature is switched back to the initial temperature at $t > 1000\,\mathrm{s}$, the slope of the drift is approaching its initial value, so that the red dashed lines in Figure 4.15 (a) and (b) are nearly parallel to the courses of the cell voltage for $t > 1000\,\mathrm{s}$.

For the determination of the cell reaction entropy, the deteriorations by drift of the OCV as well as by the maximum, which evolved at SoCs $\leq 8\,\%$, have to be separated from the temperature-induced shift of the equilibrium cell voltage. This was achieved by extrapolating the cell voltage at the lower temperature to $t = 0\,\mathrm{s}$

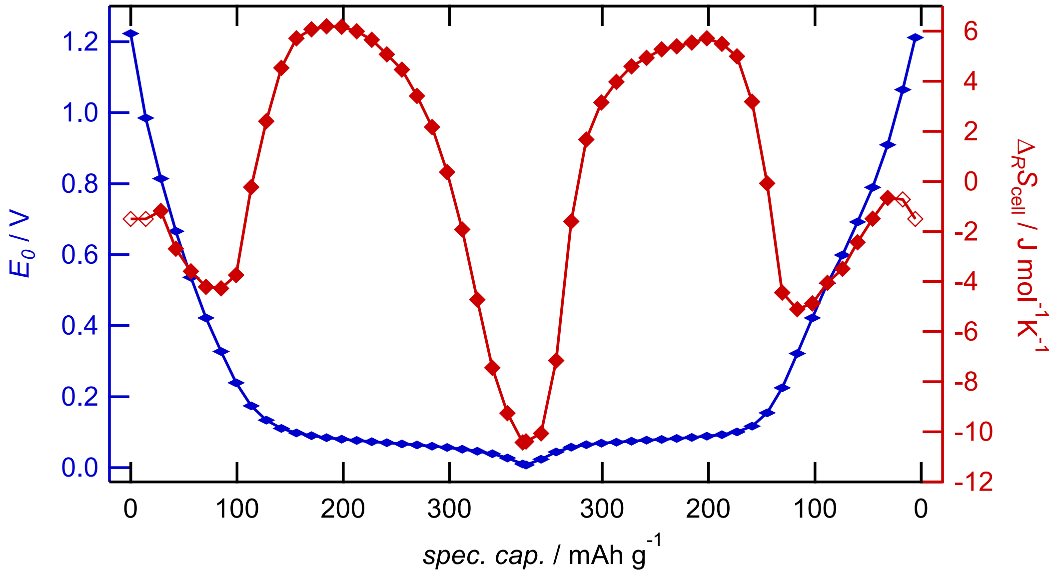

Figure 4.16: Cell reaction entropy and the equilibrium cell voltage E_0 from the temperature step experiment of a HC|Na metal coin cell with 1 M $NaPF_6$/diglyme in the charging and the discharging cycle. The data points of the entropy at 0 % and 4 % SoC (shown with an empty diamond) could only be estimated, since a linear regime of the cell voltage was not reached within 300 s after the temperature step (details see text).

with a linear fit between $t = 300\,\mathrm{s}$ to $t = 1000\,\mathrm{s}$, which is indicated in Figure 4.14 (a)-(c) with the black dashed lines. This time interval was chosen, since for all SoCs $\geq 8\,\%$ the cell voltage reached a linear regime for $t > 300\,\mathrm{s}$. The difference between the linear fit and the measured cell voltage at $t = 0\,\mathrm{s}$ was subsequently used for the determination of the cell reaction entropy (illustrated in the inset in Figure 4.13a). For SoCs below 8 %, the cell voltage didn't reach a linear regime within the measurement time and $\Delta_\mathrm{R} S_\mathrm{cell}$ couldn't be evaluated. The cell reaction entropy could only be estimated from experiments with prolonged waiting time (3500 s) at the colder temperature. It lies in the range of $-7\,\mathrm{J\,mol^{-1}\,K^{-1}}$ to $4\,\mathrm{J\,mol^{-1}\,K^{-1}}$ and $-5\,\mathrm{J\,mol^{-1}\,K^{-1}}$ to $2\,\mathrm{J\,mol^{-1}\,K^{-1}}$ for 0 % and 4 % SoC, respectively.

The resulting cell reaction entropy $\Delta_\mathrm{R} S_\mathrm{cell}$ for SoCs $\geq 8\,\%$ is shown together with the equilibrium cell voltage E_0 for the charging and discharging cycle in Figure 4.16. With increasing SoC the cell reaction entropy initially reaches a minimum ($-4\,\mathrm{J\,mol^{-1}\,K^{-1}}$), ensued by a maximum ($6\,\mathrm{J\,mol^{-1}\,K^{-1}}$) and ultimately reaching its lowest value of about $-10\,\mathrm{J\,mol^{-1}\,K^{-1}}$ when the HC was fully sodiated. In the discharging cycle, the same trend could be observed, but at low SoCs the absolute values of the reaction entropy were slightly below the ones measured in the charging cycle. This is ascribed to the remaining influence of the drift of the OCV, discussed above. In Figure C.4 the cell reaction entropy obtained by the application of a larger temperature step ($\Delta T = -9.2\,\mathrm{K}$, cf. Figure 4.13) is shown. In addition, the results of two different HC|Na metal coin cells are compared in Figure C.4. The deviations between the measurements are below 1 J mol^{-1} K^{-1}, demonstrating high repeatability and reproducibility of the method.

Comparison with other Entropy Profiling Studies of HC|Na Metal Cells

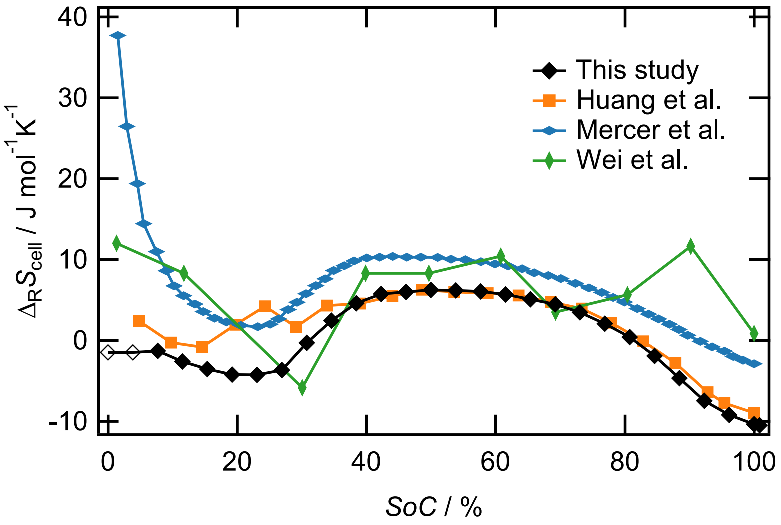

Figure 4.17: Comparison of the cell reaction entropy of different HC|Na metal cells obtained with entropy profiling by this study, by Mercer *et al.*,[61] Huang *et al.*,[63] and Wei *et al.*[64]. The data points of the cell reaction entropy of this study at 0 % and 4 % SoC (shown with an empty diamond) could only be estimated.

In Figure 4.17 the cell reaction entropy of HC|Na metal cells obtained with entropy profiling by Mercer *et al.*,[61] Huang *et al.*,[63] and Wei *et al.*[64] is compared with the results of this study. In all studies different electrolyte solutions and HC materials were used. The influence of the electrolyte solution on the cell reaction entropy should be negligible, since solvation/desolvation effects are not reflected (see discussion in chapter 4.4.1). In contrast, the HC material may influence the results, as the ratio between defects, graphitic domains and pores might differ among the HC materials. As described before, in this study, the temperature of the cell was changed within less than one minute by switching between two thermostats (described in chapter 3.2). This is in contrast to the cited studies, in which only one thermostat or one measurement chamber was used and changing the cell temperature took at least 10 min. Additionally, different resting periods after changing the SoC and before changing the temperature, ranging from 20 min (Mercer *et al.*) up to 120 min (Wei *et al.*), were applied. Despite all these experimental differences, the results of all four studies agree fairly well at SoCs above 10 %. The results of Wei *et al.* show a significant spread, which might be caused by a high level of noise in their voltage signal, as well as OCV drift interfering with their measurement, which took more than 10 h at each SoC.[64] Similar variation of the cell reaction entropy was found by Mercer *et al.*, Huang *et al.* and in this study, i.e., a minimum at around 20 %

SoC is followed by a broad maximum from 20 to 100 %. The absolute values found by Mercer *et al.* are up to $10\,\mathrm{J\,mol^{-1}\,K^{-1}}$ higher than the ones found by Huang *et al.* and this study. This deviation significantly increases at SoCs below 10 %, which might be a result of increasing OCV drift or sluggish kinetics of the sodiation of HC at these SoCs rendering the determination of the cell reaction entropy difficult. This will be elucidated in detail in chapter 4.4.3.

4.4 Sodiation Entropy of Hard Carbon

In the previous chapters it was shown how the reaction entropy of sodiation of HC dependent on the SoC was determined with electrochemical microcalorimetry and entropy profiling. With electrochemical microcalorimetry the reaction entropy of the processes taking place at the HC electrode is determined. Since the heat exchanged up to $t = 0.4\,\mathrm{s}$ after the short charging/discharging pulses was used to determine the reaction entropy, only fast processes ($t \leq 0.4\,\mathrm{s}$) contributed to the reaction entropy determined with microcalorimetry. With entropy profiling the cell reaction entropy, i.e., the sum of the entropy of the processes taking place at the HC and the Na metal electrode, is measured. At SoCs $\geq 8\,\%$ the deteriorations of the cell voltage response upon the fast temperature steps leveled off within 300 s after the temperature was switched. Thus, for the determination of the cell reaction entropy, it was assumed that within 300 s after the temperature step an equilibrium state was reached. In consequence, all processes which are completed within 300 s contributed to the cell reaction entropy determined with entropy profiling.

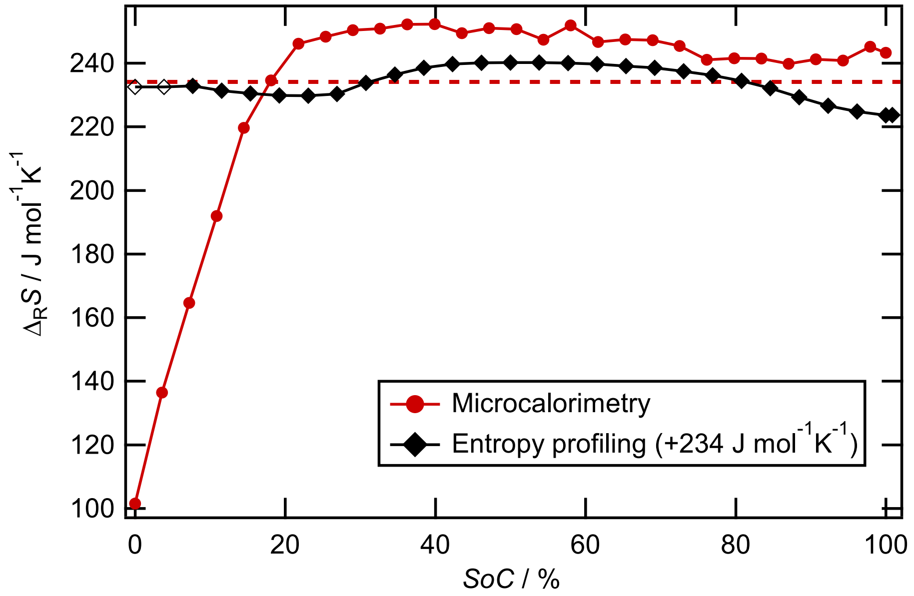

Figure 4.18: Comparison of the reaction entropy of the sodiation of HC in 1 M $NaPF_6$/diglyme in the charging cycle determined with microcalorimetry and entropy profiling, i.e., on different timescales $t \leq 0.4\,\mathrm{s}$ and $t \leq 300\,\mathrm{s}$, respectively. Since with entropy profiling only the cell reaction entropy can be obtained, it was shifted by the reaction entropy of Na metal deposition from the respective electrolyte solution, indicated with the dashed line.[29] The data points of the cell reaction entropy at 0 % and 4 % SoC (shown with an empty diamond) could only be estimated, as described in chapter 4.3.

In Figure 4.18 the reaction entropy of the sodiation of HC in 1 M $NaPF_6$/diglyme electrolyte solution obtained with microcalorimetry and entropy profiling is compared. In order to make the results comparable, the cell reaction entropy $\Delta_R S_{cell}$

(obtained by entropy profiling) was shifted by the reaction entropy of Na metal deposition from the respective electrolyte solution ($\Delta_\mathrm{R}S_\mathrm{Na} = 234\,\mathrm{J\,mol^{-1}\,K^{-1}}$[29]) to yield the HC electrode reaction entropy $\Delta_\mathrm{R}S_\mathrm{HC} = \Delta_\mathrm{R}S_\mathrm{cell} + \Delta_\mathrm{R}S_\mathrm{Na}$. As discussed in chapter 4.3 the absolute error of the cell reaction entropy determined with entropy profiling was below $1\,\mathrm{J\,mol^{-1}\,K^{-1}}$. The reproducibility of the absolute values of the reaction entropy determined in different microcalorimetric experiments was approximately $\pm 10\,\%$ caused by, e.g., uncertainties of the calibration. However, the error of the reaction entropy determined at different SoCs within one microcalorimetric experiment is much lower. The standard deviations of the linear fits used for the determination of the reversibly exchanged heat (see, e.g., Figure 4.6) were below $0.5\,\mathrm{J\,mol^{-1}\,K^{-1}}$. Consequently, the variation of the reaction entropy with the SoC could be reproduced in different microcalorimetric experiments with good precision. When comparing the reaction entropy of sodiation of HC on different timescales, two main regions can be identified. At SoCs above 20 % similar values of the reaction entropy were obtained with both methods. From a SoC of 20 % to 100 % a broad maximum of the reaction entropy was found. The absolute values of the sodiation entropy of HC are high compared to the variation of the reaction entropy with the SoC. Since the results of both methods coincide at SoCs above 20 %, it can be assumed that at these SoCs all processes, which contribute to the reaction entropy, are already completed within $t \leq 0.4\,\mathrm{s}$ (the timescale of the microcalorimetric measurements). At SoCs below 20 % the reaction entropy determined with microcalorimetry is significantly reduced compared to that obtained with entropy profiling. This indicates that at low SoCs slow processes, which are not finished within $t \leq 0.4\,\mathrm{s}$, contribute to the reaction entropy and hence are not or not fully reflected in the microcalorimetric results.

To understand the different involved processes and their contributions to the reaction entropy, the following discussion will be divided in three subchapters. First, the different contributions to the reaction entropy of the sodiation of HC will be discussed in chapter 4.4.1. The reaction entropy is divided into a contribution of the desolvation of the $\mathrm{Na^+}$ ions concomitant with the insertion into HC, and a contribution of the entropy of the Na species in the HC. The variation of the entropy of the Na species in HC with the SoC will be rationalized with a solid solution model. Subsequently, in chapter 4.4.2, the reduced reaction entropy found with microcalorimetry at SoCs below 20 % will be investigated. At these low SoCs, mainly a capacitive adsorption process is driven by the microcalorimetric current pulses, indicating slow sodiation kinetics of HC. During this adsorption process the $\mathrm{Na^+}$ ions are only partially desolvated, leading to the reduced reaction entropy. As it will be discussed in chapter 4.4.3, the slow sodiation kinetics at low SoCs are also reflected in the cell voltage responses caused by the temperature steps used for the entropy profiling experiments. A simple model, including temperature gradients across the coin cell as well as Butler-Volmer reaction kinetics at the HC and the Na metal electrode, is introduced, to simulate the variation of the single electrode potentials of the HC and the Na metal electrode, and ultimately the cell voltage response.

4.4.1 Contributions to the Sodiation Entropy of Hard Carbon

In general, the entropy change upon sodiation of HC is highly positive and depends on the electrolyte solution (cf. Figure 4.9). This can be explained by the entropy gain due to the desolvation of the Na^+ ions concomitant with the insertion, which overcompensates the entropy loss due to their fixation. Such a behavior was already found and explained by Schmid *et al.* and Karcher *et al.* for Li and Na metal deposition, respectively.[29, 73] They split the reaction entropy of the metal deposition into three components: the immobilization of the metal ions on the surface, the release of the first solvation shell, and the contribution of solvent molecules in the second and higher solvation shells, which depends on the permittivity of the solvent. The contribution of the immobilization was estimated from the entropy of freezing of the respective metal. For Na metal a value of $-37.5\,\mathrm{J\,mol^{-1}\,K^{-1}}$ was found by Karcher *et al.*[29]. With this value and the measured reaction entropy, the contribution of the desolvation of the Na^+ ions was determined to be $125\,\mathrm{J\,mol^{-1}\,K^{-1}}$ and $272\,\mathrm{J\,mol^{-1}\,K^{-1}}$ for 1 M $NaClO_4$/PC and 1 M $NaPF_6$/diglyme, respectively.[29]
The contribution of the immobilization of Na^+ ions might be different for the sodiation of HC, since it is expected that the entropy of the Na species in HC is dependent on the SoC, which will be discussed in detail in the paragraph below. On the contrary, the contribution of the desolvation in the respective electrolyte solution can presumably be adopted without any changes to the sodiation entropy of HC, when the solvation shell of the Na^+ ions is completely released upon the sodiation of HC. In the case of charging a HC|Na metal coin cell, solvation of Na^+ ions takes place at the Na metal electrode and desolvation of Na^+ ions at the HC electrode. When the Na^+ ions are completely solvated/desolvated at both electrodes, the contributions of the solvation/desolvation to the cell reaction entropy compensate for each other. Since the cell reaction entropy $\Delta_\mathrm{R}S_\mathrm{cell}$ of a HC|Na metal cell obtained with entropy profiling varies only between -10 and $6\,\mathrm{J\,mol^{-1}\,K^{-1}}$ (see Figure 4.16), the complete desolvation of Na^+ ions upon the sodiation of HC is expected within 300 s. Significantly larger variations would be expected if the Na^+ ions would only be partially desolvated at the HC electrode, due to, e.g., a solvent co-intercalation mechanism. Partial desolvation of Na^+ ions at the HC electrode would lead to a highly negative $\Delta_\mathrm{R}S_\mathrm{cell}$, since the solvation entropy is negative. Such a solvent co-intercalation mechanism is, e.g., known to take place for Na^+ ions and diglyme in graphite.[74] It was also proposed for Na^+ ions and diglyme in HC by different groups, based on transmission electron microscopy (TEM), XRD and XPS results.[58, 60, 75] How-

ever, for the herein tested HC material, the small variation of $\Delta_\mathrm{R}S_\mathrm{cell}$ contradicts such a mechanism. This is in accordance with Escher *et al.*, who measured only small volume changes of a HC electrode during charging with dilatometry.[48]

Variation of the Entropy of the Na Species in HC with the SoC

Until now, mainly the contribution of the desolvation of the Na^+ ions to the reaction entropy of the sodiation of HC was discussed. Since within 300 s the desolvation is completed at all SoCs, this contribution does not vary with the SoC. Nevertheless, a variation of the reaction entropy with the SoC was found. This can be seen in the cell reaction entropy determined with entropy profiling (cf. Figure 4.16). The cell reaction entropy does not contain contributions from the solvation/desolvation of the Na^+ ions, since the contribution of the solvation of Na^+ ions at the Na metal electrode compensates for the contribution of the desolvation of Na^+ ions at the HC electrode. Hence, the remaining variation should be rooted in the variation of the entropy of the Na species in the HC electrode dependent on the SoC. It is exactly this contribution, which might help to figure out at which sites and to which extent Na is stored in HC at the different SoCs.

Mercer *et al.* explained the variation of the cell reaction entropy with changes of the configurational entropy resulting from Na filling the interlayers and subsequently the pores of HC, starting from a simple solid solution model and adapting it to the microstructural properties of HC.[61] Since the cell reaction entropy found in this study coincides with the one by Mercer *et al.* for SoCs between 10 % and 100 % (see Figure 4.17), it stands to reason that parts of this model might as well be applicable to the herein investigated HC. Before the model of Mercer *et al.* will be described, the configurational entropy of an ideal solid solution will be explained.

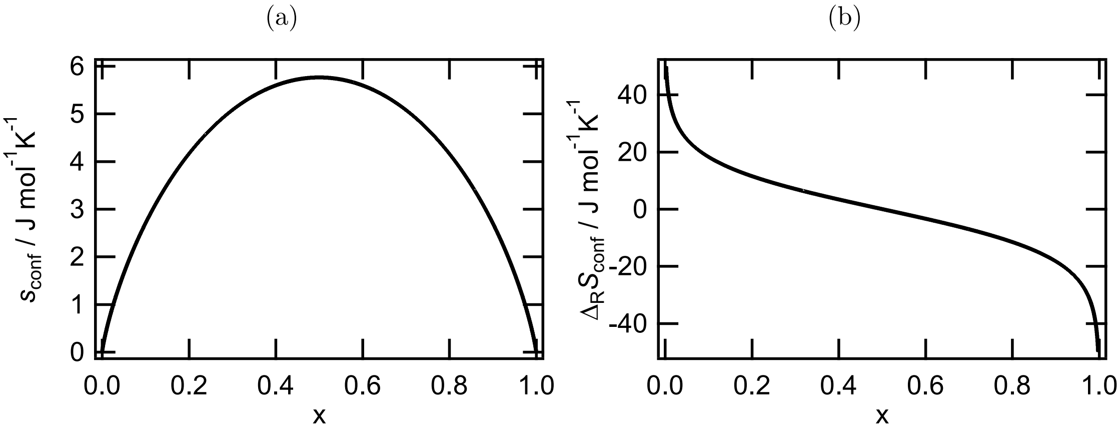

Figure 4.19: (a): Molar configurational entropy s_conf of an ideal solid solution (equation 4.1). (b): Partial molar configurational entropy $\Delta_\mathrm{R}S_\mathrm{conf}$ of an ideal solid solution (equation 4.2).

The configurational entropy depends on the number of possibilities to distribute the Na species and the vacancies in the available space.[63] In the simplest case of an ideal solid solution, i.e., a lattice with energetically equivalent sites, which is filled from $x = 0$ to $x = 1$, the molar configurational entropy s_{conf} is equivalent to the mixing entropy of an ideal solution and can be described with equation 4.1.[63]

$$s_{\mathrm{conf}} = -R\left(x\ln(x) + (1-x)\ln(1-x)\right) \tag{4.1}$$

From the slope of this function the partial molar configurational entropy, which is the measured quantity, can be derived.

$$\Delta_{\mathrm{R}}S_{\mathrm{conf}} = \frac{\partial s_{\mathrm{conf}}}{\partial x} = R\ln\left(\frac{1-x}{x}\right) \tag{4.2}$$

The courses of s_{conf} and $\Delta_{\mathrm{R}}S_{\mathrm{conf}}$ with increasing x are exemplarily shown in Figure 4.19. While s_{conf} is minimal for $x = 0$ and $x = 1$, $\Delta_{\mathrm{R}}S_{\mathrm{conf}}$ diverges toward positive and negative infinity, respectively.

For the herein measured variation of $\Delta_{\mathrm{R}}S_{\mathrm{cell}}$ with the SoC of a HC|Na metal cell, which comprises a minium and a maximum (see Figure 4.20 (a)), such a simple model of an ideal solid solution is insufficient. This can also be inferred from the change of the equilibrium potential of the HC electrode. With increasing sodium content the equilibrium potential decreases from around 1.2 V to almost 0 V. This pronounced potential change indicates that the assumption of energetically equivalent sites for storage of Na species does not hold. The different binding energies of the Na storage sites is one of the aspects, which was considered by Mercer *et al.* in their more sophisticated model of the configurational entropy of Na in HC.[61]

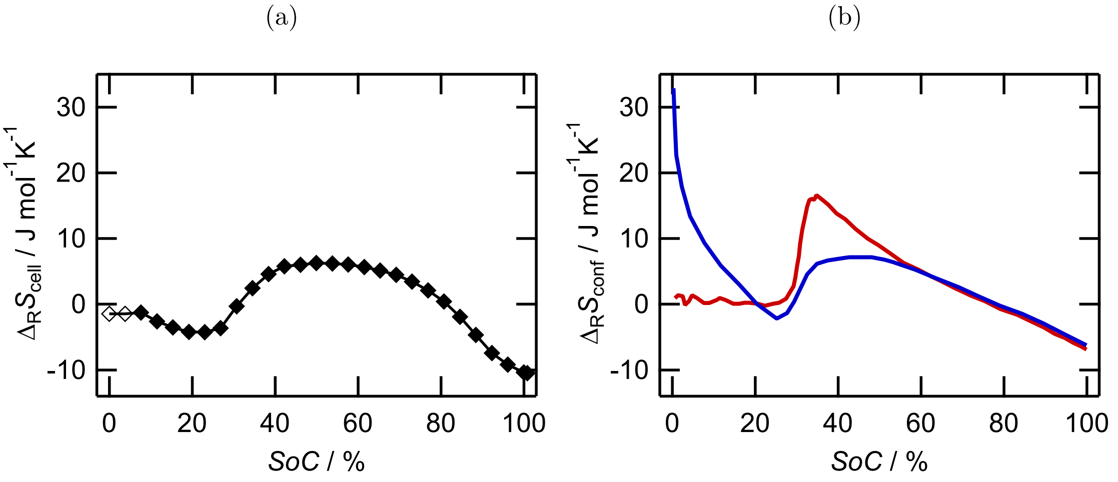

Figure 4.20: (a): Cell reaction entropy of a HC|Na metal coin cell with 1 M $NaPF_6$/ diglyme in the charging cycle. The data points of the cell reaction entropy at 0 % and 4 % SoC (shown with an empty diamond) could only be estimated, as described in chapter 4.3. (b): Partial molar configurational entropy simulated by Mercer *et al.* considering a distribution of binding energies of the interlayer sites (red), or a binding energy of the interlayer sites that varies with the SoC (blue).[61]

Mercer *et al.* represented the system by two energy levels, one representing sodium filling the interlayers and the other one sodium filling the pores. For the binding energy of the Na species in the interlayers they evaluated two different concepts. Motivated by the heterogeneity of HC, consisting of heteroatoms and defects, they first used a distribution of binding energies (between $-1.65\,\text{eV}$ and $0.08\,\text{eV}$) with increasingly more sites with high binding energy. By doing so the amount of energetically accessible sites at one specific SoC is low, which leads to a low configurational entropy at low SoCs (see the red line in Figure 4.20 (b)). This did not resemble their experimentally derived configurational entropy at low SoCs. Hence, they discarded this idea and used the same binding energy for all sites in the interlayers, but let the binding energy increase with increasing SoC. For the pore sites the binding energy was assumed to be independent of the SoC, but two additional terms were used to include interparticle interactions. Finally, instead of considering both energy levels completely separated, they allowed them to overlap, i.e., simultaneous interlayer and pore filling could take place. The resulting configurational entropy (shown with the blue line in Figure 4.20 (b)) was in agreement with their experimental results, i.e., high cell reaction entropies at low SoCs.

In the current study, the cell reaction entropy at SoCs below $10\,\%$ is significantly lower than the one obtained by Mercer *et al.* (see Figure 4.17). Such a low configurational entropy at low SoCs would be in line with the first model of Mercer *et al.* assuming that the binding energies of the sites accessible for Na species in the sloping region have a broad distribution and the amount of accessible sites is decreasing with increasing OCV (i.e., decreasing SoC). This becomes apparent when, for SoCs below $10\,\%$, the cell reaction entropy (Figure 4.20 (a)) is compared with the simulated partial molar configurational entropy that assumes a distribution of binding energies for the interlayer sites (red line in Figure 4.20 (b)). This is also in accordance with DFT calculations by Reddy *et al.*, who found variations of the potential of around $1\,\text{V}$ for vacancy containing graphitic layers.[50] When the energy difference between different binding sites is larger than the thermal fluctuations, only a small fraction of them is accessible, which ultimately leads to a low configurational entropy. Such a charging mechanism would be rather termed adsorption of Na^+ ions at defects and heteroatoms, than intercalation of Na^+ ions into the graphitic layers. For SoCs above $10\,\%$ the cell reaction entropy determined by Mercer *et al.* coincides with the one measured in this study (see Figure 4.17). Consequently, their model, in which a transition from simultaneous interlayer and pore filling to exclusive pore filling is assumed, might be adapted. Finally, a combination of the two models presented by Mercer *et al.* (i.e. in Figure 4.20 the red line at SoCs below $10\,\%$ and the blue line at SoCs above $10\,\%$) could explain the variation of the cell reaction entropy with the SoC found in this study. In conclusion, the results presented herein speak in favor of the adsorption-intercalation-pore filling model, i.e., Na^+ ion storage at defect sites with varying binding energy is followed by intercalation of Na^+ ions and ultimately pore filling takes place.

4.4.2 The Charging Process Changes with the State of Charge

With microcalorimetry a significantly reduced reaction entropy was found at SoCs below 20 %. In order to understand these differences of the reaction entropy at low and high SoC, more information about the process driven during the microcalorimetric pulse measurements is needed. In Figure 4.21 typical potential transients upon 10 ms sodiation pulses (−300 µA) of HC at low (ca. 3 %) and high SoC (ca. 75 %) are compared for (a) 1 M $NaClO_4$/PC and (b) 1 M $NaPF_6$/diglyme. Independent of the electrolyte solution and the SoC, the potential decreased stepwise when the current was switched on (t = 10 ms) and increased stepwise when the current was switched off (t = 20 ms). This abrupt change of the potential amounts to about 50 mV for all four transients and is attributed to the iR-drop in the electrolyte solution.

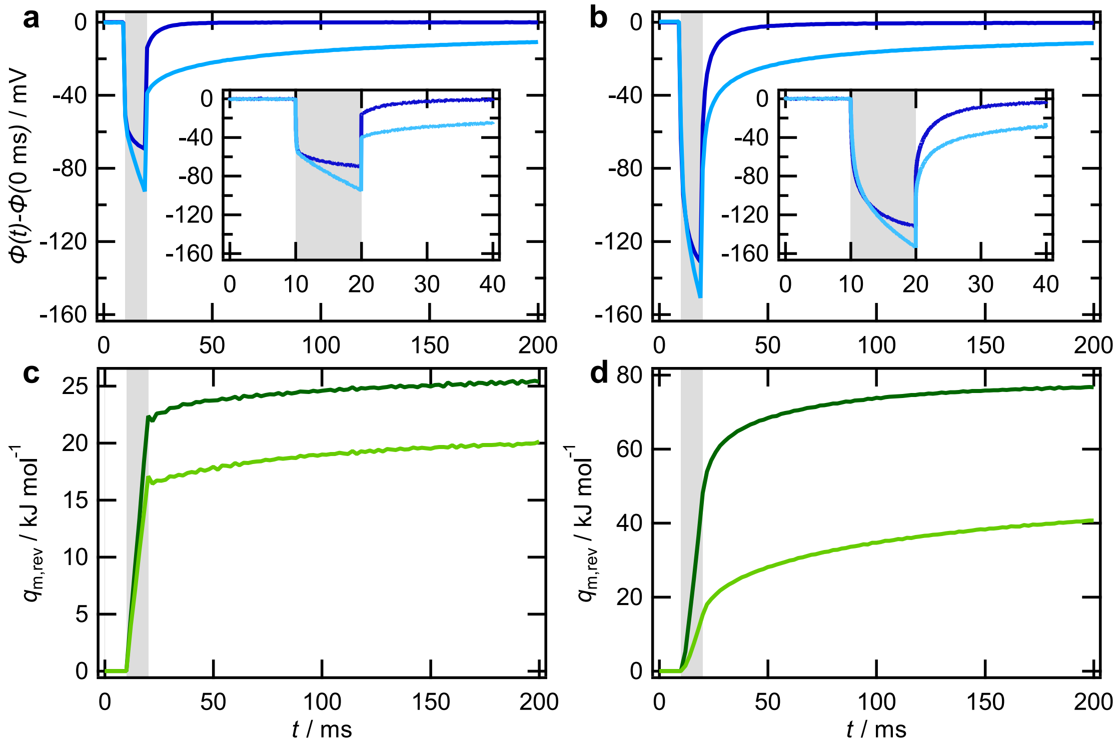

Figure 4.21: Potential transients, referenced to the initial potential, upon 10 ms current pulses (−300 µA, time interval marked in gray) at a high (dark blue) and a low SoC (light blue) of HC in (a) 1 M $NaClO_4$/PC and (b) 1 M $NaPF_6$/diglyme. The potential before for the pulse was, (a) 0.060 V (SoC 74 %) and 0.993 V (SoC 3.3 %), and (b) 0.059 V (SoC 76 %) and 1.020 V (SoC 3.6 %). The reversibly exchanged molar heat at the high (dark green) and the low SoC (light green) is shown in (c) and (d).

During current flow (from t = 10 ms to t = 20 ms) the potential decreases nearly linearly for HC at low SoC (3.3 %) in 1 M $NaClO_4$/PC (Figure 4.21 (a), light blue). On the contrary, at high SoC (74 %, Figure 4.21 (a), dark blue) the potential is only slowly decreasing during current flow. Immediately after the current pulse (at $t = 20\,\mathrm{ms}$, after the iR-drop), the remaining deviation of the potential from the initial potential (at $t = 0\,\mathrm{ms}$) is significantly larger at the low SoC ($-42\,\mathrm{mV}$) compared to the high SoC ($-18\,\mathrm{mV}$). Furthermore, at low SoC the potential relaxation at OC conditions is not completed at $t = 200\,\mathrm{ms}$, whereas at high SoC the initial potential is already reached at around $t = 50\,\mathrm{ms}$. It is expected that the potential relaxation at low SoC goes on far beyond 200 ms, since with the applied sodiation pulse at an SoC of 3.3 % a change of the equilibrium potential of less than 0.1 mV is expected. This was inferred from the slope of the equilibrium potential vs. specific capacity curve (shown for 1 M $NaClO_4$/PC in Figure 4.8), which was determined at OC conditions 40 min after changing the SoC. Similar behavior of the potential was observed in 1 M $NaPF_6$/diglyme (Figure 4.21 (b)), but for the same current amplitude the total overpotential was about 60 mV larger at each SoC compared to 1 M $NaClO_4$/PC.

The characteristics of the potential transients indicate that at low SoC the main process during the short sodiation pulses may be capacitive in nature and leads to significant charging of the interfacial capacitance. After the pulse, the interfacial capacitance is discharged on the minutes timescale and thereby the sodiation of HC may be driven further on without current flow in the external circuit. At high SoC Faradaic processes may dominate during the current pulse. Thus, the interface is less polarized and its equilibration after the pulse is already completed within around 30 ms. Simply put, at low SoC the major part of the current may lead to charging of the interfacial capacitance during the pulse, while at high SoC it may directly drive a Faradaic process. This could be caused by a higher charge transfer resistance at low SoC. Linsenmann *et al.* and Aniskevich *et al.* found with EIS that the charge transfer resistance is indeed up to ten times larger at low SoC compared to high SoC.[54, 55] Note, that part of the polarization could also be explained with concentration overpotential caused by enrichment or depletion of Na^+ ions in the pores filled with electrolyte solution or Na^+ ions in the HC grains.

In Figure 4.21 (c) the reversibly exchanged molar heat is shown in light green for the low SoC (3.3 %) and dark green for the high SoC (74 %) of HC in 1 M $NaClO_4$/PC. At $t = 200\,\mathrm{ms}$ less heat is exchanged at low SoC compared to the high SoC. This difference exists already at the end of the current pulse ($t = 20\,\mathrm{ms}$) and remains almost constant with increasing time, i.e., the delayed heat exchange is not influenced by the SoC. The smaller value for $q_{\mathrm{m,rev}}$ found at low SoC, i.e, the lower reaction entropy at low SoC, could be explained by partial desolvation of the Na^+ ions, since the largest contribution to the reaction entropy of the sodiation of HC is the desolvation of Na^+ ions. This partial desolvation has to take place already during the current pulse, since the major part of the heat is already exchanged up up to $t = 20\,\mathrm{ms}$.

In 1 M $NaPF_6$/diglyme at high SoC (3.6 %) more heat is exchanged compared to 1 M $NaClO_4$/PC (cf. Figure 4.21 (d)), which is due to the higher desolvation entropy in the ether-based electrolyte solution, as pointed out in chapter 4.4.1. The difference between the exchanged heat at high and low SoC is more pronounced in 1 M $NaPF_6$/diglyme, which is consistent with the hypothesis of partial desolvation of Na^+ ions. Nevertheless, it should be noted that only a doubling of this difference is expected considering the desolvation entropy for the respective electrolyte solutions and assuming that the degree of desolvation is the same at the probed SoC, but at $t = 200\,\text{ms}$ they differ by more than a factor of four. This might be caused by slow desolvation of Na^+ ions in the ether-based electrolyte solution, which was reported by Karcher *et al.* for the Na metal deposition.[29] In particular, they found that in 1 M $NaPF_6$/diglyme solvated Na^+ ions are incorporated during the electrochemical process in the SEI and are subsequently slowly desolvated without external or internal electrochemical current flow. Such a process would only alter the reversibly exchanged molar heat, but not the potential transient. This holds true for the comparison of the transients in the 1 M $NaClO_4$/PC and the 1 M $NaPF_6$/diglyme electrolyte solution in Figure 4.21. While the potential relaxes in about the same time after the current is stopped, significantly more heat is reversibly exchanged for $t > 20\,\text{ms}$ in the ether-based electrolyte solution.

Combining the information, which can be derived from the potential response and the reversibly exchanged molar heat, the following interim conclusion can be drawn. At low SoC (ca. 3 %) a capacitive process may dominate during the current pulse and is followed by a slow equilibration process. The reduced reaction entropy at this SoC could be explained with partial desolvation of the Na^+ ions. Simply put, at low SoC (ca. 3 %), the sodiation of HC, including the desolvation of Na^+ ions and the insertion of Na^+ ions into HC, may not be finished at $t = 200\,\text{ms}$. At high SoC (ca. 75 %), the potential relaxation after the current pulse is completed at $t = 200\,\text{ms}$. In addition, the reaction entropy is close to the one found for Na metal deposition, which indicates complete desolvation of the Na^+ ions. Thus, at high SoC (ca. 75 %) the sodiation of HC is presumably finished at $t = 200\,\text{ms}$.

So far, the mechanism was discussed only for the insertion of sodium into HC and only at two specific SoCs. For the desodiation of HC the same mechanism in the opposite direction should hold true, since with the short pulses the HC electrode stays close to equilibrium and mainly reversible processes are probed. This can be inferred from the almost quantitative reversal of the potential and heat transients, as, e.g., shown in Figure 4.5 for the high SoC. Still, the question remains how the mechanism of the sodiation of HC is gradually changing with the SoC. In Figure 4.22 (a) and (b) the reaction entropy is shown together with the equilibrium potential in the charging cycle for 1 M $NaClO_4$/PC and 1 M $NaPF_6$/diglyme, respectively. Additionally, the remaining deviation of the potential at $t = 400\,\text{ms}$ after 10 ms sodiation

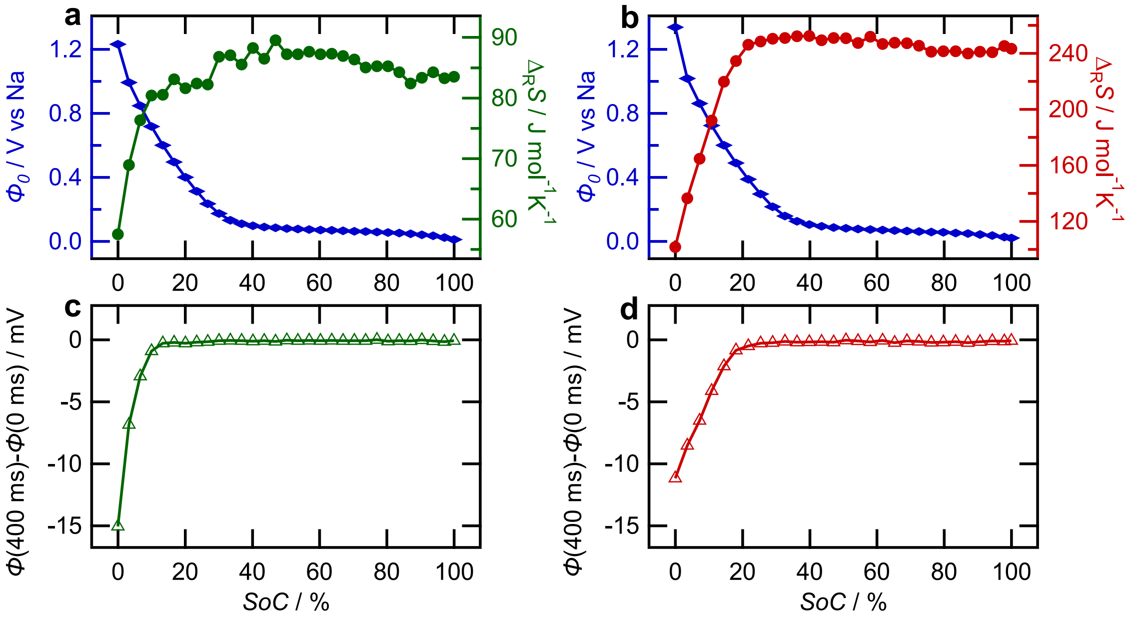

Figure 4.22: Further microcalorimetric results of the sodiation of HC dependent on the SoC compared between 1 M $NaClO_4$/PC (green) and 1 M $NaPF_6$/diglyme (red). (a), (b): Reaction entropy $\Delta_R S$ and equilibrium potential ϕ_0 in the charging cycle of HC. (c), (d): Difference between the potential at $t = 400$ ms after a 10 ms current pulse (−300 µA) and the potential at $t = 0$ ms before the pulse.

pulses (−300 µA) from the initial potential is shown dependent on the SoC for the corresponding electrolyte solution in Figure 4.22 (c) and (d). It can be clearly seen, that the reaction entropy (determined with the reversibly exchanged molar heat up to $t = 400$ ms) correlates with the remaining potential deviation. At SoCs below 20 % the current pulses lead to significant charging of the interface, which is associated with a reduced reaction entropy due to the incomplete desolvation. For all SoCs above 20 % the equilibration of the interface seems to be completed at $t = 400$ ms and hence the Na^+ ions are fully desolvated and the reaction entropy is close to the value found for Na metal deposition from the respective electrolyte solution. In addition, attention should be drawn to the different magnitude of the increase in reaction entropy from 0 % to 20 % in the different electrolyte solutions (see Figure 4.22 (a) and (b)). While, in 1 M $NaClO_4$/PC the reaction entropy is increasing by about 25 J mol^{-1} K^{-1}, the reaction entropy increases by about 145 J mol^{-1} K^{-1} in 1 M $NaPF_6$/diglyme. Since the desolvation entropy of Na^+ ions in 1 M $NaPF_6$/diglyme is considerably higher than in 1 M $NaClO_4$/PC, this corroborates the hypothesis that the reduced reaction entropy at SoCs below 20 % could be attributed to partial desolvation of the Na^+ ions.

To complete the picture, the cell reaction entropy determined with entropy profiling has to be taken into account (reproduced in Figure 4.23 (a)). As described in chapter 3.2 all processes, which are completed within 300 s, contribute to the cell reaction entropy determined from the temperature dependence of the equilibrium

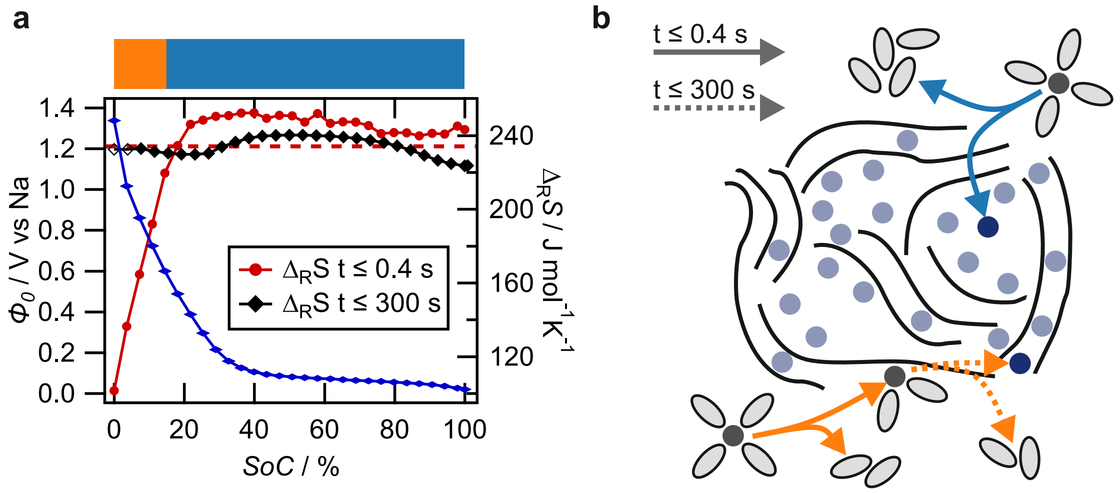

Figure 4.23: (a): Comparison of the reaction entropy and the equilibrium potential of HC with 1 M $NaPF_6$/diglyme in the charging cycle determined on different timescales, as shown in Figure 4.18. (b): Schematic representation of the sodiation mechanism of HC at low (orange) and high SoC (blue) (cf. the color bar on top of a).

cell voltage. On that timescale the desolvation of the Na^+ ions is completed at all SoCs, as discussed in chapter 4.4.1. This implies that the partial desolvation of the Na^+ ions at SoCs below 20 % found with microcalorimetry ($t \leq 0.4\,s$) is only an intermediate state and the desolvation is slowly completed within 300 s. The heat exchange due to this slow desolvation process is not captured with microcalorimetry, i.e., no significant changes of $q_{m,rev}$ are found for $t > 0.4\,s$, since the heat flux is probably below the sensitivity of the microcalorimetric method.

In conclusion, a mechanism for the sodiation of HC can be proposed (see Figure 4.23 (b)). At SoCs below 20 % the sodiation process is composed of a fast capacitive process on the milliseconds time scale, followed by slow equilibration through discharging of the interfacial capacitance. The fast capacitive process could be the adsorption of Na^+ ions at the HC surface, such as, e.g., observed in electrochemical double layer capacitors.[76] It is accompanied by partial desolvation of the Na^+ ions. In a following slow process, the desolvation of the Na^+ ions is completed. The rate of the slow equilibration process might be limited by the rate of the solid diffusion of Na species in the HC particle. At SoCs above 20 % the sodiation process involves a Faradaic process, which is accompanied by complete desolvation of the Na^+ ions - similar to the metal underpotential deposition mechanism for the filling of the pores of HC with Na proposed by Li *et al.*[77] This SoC-dependent mechanism is in agreement with the EIS findings at different SoCs by Schutjajew *et al.*[56] For the sodiation of HC they found processes with time constants of milliseconds up to twenty seconds. At low SoCs the impedance was clearly dominated by the slow process, whose contribution decreased significantly in the sloping region with increasing SoC, leading to an impedance dominated by the fast processes in the plateau region.

4.4.3 Influence of the Sodiation Kinetics on the Cell Voltage Response upon Temperature Steps

In the comparison of the cell reaction entropy of HC|Na metal cells found by different entropy profiling studies (Figure 4.17) significant deviations were found at SoCs below 10 % and it was briefly mentioned that OCV drift or sluggish kinetics might be the reason. Exactly at these SoCs, the characteristics of the cell voltage response caused by the temperature steps drastically changed (see Figure 4.14). In addition to the sharp negative voltage spike immediately after the temperature step, a maximum evolved. In the following a simple model will be introduced to simulate the time evolution of the electrode potentials of the HC and the Na metal electrode. The influence of the thermal response of the coin cell and the kinetics of the electrode reactions will be considered. From the simulated transients of the electrode potential, transients of the cell voltage are derived for different SoCs of the HC and are compared with the respective experimentally observed cell voltage transients.

The cell voltage E of a HC|Na metal cell is given by the difference between the potential of the HC electrode ϕ_{HC} and the potential of the Na metal electrode ϕ_{Na}. Therefore, its variation upon changing the temperature, starting from the initial temperature T_0, depends on the variation of the electrode potentials with their actual temperatures T_{HC} and T_{Na}.

$$\Delta E = \Delta\phi_{\mathrm{HC}}(T_{\mathrm{HC}} - T_0) - \Delta\phi_{\mathrm{Na}}(T_{\mathrm{Na}} - T_0) \tag{4.3}$$

With the brackets in equation 4.3 the functional dependence of the electrode potentials on the temperature is denoted. If an infinitely fast equilibration of the electrode potentials is assumed, the electrode potentials are equal to the respective equilibrium electrode potentials, whose temperature dependence is given in analogy to equation 2.2. Thus, the variation of the cell voltage, starting from the equilibrium cell voltage at the initial temperature T_0, depends on the electrode temperatures and their reaction entropies.

$$\begin{aligned}\Delta E &= \frac{\partial\phi_{0,\mathrm{HC}}}{\partial T}\cdot(T_{\mathrm{HC}} - T_0) - \frac{\partial\phi_{0,\mathrm{Na}}}{\partial T}\cdot(T_{\mathrm{Na}} - T_0)\\ &\approx \frac{1}{zF}\Delta_{\mathrm{R}}S_{\mathrm{HC}}\cdot(T_{\mathrm{HC}} - T_0) - \frac{1}{zF}\Delta_{\mathrm{R}}S_{\mathrm{Na}}\cdot(T_{\mathrm{Na}} - T_0)\end{aligned} \tag{4.4}$$

For simplicity, it was assumed that the reaction entropies of the electrode reactions are constant upon the small temperature changes. It should be noted that in the case of temperature gradients across the cell, the cell is not in an equilibrium state and irreversible thermodynamics has to be applied for a correct description of the cell voltage. In particular, ion and electron transport into and out of the the electrode-electrolyte interfaces at each electrode have to be included (see the derivation of the electrochemical Peltier heat in chapter 2.2.1). As a result, the temperature dependence of the electrode potential $\frac{\partial\phi}{\partial T}$ corresponds to the electrochemical Peltier heat Π, when the Soret diffusion is neglected (for a detailed description see Agar[15]). However, these corrections are neglected in the following, since the discussion is rather qualitative and the entropy of transport for 1 M $NaPF_6$/diglyme is small compared to the reaction entropy of the sodiation of HC in this electrolyte solution (cf. Table 4.1).

When the temperature of both electrodes is equal ($T_{\mathrm{HC}} = T_{\mathrm{Na}}$), equation 4.4 reduces to equation 2.2, since $\Delta_{\mathrm{R}}S_{\mathrm{HC}} - \Delta_{\mathrm{R}}S_{\mathrm{Na}} = \Delta_{\mathrm{R}}S_{\mathrm{cell}}$. As soon as the electrode temperatures differ, this temperature difference will be additionally reflected in the cell voltage variation. In the herein presented temperature step experiments such temperature gradients across the coin cell are expected, due to the asymmetric cell design. While the HC electrode is directly pressed against the cell housing, the Na metal electrode is contacted *via* a spring (see Figure 3.9) with a low thermal conductivity. Therefore, the HC electrode should follow the temperature change much faster than the Na metal electrode. To quantify these differences and their influence on the cell voltage, the thermal responses of the electrodes were simulated, which is explained in the following paragraph.

Coin Cell Temperature Simulation

The simulation of the heat transfer inside the coin cell is based on the procedure used by Bickel *et al.*[31] They employed that a thermal transport problem can be transposed into an electrical network problem. The temperature T is transposed into potential ϕ and heat q into charge Q. Equally, the temporal change of the temperature within a material with the heat conductivity λ_Q and the volumetric heat capacity c_{vol} in one dimension x,

$$\frac{\partial T}{\partial t} = \frac{\lambda_Q}{c_{\mathrm{vol}}}\frac{\partial T}{\partial x}, \tag{4.5}$$

is transposed into the change in potential within a RC transmission line with the resistance per unit length ρ' and the capacity per unit length C_V:

$$\frac{\partial\phi}{\partial t} = \frac{1}{\rho' C_V}\frac{\partial\phi}{\partial x}. \tag{4.6}$$

Hence 1 V corresponds to 1 K, ρ' to $\frac{1}{\lambda_Q}$ and C_V to $c_{\mathrm{vol}} = c_{\mathrm{m}}\rho$ with the specific heat capacity c_{m}.

Within this framework the heat transfer within the coin cell in one dimension was simulated with the equivalent electric circuit shown in Figure 4.24 in the program SPICE in the implementation by Linear Technologies (LTspice®). As already mentioned above, due to the asymmetric design of the coin cell, which is shown schematically in Figure 3.9, the heat transfer from the housing to the Na metal electrode is expected to be much slower than the heat transfer to the HC electrode. This was implemented in the simulation by assuming that the heat flux toward the Na metal electrode occurs purely through the electrolyte-soaked separator and the HC composite electrode, neglecting the heat transfer from the backside of the Na metal electrode. In the equivalent circuit this is reflected with only one controllable voltage source, with which the temperature change at the backside of the Cu current collector was simulated. This voltage source is connected to three *RC* transmission lines connected in series, which represent the Cu current collector with the HC composite, the separator soaked with the electrolyte solution and the stainless-steel spacer with the Na metal pressed on it.

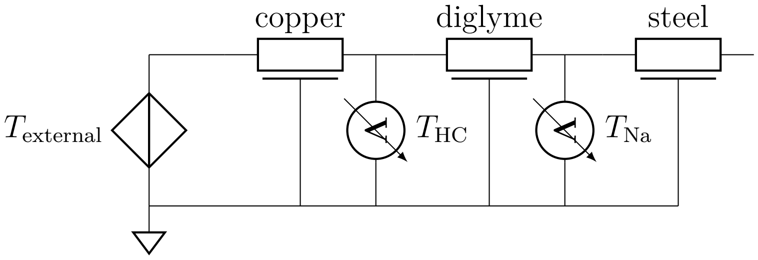

Figure 4.24: Equivalent electric circuit used for the coin cell temperature simulation.

Several assumptions were made to simplify the simulation. The HC composite on the 50 µm thick Cu current collector was neglected, so that the material parameters of pure Cu could be used. For the 420 µm thick separator layer the material parameters of pure diglyme were assumed, and the Na metal on the 1000 µm thick stainless-steel spacer was neglected. This led to the following layers: 50 µm Cu, 420 µm diglyme and 1000 µm stainless-steel. The respective material parameters used in the simulation are summarized in Table 4.2.

	Copper	Diglyme	SS (304)
$c_{\text{m}}/\text{J g}^{-1}\text{K}^{-1}$	0.385[78]	2.08[79]	0.38[80]
$\lambda_Q/\text{W m}^{-1}\text{K}^{-1}$	401[78]	0.14[81]	13.8[80]
$\rho/\text{g cm}^{-3}$	8.96[82]	0.94[83]	8.0[80]
$c_{\text{vol}}/\text{J K}^{-1}\text{m}^{-3}$	3.45×10^6	1.96×10^6	4.00×10^6
$C_V/\text{F m}^{-1}$	3.45×10^6	1.96×10^6	4.00×10^6
$\rho'/\Omega\,\text{m}^{-1}$	2.55×10^{-3}	7.1	6.2×10^{-2}

Table 4.2: Parameters used for the simulation of the electrode temperatures.

Finally, the heat transfer within the coin cell was simulated. An exponential decay from 298.15 K to 293.85 K with a time constant of 4.7 s, which was obtained from an exponential fit to the temperature experimentally measured at the backside of the Al cell holder, was used to trigger the heat transfer. The voltage at the output of the Cu *RC* transmission line was denoted as the temperature of the HC electrode and the voltage at the output of the diglyme RC transmission line as the temperature of the Na metal electrode (indicated in Figure 4.24).

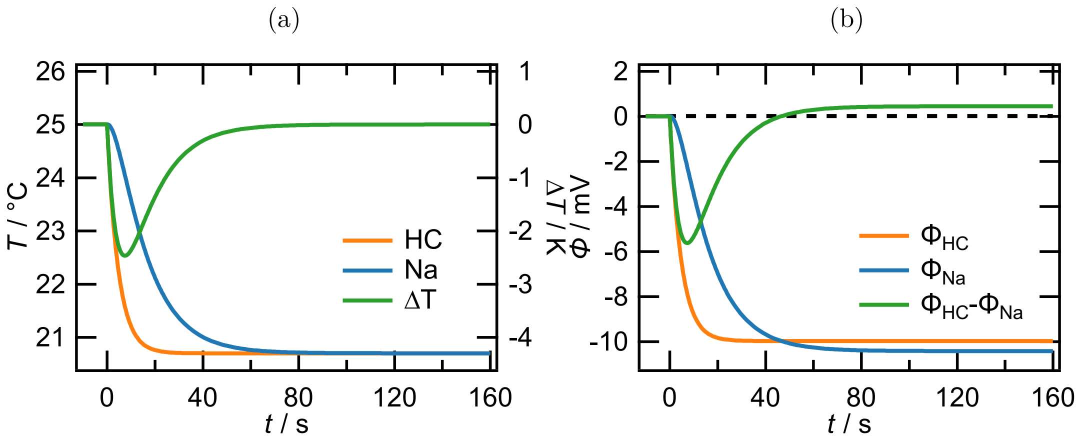

Figure 4.25: (a): Simulated temperature of the HC electrode (orange) and the Na metal electrode (blue) and their temperature difference (green) caused by an exponential decay of the temperature at the backside of the HC electrode. (b): Electrode potentials and the cell voltage (green) determined with the simulated electrode potentials and equation 4.4. For the reaction entropies of the electrode $\Delta_R S_{Na} = 234\,\mathrm{J\,mol^{-1}\,K^{-1}}$ and $\Delta_R S_{HC} = 224\,\mathrm{J\,mol^{-1}\,K^{-1}}$ were used.

The resulting temperature of both electrodes and the difference between them is shown in Figure 4.25 (a). It can be clearly seen, that significant differences between the temperatures of the electrodes arise. The temperature difference (green) has a minimum of $-2.5\,\mathrm{K}$ at $t = 7\,\mathrm{s}$ before for $t > 60\,\mathrm{s}$ it approaches zero, that is, both electrodes reach the same temperature. The variation of the temperatures of the electrodes was subsequently used to calculate the electrode potentials and the cell voltage employing equation 4.4, i.e., assuming infinitely fast local equilibration of the electrode potentials. For the reaction entropy of Na metal deposition $\Delta_R S_{Na} = 234\,\mathrm{J\,mol^{-1}\,K^{-1}}$, which was determined by Karcher *et al.*, was used.[29]. For the reaction entropy of the sodiation of HC $\Delta_R S_{HC} = 224\,\mathrm{J\,mol^{-1}\,K^{-1}}$ was used, resulting in a difference of $\Delta_R S_{cell} = -10\,\mathrm{J\,mol^{-1}\,K^{-1}}$, as it was found for a high SoC of the HC electrode (see e.g. Figure 4.16). The resulting electrode potentials and the difference between them, that is the cell voltage, is shown in Figure 4.25. As expected, the electrode potentials directly follow the electrode temperatures and the cell voltage follows the temperature difference. The cell voltage exhibits a pronounced minimum lower than $-5\,\mathrm{mV}$ for short times, which can be directly ascribed to the differing time evolution of both electrode temperatures and is very similar to the minimum observed in the temperature step experiment at SoCs above 8 % (cf. Figure 4.14 (a), (b) and (c)). For $t > 60\,\mathrm{s}$ the cell voltage reaches a stable value of around $0.4\,\mathrm{mV}$, which is the result of the difference of the reaction entropies at both electrodes, i.e., it reflects $\Delta_R S_{cell}$. It is noteworthy that the high reaction entropies of the single electrodes, which are a result of the solvation/desolvation of the Na^+

ions, lead to a strong variation of the electrode potentials of more than 10 mV, while the variation of the cell voltage amounts only a to a few tenth of a mV. In conclusion, the sharp negative voltage spike for $t < 10\,\mathrm{s}$ is a result of the temperature differences between the electrodes, which occur after switching the temperature, and the high temperature sensitivity of the electrode potentials. For $t > 60\,\mathrm{s}$ these temperature gradients vanish and the cell voltage variation is solely determined by the cell reaction entropy $\Delta_\mathrm{R}S_\mathrm{cell}$.

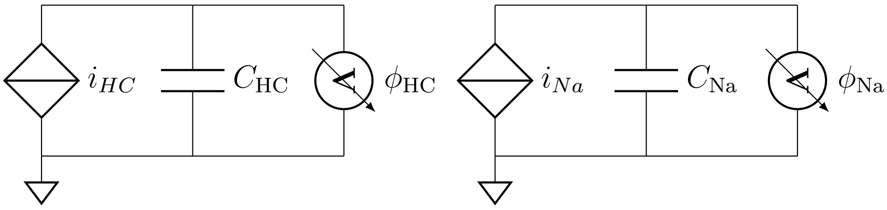

Figure 4.26: Equivalent electric circuit used for the electrode potential simulation. The current was calculated with equation 4.7 and the voltage across the capacitor was denoted as electrode potential of the respective electrode.

Introducing the Kinetics of the Electrode Polarization

At a SoC of 8 % the negative voltage spike in the cell voltage response upon the temperature step was followed by a maximum, which at a SoC of 0 % even dominated the cell voltage response (cf. Figure 4.14 (c)). So far, this could not be explained with the simulation, in which it was assumed that the electrode potentials can instantaneously follow the temperature changes. At such low SoCs sluggish kinetics of the sodiation/desodiation of HC were reported. In particular, an increase of the charge-transfer resistance with decreasing SoC was found with EIS.[54, 55] Consequently, it is supposed that kinetic limitations of the sodiation/desodiation of HC might cause the maximum in the cell voltage response. In order to evaluate this hypothesis, the kinetics of the processes at the HC and the Na metal electrode are included in the simulation. As described above the electrode potentials show strong variation due to the variation of the electrode temperatures. To readjust thermodynamic equilibrium at the electrodes, their double layers have to be strongly polarized, which is achieved by the insertion or extraction of a small amount of Na^+ ions from the electrode with a finite rate.

To include double layer charging in the simulation of the electrode potentials, Butler-Volmer-type kinetics were assumed for the electrode processes (exemplarily presented here for the sodiation/desodiation of the HC electrode). For the herein discussed experiment, the overpotential, which is needed to drive the reaction, is not an externally applied potential, but is the difference between the temperature dependent equilibrium electrode potential $\phi_{0,\mathrm{HC}}(T_\mathrm{HC})$ and the actual electrode potential

ϕ_{HC}. The current density referring to the active electrode area is given by:[84]

$$j = Fc_0k_0\left[\exp\left(\frac{\alpha F\left(\phi_{\mathrm{HC}} - \phi_{0,\mathrm{HC}}(T_{\mathrm{HC}})\right)}{RT}\right) - \exp\left(-\frac{(1-\alpha)F\left(\phi_{\mathrm{HC}} - \phi_{0,\mathrm{HC}}(T_{\mathrm{HC}})\right)}{RT}\right)\right] \tag{4.7}$$

with the molar gas constant R, the transfer coefficient $\alpha = 0.5$, the standard concentration $c_0 = 1\,\mathrm{mol\,l^{-1}}$ and the standard rate constant $k_0 = A\exp\left(-\frac{\Delta H^{\ddagger}}{RT}\right)$. $\Delta H^{\ddagger}$ is the activation energy and A is the pre-exponential factor, which is assumed to be temperature-independent.

In order to simulate the potential transients of the HC and the Na metal electrode, the respective temperature profiles shown in Figure 4.25 (a) were used to calculate the equilibrium electrode potential according to equation 4.4 and ultimately equation 4.7 was used to simulate the current to charge the double layer of the electrode. The equivalent electric circuits used for this simulation are shown in Figure 4.26. For the double layers a capacitance of $100\,\mathrm{\mu F\,cm^{-2}}$ was estimated and the voltage across the capacitors were used as the actual electrode potentials. Due to the rather low conversions expected for double layer charging, any concentration changes are neglected.

The relevant parameters for an Arrhenius-type description of the kinetics of the electrode reactions are the activation energy $\Delta H^{\ddagger}$ and the pre-exponential factor A. With temperature-dependent EIS Lv *et al.* determined $\Delta H^{\ddagger}$ for a fully sodiated HC electrode in 1 M $\mathrm{NaPF_6}$/diglyme electrolyte solution ($64.0\,\mathrm{kJ\,mol^{-1}}$),[60] and Niu *et al.* for a Na metal electrode in the 0.5 M $\mathrm{NaPF_6}$/diglyme electrolyte solution ($59.0\,\mathrm{kJ\,mol^{-1}}$).[85] The pre-exponential factor was estimated with the reported charge-transfer resistance R_{ct} at a certain temperature and $\Delta H^{\ddagger}$ as follows. For small overpotentials, the Butler-Volmer equation can be linearized and the exchange current density is given by $j_0 = \frac{RT}{FR_{\mathrm{ct}}}$.[84] Since $j_0 = Fk_0c_0$, the pre-exponential factor can be obtained by $A = \frac{j_0}{Fc_0}\exp\left(\frac{\Delta H^{\ddagger}}{RT}\right)$. With the values reported for R_{ct} by Lv *et al.* for the fully sodiated HC electrode,[60], and by Niu *et al.* for the Na metal electrode,[85] pre-exponential factors of $711\,\mathrm{m\,s^{-1}}$ and $79\,000\,\mathrm{m\,s^{-1}}$ were determined for the HC and the Na metal electrode, respectively.

With these kinetic parameters the transients of the electrode potentials and of the cell voltage upon a temperature step were simulated and are shown in Figure 4.27 (a) (referred to as high SoC). The temporal progression of the electrode potentials and the cell voltage equal the transients in Figure 4.25, where double layer charging was neglected. This implies that the sodium deposition reaction as well as the sodiation of HC at a high SoC are fast enough so that the electrode potentials can immediately follow the temperature variations of the electrodes. The simulated transient of the cell voltage is similar to the ones experimentally observed for SoCs between

30 % and 100 % (see, e.g., Figure 4.27 (b)). However, the depth of the cell voltage minimum in the simulation is more than five times larger than the experimentally observed one at a SoC of 99 % (compare Figure 4.27 (a) and (b)). There are two explanations to this. Either the heat transfer to the Na metal electrode is underestimated in the simulation, since heat transfer *via* the spring from the backside of the Na metal electrode was neglected. A faster heat transfer to the Na metal electrode would lead to a faster decrease of the potential of the Na metal electrode and ultimately to a smaller cell voltage minimum. Or, the reaction rate of the sodiation of HC was overestimated, i.e., the activation energy used in the simulation was too low. Analogously, a slower equilibration of the HC electrode potential would lead to a smaller minimum in the cell voltage.

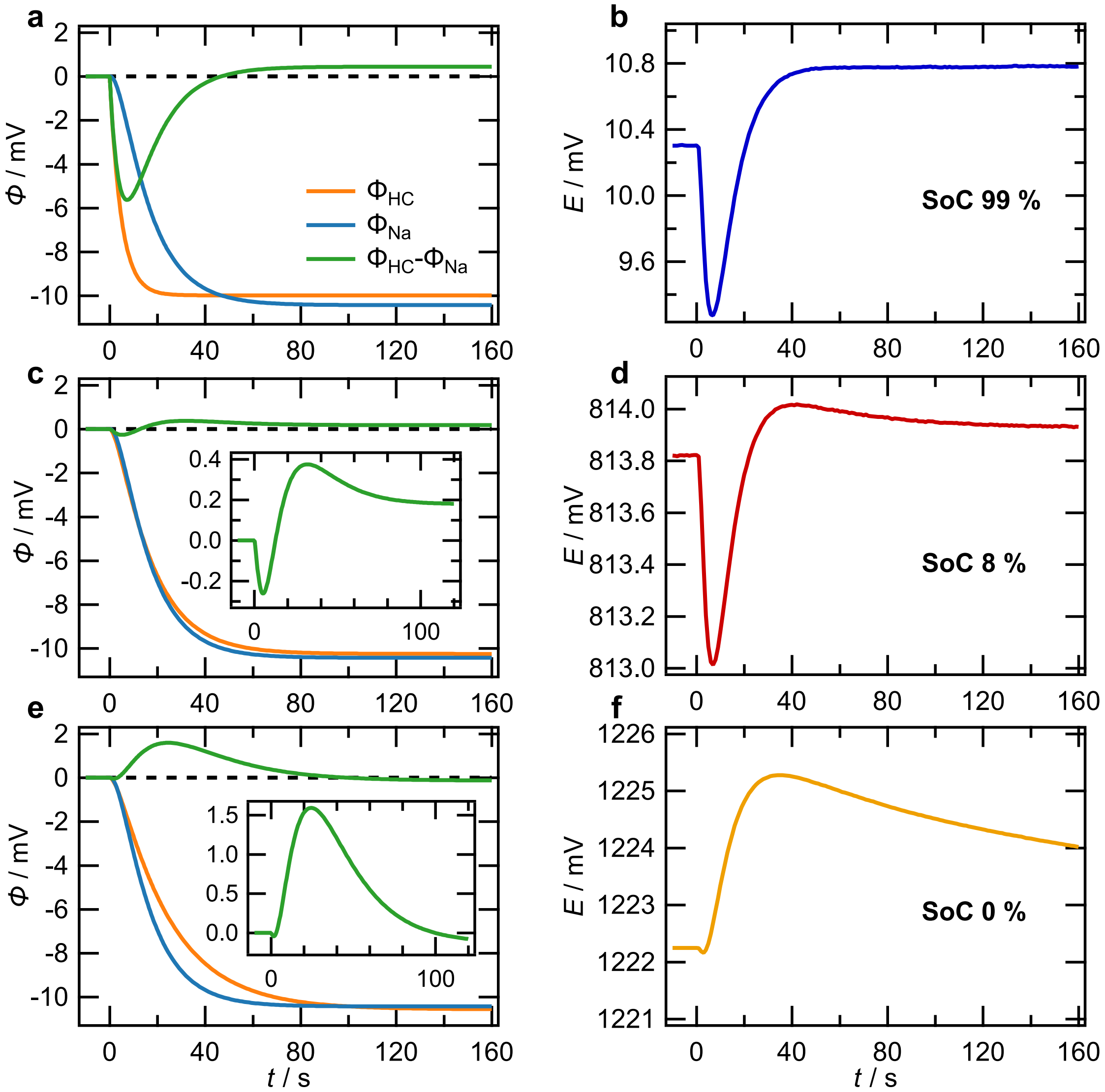

Figure 4.27: (a), (c), (e): Simulated electrode potentials of the HC (orange) and the Na metal electrode (blue) and the simulated cell voltage (green) at a (a) high, (b) medium and (c) low SoC. The used parameters are summarized in Table 4.3. (b), (d), (f): Experimentally measured cell voltage transients corresponding to the three SoCs.

At lower SoCs, where an influence of the slow sodiation kinetics is expected, no kinetic parameters were available for the same electrolyte solution. Thus, the activation barrier in the simulation was adjusted in order to achieve qualitative agreement between the simulation and the experimentally measured cell voltage responses at a SoC of 8 % (referred to as medium SoC in the simulation) and a SoC of 0 % (referred to as low SoC). Finally, activation energies of $\Delta H^{\ddagger} = 76.5\,\mathrm{kJ\,mol^{-1}}$ and $77.5\,\mathrm{kJ\,mol^{-1}}$ were used to simulate the medium and the low SoC, respectively. This is consistent with temperature-dependent EIS measurements by Aniskevich *et al.*, who found an increasing activation barrier of the sodiation/desodiation process at the HC electrode in a PC-based electrolyte solution with decreasing SoC.[55] All kinetic and thermodynamic input parameters for the simulation are summarized in Table 4.3.

	$\Delta_{\mathrm{R}}S/\mathrm{J\,mol^{-1}\,K^{-1}}$	$\Delta H^{\ddagger}/\mathrm{kJ\,mol^{-1}}$	$A/\mathrm{m\,s^{-1}}$
Na metal	234	59.0[85]	79000[85]
HC, high SoC	224	64.0[60]	711[60]
HC, medium SoC	230	76.5	711[60]
HC, low SoC	237	77.5	711[60]

Table 4.3: Thermodynamic and kinetic parameters used for the simulation of the electrode potentials.

In Figure 4.27 (c) and (e) the simulated transients of the electrode potentials and the cell voltages are shown for medium and low SoC. While the potential transient of the Na metal electrode persists, that of the HC electrode is considerably delayed with respect to its temperature transient. This is rooted in the slow sodiation kinetics at lower SoCs leading to slow double layer charging. The delay of the HC electrode potential is directly influencing the cell voltage transient. At medium SoC (Figure 4.27 (c)) the amplitude of the sharp negative voltage spike, which was attributed to the temperature gradient within the coin cell, is significantly reduced and a maximum in the cell voltage evolved at around 30 s and decays within about 100 s. This is in qualitative agreement with the cell voltage transient experimentally observed at an SoC of 8 % (Figure 4.27 (d)). At low SoC (Figure 4.27 (e)) the double layer charging at the HC electrode is even more slowed down, resulting in a cell voltage transient, which hardly shows a sharp minimum but is rather dominated by the large maximum extending over more than 100 s. This resembles the cell voltage response found in the experiment at 0 % SoC (Figure 4.27 (f)).

The simulation revealed two key aspects of the temperature step experiments with the HC|Na metal cells. Firstly, due the high reaction entropies of the processes at the single electrodes, the electrode potentials are highly temperature-sensitive. Thus, the sharp cell voltage spike for $t < 10\,\mathrm{s}$ is a result of temperature gradients across the coin cell caused by the asymmetric design of the employed coin cell. Secondly, the maximum in the cell voltage, which evolves at SoCs $\leq 8\,\%$, is a result of the sluggish kinetics of the sodiation of HC at these SoCs leading to a slow equilibration of the HC electrode potential. In the herein presented temperature step experiments this maximum impeded a reasonable determination of the cell reaction entropy at SoCs below 8 % as already mentioned in chapter 4.3. The sluggish sodiation kinetics most likely also influence the results of the entropy profiling studies shown in Figure 4.17 and might be one explanation for the deviations between the different studies at SoCs below 10 %.

4.4.4 Conclusions

The reaction entropy of the sodiation of HC is dominated by the desolvation of the Na^+ ions concomitant with the insertion into the HC. Since the desolvation entropy is highly dependent on the electrolyte solution (especially on the employed solvent), the reaction entropy of the sodiation of HC is significantly influenced by the electrolyte solution. In the microcalorimetric pulse experiments as well as in the cell voltage responses caused by temperature steps, it was observed that the kinetics of the charging process vary with the SoC. At SoCs below 20 % the sodiation of HC and consequently the desolvation of the Na^+ ions was found to be significantly slowed down. At these SoCs, the process driven by the 10 ms current pulses used for the electrochemical microcalorimetry was mainly capacitive in nature and the reduced reaction entropy indicated only partial desolvation of the Na^+ ions within 400 ms. However, with the cell reaction entropy determined with entropy profiling it could be shown that the desolvation of the Na^+ ions was completed within 300 s also at SoCs below 20 %. Consequently, from the herein presented data a permanent co-intercalation of Na^+ ions and solvent molecules into HC is not expected. At SoCs above 20 % the sodiation of HC exhibited faster kinetics, leading to less charging of the interface during the 10 ms current pulses and a complete desolvation of the Na^+ ions within 400 ms. In addition to the contribution of the desolvation of the Na^+ ions, the entropy of the Na species in HC contributes to the sodiation entropy of HC. The variation of the entropy of the Na species in HC with the SoC was ascribed to contributions of the configurational entropy and speaks in favor of the adsorption-intercalation-pore filling model.

4.5 XPS Investigations of the Solid Electrolyte Interphase on Hard Carbon

It has already been noted in chapter 4.1 that the components of the SEI in SIBs are in general more prone to dissolution than those of the SEI in LIBs.[86] For instance, the solubility of NaF in PC is more than 50 times higher than for LiF in PC (the same trend is found for the respective alkali metal carbonates).[87] By investigating changes of the SEI thickness with hard X-ray photoelectron spectroscopy, Mogensen *et al.* found that the dissolution of the SEI is one of the major reasons for self-discharging of HC electrodes.[68] If parts of the SEI are continuously dissolved, the SEI has to be reformed during cycling by decomposition of the electrolyte solution. Consequently, it is expected that the state of the SEI is not only changing during the first cycle, but also varies with the SoC of the HC electrode during consecutive cycling.

The components of the SEI can, e.g., be probed with XPS. The composition of the SEI is highly dependent on the salt, the solvent(s) and the additive(s) used in the electrolyte solution.[41, 66, 88] Eshetu *et al.* found, e.g., that the anion of the salt determines the overall nature of the SEI on the HC electrode in SIBs. By using $NaPF_6$ more organic content was found in the SEI compared to, e.g., $NaClO_4$.[66] In most XPS studies the HC electrodes are investigated after different numbers of charging/discharging cycles, but at an identical SoC.[34, 67, 89] However, Dahbi *et al.* measured XP spectra of HC electrodes, which were cycled to specific cutoff voltages in the first charging cycle.[90] Already at 1.2 V vs. Na/Na^+ the intensity of the sp^2 C peak, which originates from the graphitic layers of the HC, was decreasing. They concluded that a surface layer was formed on the HC electrode. Zhu *et al.* and Alvin *et al.* investigated the changes of the Na 1s peak at different cutoff voltages to understand the sodiation mechanism of HC.[91, 92]

Herein, the influence of the SoC of the HC electrode on the SEI is studied by XPS. For this purpose, the HC electrodes were cycled five times before being charged to a specific SoC, which is described in chapter 4.5.1. In chapter 4.5.2, the XP spectra of a fully sodiated, a partially sodiated and a desodiated HC electrode are compared with those of a HC electrode, which was assembled in a pouch cell without cycling, and a pristine HC electrode. The same set of samples was investigated with a 1 M $NaPF_6$/diglyme electrolyte solution, hereafter referred to as Diglyme samples, and a 1 M $NaPF_6$/EC,PC+FEC electrolyte solution, hereafter referred to as Carbonate samples.

4.5.1 Electrochemical Cycling

With each electrolyte solution four HC|Na metal cells were build. One cell was only assembled, but not cycled. The other three cells were cycled five times with a

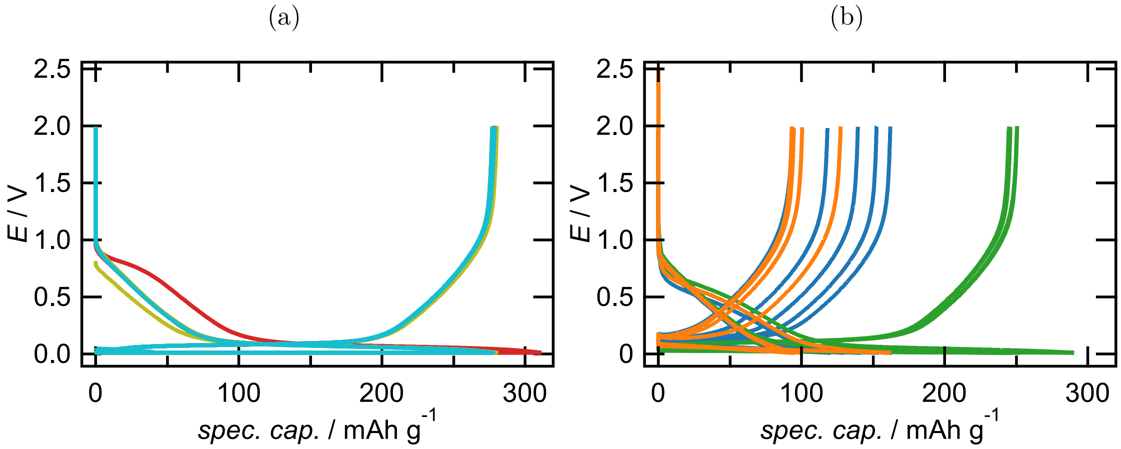

Figure 4.28: Charging and discharging curves of three HC|Na metal pouch cells with (a) Diglyme and (b) Carbonate electrolyte solution. For each cell the first five cycles are shown. The charging rate was 0.1 C. The lower voltage limit was 0.01 V and the upper voltage limit was 2.00 V.

charging rate of 0.1 C. The corresponding charging and discharging curves are shown in Figure 4.28 for the (a) Diglyme cells and (b) the Carbonate cells. The Diglyme cells showed the typical charging behavior of HC consisting of a sloping and a plateau region. Specific capacities of 270 - 280 mAh g^{-1} were obtained as expected.[39] Only in the first charging cycle differences among the three samples, most likely due to SEI formation, were observed. In contrast to that, the charging/discharging curves of the Carbonate cells significantly differed from each other in all cycles. This might be rooted in the bad uptake of the Carbonate electrolyte solution by the separator. The first attempt with Celgard separators, which were used for the Diglyme cells, failed, since the electrolyte solution was not sucked up by the separator and thus no cycling was possible. Glass fiber separators were avoided, because they can stick to the electrode surface and alter the XPS results. Finally, Solupor separators were used as a compromise for the Carbonate cells. The electrolyte solution uptake by the Solupor separator was better, but not as good as for the Diglyme electrolyte solution. Only one Carbonate cell reached the expected capacity (see Figure 4.28 (b), green) and for the other Carbonate cells values below 150 mAh g^{-1} were obtained. Due to the bad uptake of the electrolyte solution by the separator, the cells probably had high internal resistances, so that the lower voltage limit of 0.01 V was reached before the HC electrodes were fully sodiated.

After these five formation cycles, each cell was charged to a different SoC by stopping at different voltage limits. Just before the pouch cells were disassembled in order to measure the XP spectra of the HC electrodes, their OCVs were measured. In Table 4.4 an overview of all samples, their preparation and OCVs is given.

Identifier	Condition	Cycling	OCV
Diglyme A	soaked with electrolyte solution	not cycled	-
Diglyme B	desodiated HC	24 h rest, 5 x 0.1 C, 1 x 0.2 C	0.964 V
Diglyme C	partially sodiated HC	24 h rest, 5 x 0.1 C, 1 x 0.2 C, 0.1 C until 0.07 V	0.073 V
Diglyme D	fully sodiated HC	24 h rest, 5 x 0.1 C, 1 x 0.2 C, 0.1 C until 0.01 V	0.015 V
Carbonate A	soaked with electrolyte solution	not cycled	2.325 V
Carbonate B	desodiated HC	72 h rest, 5 x 0.1 C, 1 x 0.1 C	0.999 V
Carbonate C	partially sodiated HC	24 h rest, 5 x 0.1 C, 1 x 0.1 C, 0.1 C until 0.07 V	0.107 V
Carbonate D	fully sodiated HC	72 h rest, 5 x 0.1 C, 1 x 0.1 C, 0.1 C until 0.01 V	0.081 V

Table 4.4: Overview of the different samples and their electrochemical preparation for the XPS measurements. The OCV was measured right before the cells were disassembled.

4.5.2 X-ray Photoelectron Spectra

In Figure 4.29 survey XP spectra of selected samples are shown. The main contributions in all spectra are attributed to carbon, oxygen and sodium. Already on the pristine HC electrode, sodium was found, since sodium carboxymethyl cellulose was used as binder in the composite electrodes. The oxygen contribution on the pristine sample is also a result of the binder, as well as O residues in the HC active material. In the spectra of the HC electrodes from the cells, which were not cycled (Diglyme A, Carbonate A), peaks of fluorine and phosphorus were found, which could stem from the used salt $NaPF_6$ and in the case of the Carbonate electrolyte solution the additive FEC. The same elements were found on the cycled and fully sodiated HC electrodes (Diglyme D, Carbonate D), but the intensity ratio between the Na 1s and the C 1s peak differs. While for the pristine HC electrode the intensity of the C 1s peak is higher than that of the Na 1s peak, this is inverted for the cycled HC electrodes. As expected, the amount of sodium present on the fully sodiated HC samples is significantly higher compared to the pristine sample.

The raw XP spectra of the C 1s region of the HC electrodes are compared in Figure 4.30 for the (a) Diglyme and the (b) Carbonate cells. The vertical dashed lines indicate the position of the C$-$H/C$-$C peak. For the pristine electrode this line is located at 285 eV, but for all other samples it is shifted toward higher binding energies. This can already be seen for the non-cycled electrodes (Diglyme A and Carbonate A). The shift is enhanced when the HC electrodes were cycled and increases with increasing SoC of the HC electrode. Actually, the complete spectra and

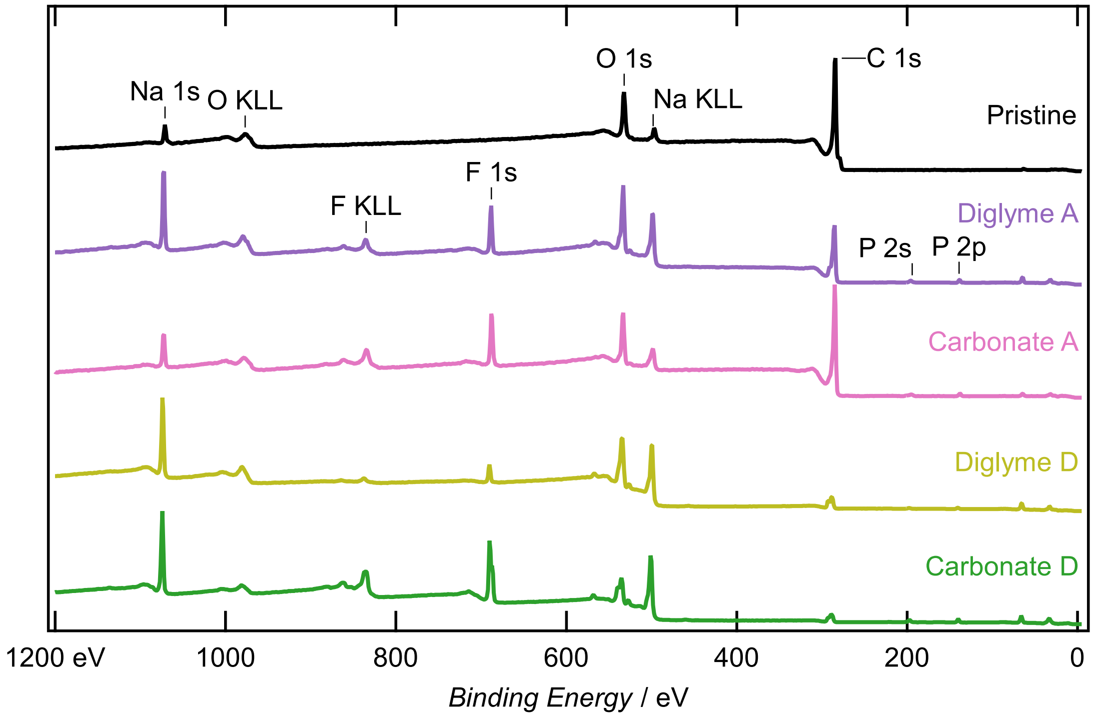

Figure 4.29: Survey XP spectra of the pristine thick HC electrode (46 µm), the thick HC electrodes soaked with electrolyte solution (Diglyme A, Carbonate A) and the fully sodiated, thick HC electrodes (Diglyme D, Carbonate D).

not only the C–H/C–C peaks are shifted. The shift might be explained with charge accumulation on the surface of the HC electrodes during the XPS measurements, which can lead to a positive shift of the binding energy. Such a process might take place, since the HC electrodes are covered with an electronically insulating SEI. The positive charge, which is caused by the emission of photoelectrons from the sample during the XPS measurements, can not be compensated. Since this effect can already be seen for the HC electrodes, which were not cycled, it can be assumed that some kind of surface layer is formed on the HC electrode after being assembled in a HC|Na metal pouch cell. The differently pronounced shift of the HC electrodes, which were charged to a specific SoC, indicates that the surface layer, i.e., the SEI, is still changing with the SoC in the sixth cycle. With increasing SoC the SEI could become less electronically conductive either due to changes in its composition or due to an increasing thickness.

Information about the composition can be obtained by curve fitting of the spectra. The results for the C 1s spectra are shown in Figure 4.31 and the binding energies and full widths at half maximum (FWHMs) of the individual peaks are summarized in Table C.1 and Table C.2 in the appendix for the Diglyme and the Carbonate samples, respectively. All spectra are referenced in binding energy to the respective C–H/C–C peak (yellow) at 285 eV. The C 1s spectrum of the pristine HC electrode has two main contributions. One can be attributed to sp^2 carbon (blue)

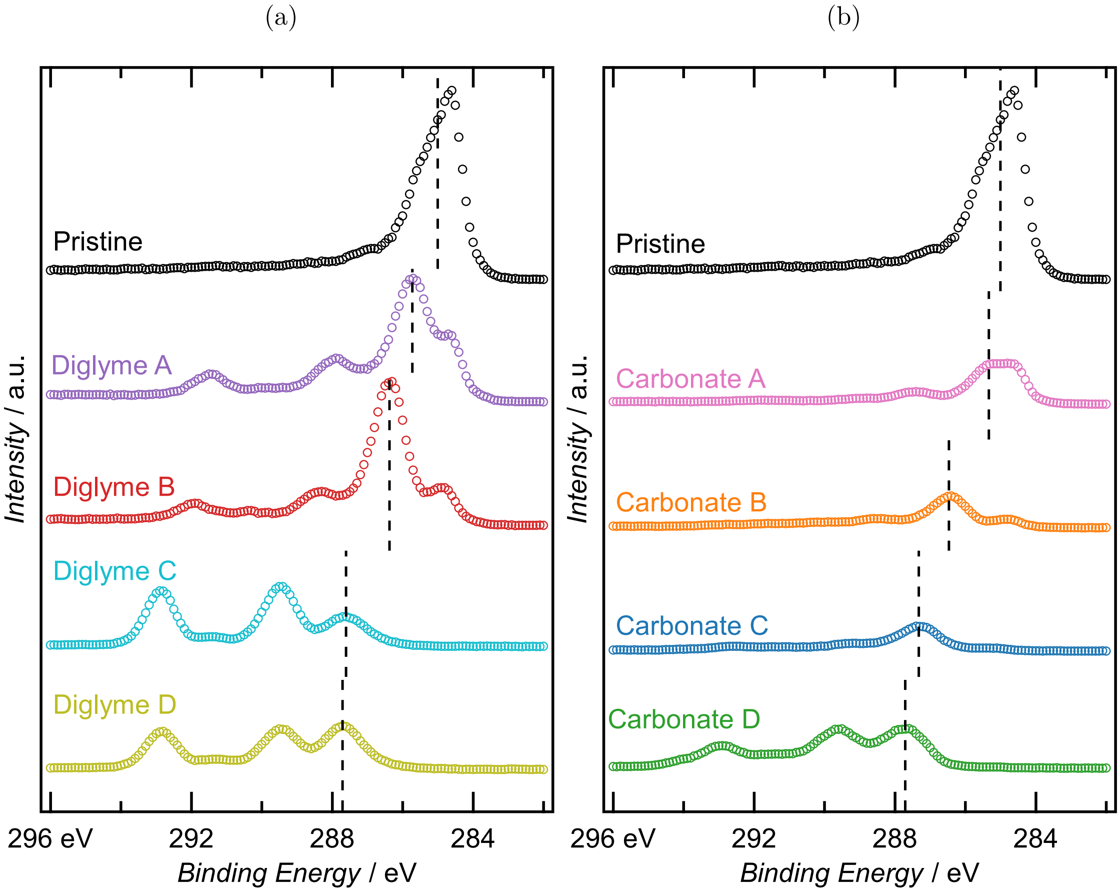

Figure 4.30: Raw XP spectra of the C 1s region of the (a) Diglyme and (b) Carbonate samples. The samples were grounded and no charge compensation was used. The vertical dashed lines indicate the position of the C−H/C−C peak.

stemming from the graphitic domains of the HC. The other one can be attributed to C−H/C−C species (yellow) of the HC electrode or adventitious carbon. In the spectra of the HC electrodes of the cells, which were not cycled (Diglyme A, Carbonate A), the intensity of the sp^2 C peak is reduced. In addition, contributions, such as from C−O, C=O and CO_3, arise. This corroborates the hypothesis formulated above, that a surface layer is formed on the HC electrodes already without cycling. For the cycled electrodes, the intensity of the sp^2 C peak is continuously decreasing with increasing SoC. For the cycled Diglyme samples the contributions of C−O and CO_3 increase significantly. For the cycled Carbonate samples an additional peak occurs at a binding energy of about 290.5 eV, which might be assigned to an FEC decomposition product.[93] In general, similar carbon species were found with XPS on HC electrodes in other studies after cycling in diglyme electrolyte solution,[34] and carbonate electrolyte solutions.[41, 88, 89, 94] It should be noted that the Na metal used as CE in the pouch cells can influence the SEI on the HC electrodes, since an SEI is also formed on the Na metal electrode and some of its compounds might diffuse through the separator and deposit on the HC electrode.[95] Additionally, the time interval between the end of charging and the disassembly of the cells

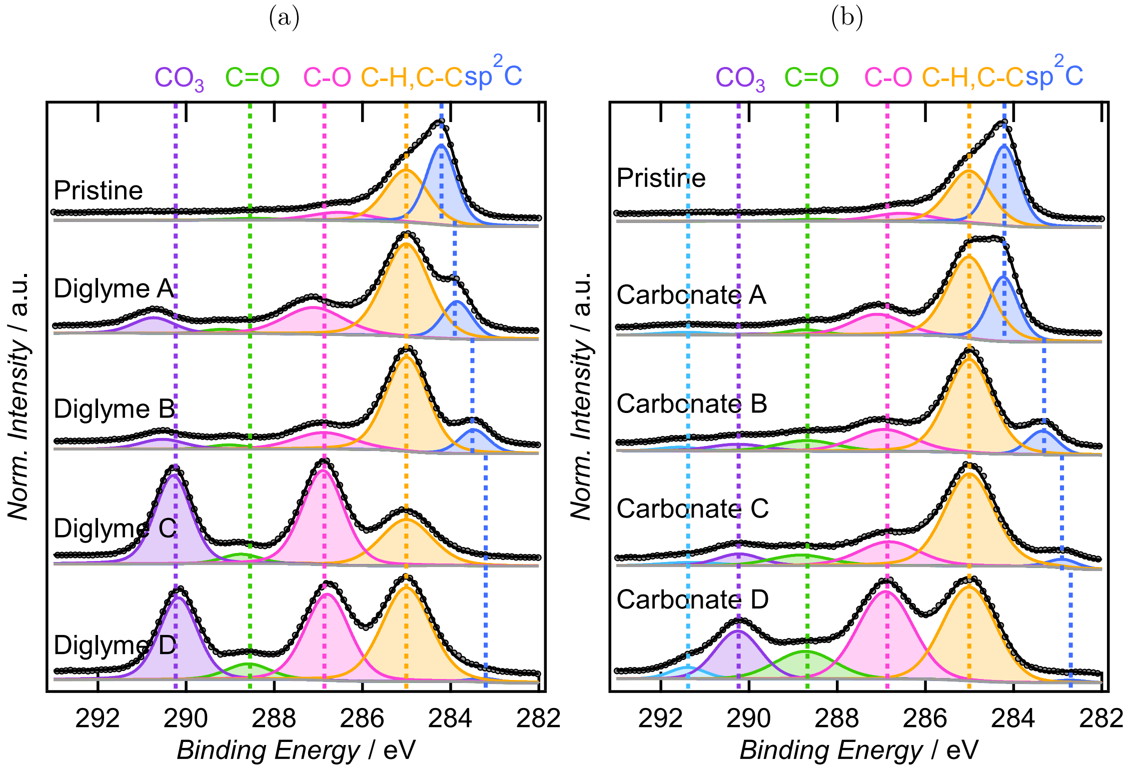

Figure 4.31: Curve-fitted C 1s spectra for the (a) Diglyme and (b) Carbonate samples. The dots show the data points and the black lines the total curve fits. All spectra are referenced in binding energy to the respective C−H/C−C peak (yellow) at 285 eV.

can lead to changes in the thickness and composition of the SEI.[68] In this study, the resting time decreased from the samples B to D. The different resting times might be another reason for the differences in the spectra.

Two trends can be observed for the sp^2 carbon peak. With increasing SoC it is (I) shifted toward lower binding energies and (II) its intensity is decreasing compared to, e.g., the C−H/C−C peak. Since such a large shift in binding energy of the sp^2 carbon peak (up to 1.5 eV) is not expected to be caused by an actual chemical shift due to the increasing sodium content in the HC,[96] the shift in binding energy might be a result of referencing the binding energy of the spectra to the C−H/C−C peak. The decreasing intensity of the sp^2 carbon peak could indicate an increasing thickness of the SEI with increasing SoC of the HC electrode. In the following, the two trends of the sp^2 carbon peak will be discussed in detail.

On the pristine electrode both, the photoelectrons contributing to the C−H/C−C peak as well as those contributing to the sp^2 peak, were emitted directly from the HC electrode surface. In contrast to that, for the HC electrodes, which were electrochemically cycled (samples B-D), the C−H/C−C peak mainly stems from the SEI, while the sp^2 peak is still a contribution of the HC composite. Since the HC composite is electronically conductive, but the SEI is not, these two layers might differ in their surface potential and an electric potential gradient might evolve between them. Such a behavior was already reported by Maibach *et al.* for lithiated graphite electrodes. They found that the difference between the binding energy of surface and bulk components was dependent on the SoC of the graphite electrodes, i.e., the OCV of the cells before the XPS measurements.[96] Similarly, in the C 1s spectra of the HC electrodes the difference in binding energy between the C−H/C−C peak and the sp^2 C peak increased with increasing SoC of the HC electrodes. In essence, the spectra herein are referenced in binding energy to a surface component, which introduces an deviation for the absolute binding energy of bulk components such as the sp^2 C peak. Consequently, the actual chemical shift of the sp^2 C peak due to the increasing sodium content cannot be assessed. Using the C−H/C−C peak as reference for the binding energy might also be the reason for the deviations of the C−O, C=O and CO_3 peak positions for the non-cycled samples A and the cycled samples B-D. For Diglyme A and Carbonate A some kind of surface layer seems to be formed, but it is probably thin enough so that the C−H/C−C peak contains contributions from the surface layer as well as from the bulk HC electrode.

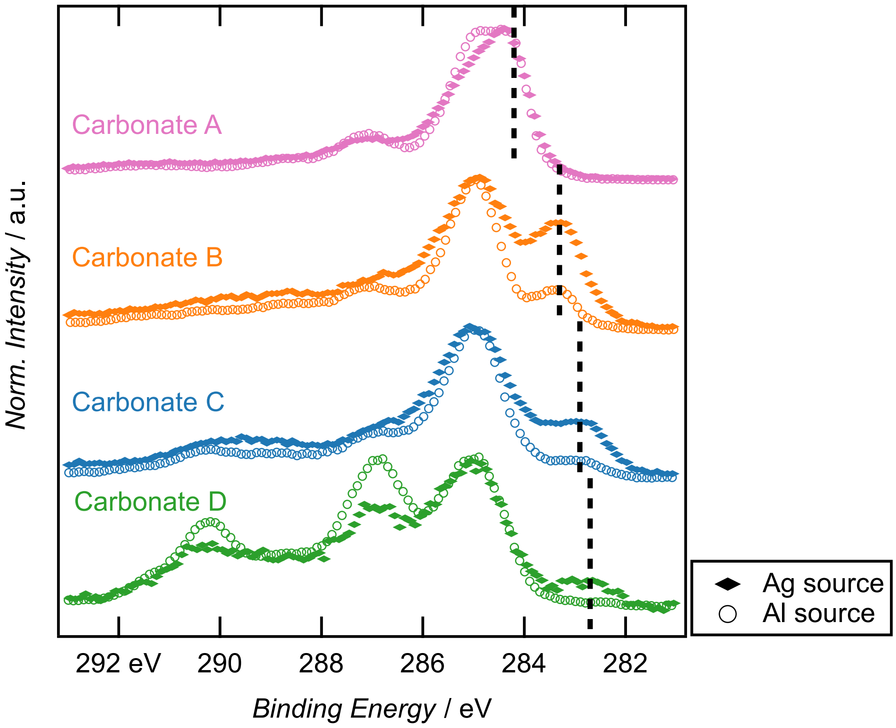

Figure 4.32: XP spectra of the C 1s region of the Carbonate samples obtained with an Al (circles) and an Ag (filled symbols) X-ray source. The vertical black dashed lines indicate the positions of the sp^2 C peak.

The second trend of the sp^2 peak is, that its intensity decreases with increasing SoC of the HC electrode. This indicates that the thickness of the SEI is increasing, since this peak is a contribution from the bulk HC composite. When the SEI on top of the HC electrode is thicker, less photoelectrons from this layer will reach the detector without being scattered. In order to verify that the intensity of the sp^2 peak is reduced due to a thicker SEI, XP spectra of the C 1s region were additionally recorded with an Ag X-ray source. The photon energy of Ag Lα (2984.2 eV) is about twice the photon energy of Al Kα (1486.6 eV), which was normally used as X-ray source in this study. Due to the higher photon energy the probing depth is increased. The probing depth is usually defined as three times the IMFP of the photoelectrons in the respective material.[18] For instance, the probing depth of the C 1s core level of the typical SEI component Na_2CO_3 is around 8 nm when an Al X-ray source is used (obtained from the NIST Electron Inelastic-Mean-Free-Path Database).[97] For an Ag X-ray source this increases up to 16 nm.[41] The XP spectra of the C 1s region obtained with the two different X-ray sources are compared for the Carbonate cells in Figure 4.32. With the vertical black dashed lines the positions of the sp^2 C peaks are indicated. For the non cycled sample (Carbonate A, pink) only minor differences depending on the probing depth were found, but for all cycled samples (Carbonate B-D) the intensity of the sp^2 C peak is significantly enhanced when the probing depth is increased. This confirms that the sp^2 C peak is indeed a contribution from the bulk HC composite covered by an SEI, which is growing in thickness with increasing SoC. Similar XP spectra were obtained with the Ag source for the Diglyme cells.

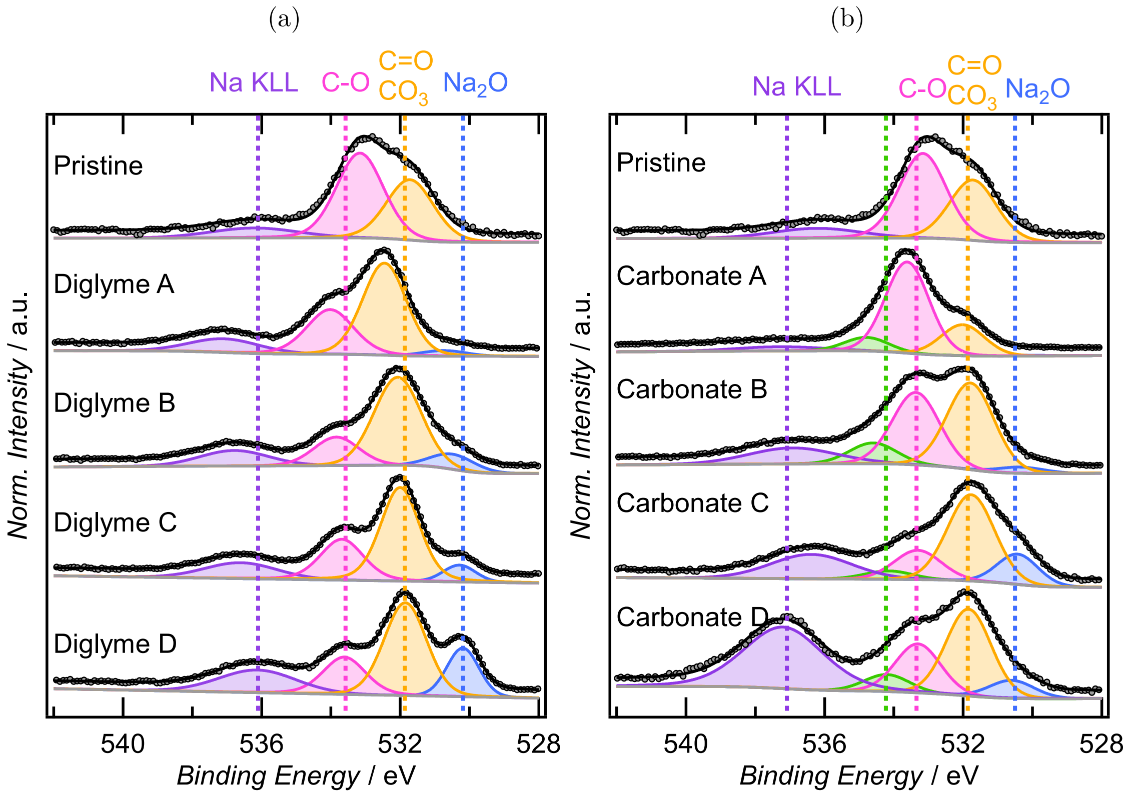

Figure 4.33: Curve-fitted O 1s spectra for the (a) Diglyme and (b) Carbonate samples. The dots show the data points and the black lines the total curve fits. All spectra are referenced in binding energy to the respective C−H/C−C peak at 285 eV (cf. Figure 4.31).

In Figure 4.33 the curve-fitted XP spectra of the O 1s region are shown for all samples. The binding energy was referenced to the C–H/C–C peak from the respective C 1s spectra (cf. Figure 4.31). As discussed above this can lead to deviations of the binding energies of the same species on different samples. These deviations are especially pronounced when the non-cycled samples (Pristine or Sample A) are compared with the cycled samples (Sample B, C and D) as explained above. In all spectra, contributions from C–O and C=O/CO_3 species were found in accordance with literature reports for HC electrodes cycled in diglyme electrolyte solution,[34] or carbonate electrolyte solution.[90] Additionally, a Na KLL Auger peak was observed at binding energies higher than 536 eV. The Na Auger peak is rather broad (FWHM 3 eV) and its relative intensity slightly increases with increasing sodiation state of the HC electrode. It should be noted that for the fully sodiated HC electrodes (Diglyme D and Carbonate D) the relative intensity of the Na Auger peak is much higher for the Carbonate sample compared to the Diglyme sample. This could indicate that on the Carbonate sample the relative amount of oxygen-containing SEI components is lower than on the Diglyme sample. An additional peak evolved at a binding energy of around 530 eV on the cycled HC electrodes (samples B, C and D). This can most likely be ascribed to Na_2O, which has an O 1s binding energy of 529.5 eV.[66] In general the relative intensity of the Na_2O peak increases with increasing SoC of the HC electrode. The peak at around 534 eV (green) on the Carbonate samples might stem from an FEC decomposition product.[93]

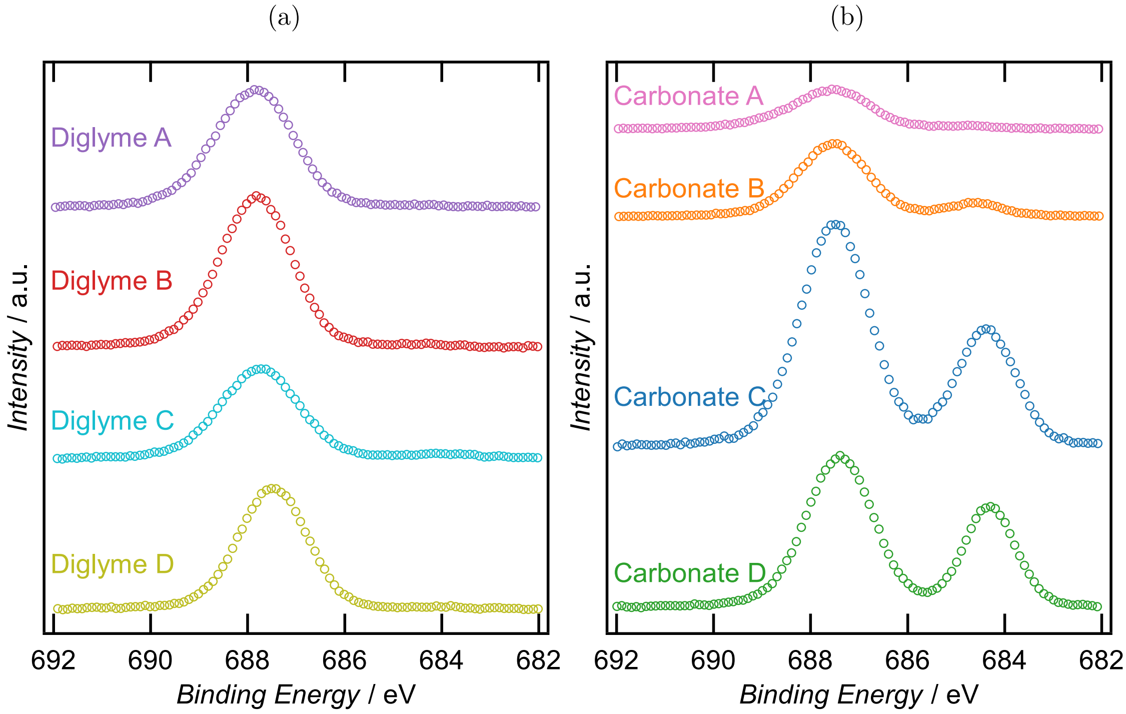

Figure 4.34: XP spectra of the F 1s region for the (a) Diglyme and (b) Carbonate samples. All spectra are referenced in binding energy to the respective C–H/C–C peak at 285 eV (cf. Figure 4.31).

The XP spectra of the F 1s region are shown in Figure 4.34. In all spectra the main peak is located at around 687.5 eV and presumably contains contributions from different fluorinated phosphate species. For instance, $NaPF_6$ (characteristic binding energy 687.1 eV[66]), which was used as salt in both electrolyte solutions, or possible decomposition products from the salt (Na_xPF_y), which were also found in other studies.[90] The second peak, which is hardly visible for the Diglyme samples but quite pronounced for the Carbonate C and D samples is located around 684.4 eV. This is attributed to contributions from NaF (characteristic binding energy 684.8 eV) on the surface. NaF can also be formed during the XPS measurements due to decomposition of, e.g., $NaPF_6$ caused by X-ray radiation. Thus, it is difficult to evaluate how much NaF was present on the HC electrodes after cycling, but before the XPS measurements. A rough estimate of this effect was obtained by measuring the F 1s region a second time at the end of all XPS measurements. Indeed, the relative intensity of the NaF peak increased with increasing time of X-ray beam exposure, but this increase can not explain the complete amount of NaF seen on the Carbonate C and D samples (Figure 4.34 (b)). Thus, it is assumed that NaF was part of the SEI on the HC electrodes, which were cycled in the Carbonate electrolyte solution. This might be a result of the FEC additive used in the Carbonate electrolyte solution.[41]

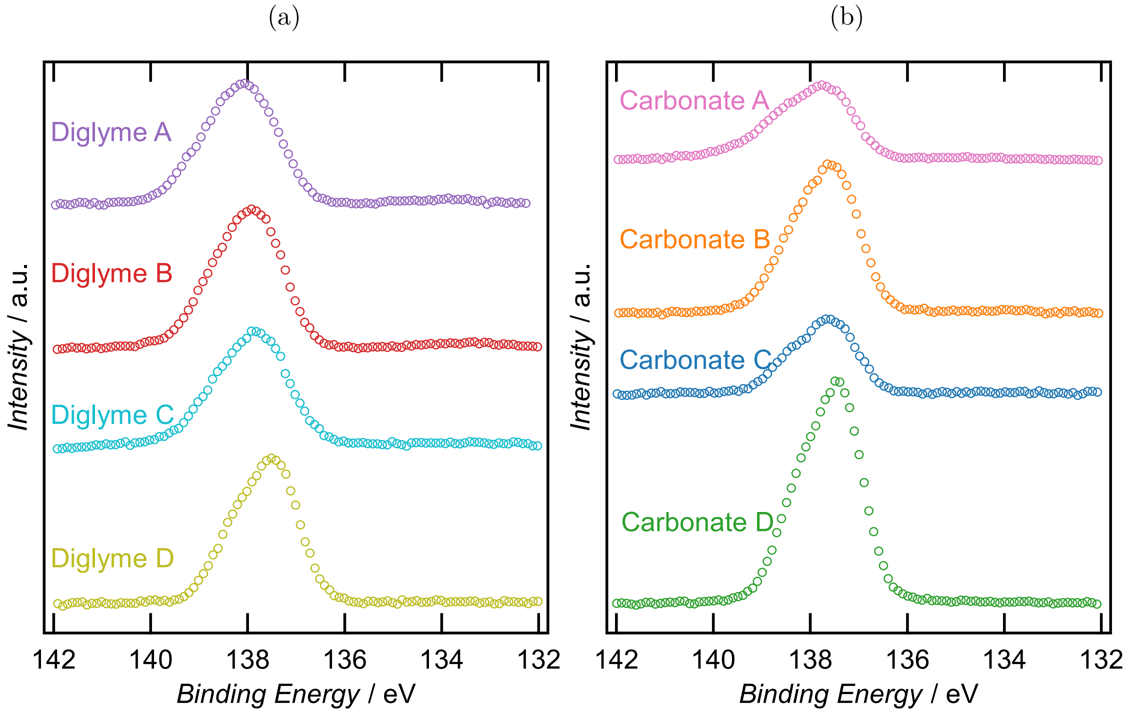

Figure 4.35: XP spectra of the P 2p region for the (a) Diglyme and (b) Carbonate samples. All spectra are referenced in binding energy to the respective C−H/C−C peak at 285 eV (cf. Figure 4.31).

In the XP spectra of the P 2p region shown in Figure 4.35 only one main peak was found. Its asymmetry is rooted in the spin-orbit splitting of the 2p level into $2\,p_{3/2}$ and $2\,p_{1/2}$, i.e., the peak consists of two peaks with the intensity ratio 2:1

($2\,p_{3/2}$:$2\,p_{1/2}$). The peak can be attributed to $NaPF_6$.[66] It might also contain contributions from Na_xPF_y, but P−O containing species can be excluded as they should appear at lower binding energies (e.g., 133.9 eV was measured for Na_2PFO_3). The XP spectra of the F 1s and the P 2p region were dominated by the contributions of $NaPF_6$. This indicates that a lot of electrolyte solution residues were present on the HC electrodes, although all samples were washed with DMC and dried under vacuum before being introduced into the measurement chamber (see chapter 3.4). A possible reason for this could be, that electrolyte solution was trapped in the porous structure of the HC composite or the SEI and was not removed by the cleaning procedure.

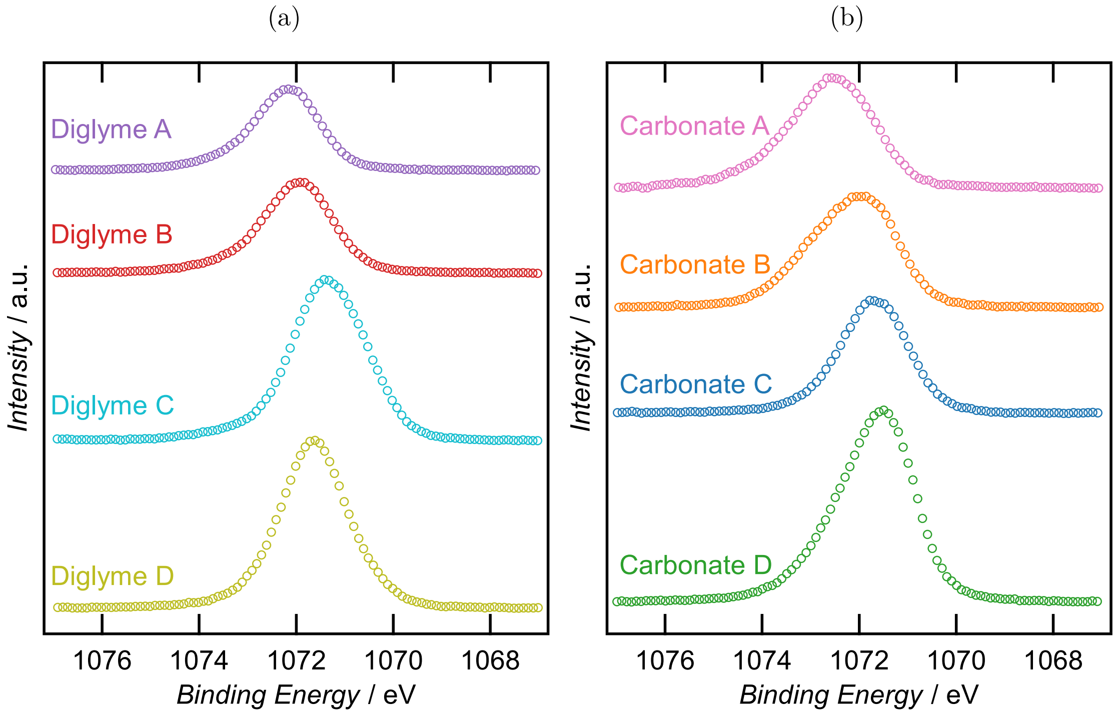

Figure 4.36: XP spectra of the Na 1s region for the (a) Diglyme and (b) Carbonate samples. All spectra are referenced in binding energy to the respective C−H/C−C peak at 285 eV (cf. Figure 4.31).

In the Na 1s region shown in Figure 4.36 only one peak was found. It probably consists of overlapping peaks stemming from different Na containing species ($NaPF_6$, NaF, Na_2O) but also from Na which was inserted into the HC. These contributions can not be disentangled, as the variation of the binding energy of the Na 1s core level among the different compounds is only around 1 eV.[66] Additionally, the difficulties in referencing the binding energy described above don't allow for further interpretation.

4.5.3 Conclusions

XP spectra of HC electrodes, which were either pristine, soaked with electrolyte solution or cycled to different SoCs were recorded. Charging effects caused by the electronically insulating nature of the SEI, which covered the HC electrodes, caused shifts of the binding energy up to 2 eV. This effect was especially pronounced for the HC electrodes cycled to a high SoC and rendered the determination of exact binding energies difficult. In order to compare the different spectra, the C−H/C−C peak was used as a reference for the binding energy. Since this peak might be a result of electrons from the bulk HC material and the SEI, which are affected differently by the charging effects, this reference is prone to be erroneous.

On HC electrodes, which were not cycled, small amounts of typical SEI components were found, indicating that some kind of surface layer was formed due to the contact with the electrolyte solution. After cycling, all HC electrodes were covered with an SEI, but the measurements at different SoCs revealed, that the SEI on the HC electrodes is still changing with the SoC in the 6^{th} charging cycle. With increasing SoC, i.e., with increasing Na content in the HC, the SEI is becoming thicker, which was reflected in the decreasing intensity of the sp^2 C peak of the HC material. Additionally, the composition of the SEI is changing with the SoC. In general, more inorganic species were detected at high SoCs. The additive FEC used in the Carbonate electrolyte solution, led to the unambiguous presence of NaF in the SEI.

4.5.4 Impact of the SEI Instability on the Microcalorimetric Measurements

The XPS measurements of HC electrodes at different SoCs showed that the SEI is still changing with the SoC in the 6^{th} charging cycle. This could possibly influence the microcalorimetric pulse experiments in two ways.

(1) A part of the charge of the microcalorimetric pulses with a negative current amplitude could drive the decomposition of electrolyte solution instead of the sodiation of HC. This could lead to less reversibly exchanged heat during the negative current pulses compared to the positive current pulses. However, this would require that the equilibrium potential of the HC electrode at a specific SoC would have to be close to the decomposition potential of the electrolyte solution, which is probably not the case. Instead, when parts of the SEI are continuously dissolved, it is expected that the SEI is also continuously reformed through decomposition of the electrolyte solution. These processes can take place without external current flow. Na^+ ions could be extracted from the HC electrode to reform the SEI, which would consequently lead to self-discharge of the HC electrode.

(2) It is more likely that the state of the SEI, such as the thickness of the SEI, influences the sodiation/desodiation process of HC itself. For instance, a thicker SEI could lead to delayed transfer of Na^+ ions through the SEI, which could be reflected in the temporal evolution of the heat upon short sodiation/desodiation pulses of HC.

In order to evaluate the impact of the SEI instability on the microcalorimetric results, in the following the microcalorimetric pulse experiments of HC in 1 M $NaPF_6$/ diglyme of the 8th cycle (which were discussed so far) are compared with those of the 2nd cycle. In the 2nd cycle the cutoff potential was reached after $267\,\mathrm{mAh\,g^{-1}}$ during charging (sodiation), but during discharging the cutoff potential was already reached after $232\,\mathrm{mAh\,g^{-1}}$. This amounts to a coulombic efficiency of 87 %. In contrast to that, the coulombic efficiency in the 8th cycle was 97 %. Hence, more SEI formation and consequently a greater variation of the state of the SEI is expected in the 2nd cycle compared to the 8th cycle.

In Figure 4.37 the current, potential, temperature and heat transients of exemplary sodiation/desodiation pulses of a HC composite electrode in 1 M $NaPF_6$/diglyme at a SoC of 4 % and 54 % are compared for the 2nd (light colors) and 8th (dark colors) cycle. At a SoC of 4 % (Figure 4.37 (a) and (b)) the potential transients measured in the 2nd cycle slightly differ from those measured in the 8th cycle. This is mainly due to the difference in the initial potential (1.008 V vs. 1.019 V for the 2nd and the 8th cycle, respectively). The polarization of the electrode immediately after the current pulses (after correction for the iR-drop) was only ca. 7 mV higher in the 2nd cycle compared to the 8th cycle. In the temperature and heat transients no significant differences were observed. At a SoC of 54 % (Figure 4.37 (c) and (d)) the initial potentials were 0.086 V and 0.077 V for the 2nd and the 8th cycle. The difference in the polarization of the electrode increased significantly, so that the potentials immediately after the current pulses differed by around 70 mV considering the different initial potentials. At a SoC of 54 % the temperature and the heat transients measured in the 2nd and the 8th cycle show slight deviations. At $t = 160\,\mathrm{ms}$ after the sodiation pulse (Figure 4.37 (c)) ca. 0.3 µJ less, and after the desodiation pulse (Figure 4.37 (d)) ca. 0.3 µJ more heat was exchanged in the 2nd cycle compared to the 8th cycle. This is presumably caused by the higher polarization observed in the 2nd cycle leading to more polarization heat according to equation 2.14. Indeed, the difference in the polarization of 70 mV multiplied with the pulse charge $dQ = 3.4\,\mathrm{\mu C}$ yields a polarization heat of $|\delta q_{\mathrm{pol}}| = -zF|\eta|d\xi = -|\eta dQ| = -0.24\,\mathrm{\mu J}$, close to the observed difference in the heat.

However, differences in the polarization heat shouldn't influence the resulting reaction entropy, as it is is determined from the reversibly exchanged heat (obtained by interpolation to zero overpotential). The reaction entropy from the microcalorimetric pulse measurements for the 2nd and the 8th charging cycle is shown in Figure

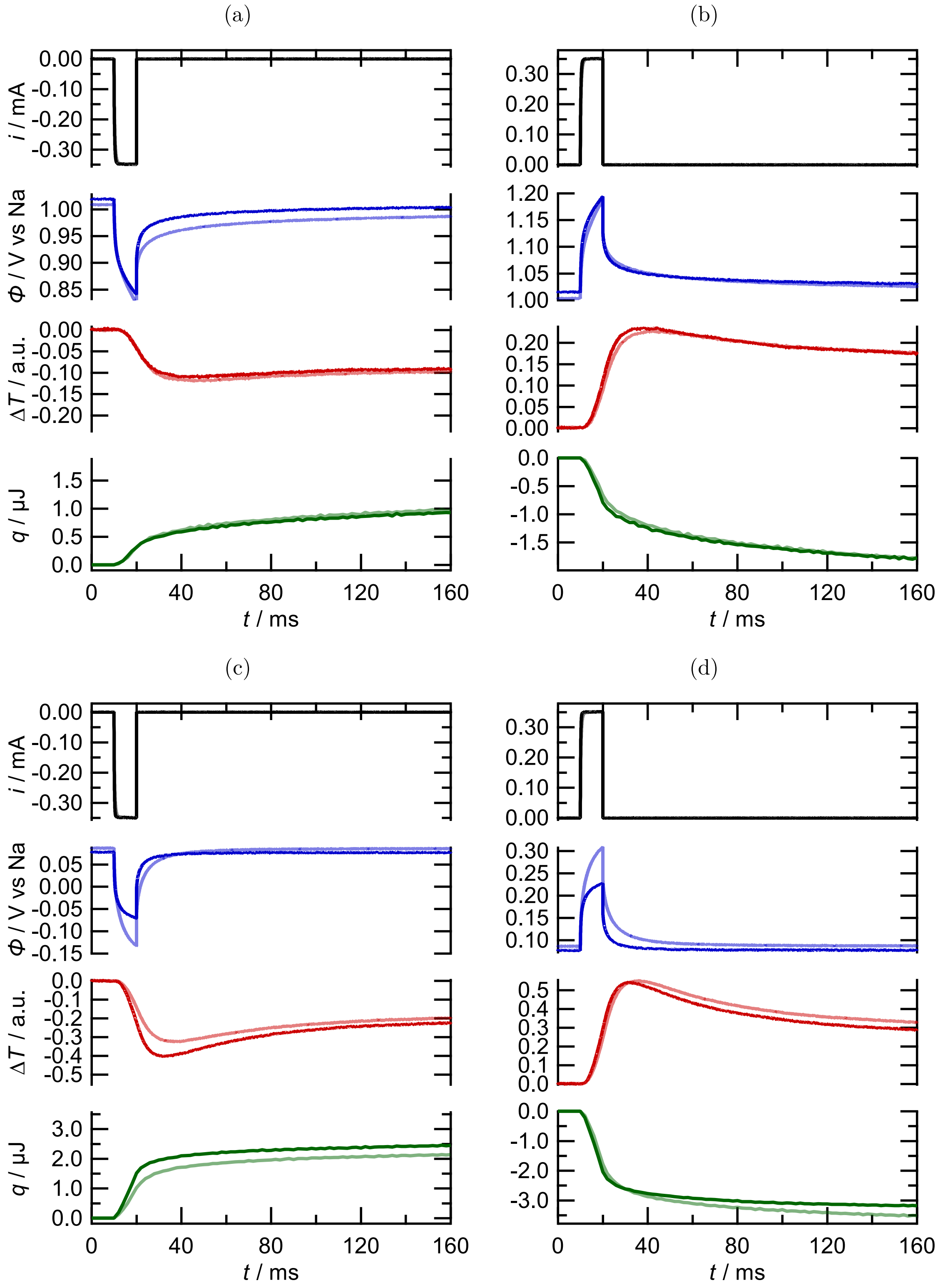

Figure 4.37: Current i, potential ϕ and temperature ΔT transients and the heat q resulting from 10 ms current pulses of a thin HC electrode (20 µm) in 1 M $NaPF_6$/diglyme. All transients shown with the light color were recorded in the 2nd cycle, and the ones with the dark color in the 8th cycle. The SoC was 4 % in (a) and (b), and 54 % in (c) and (d).

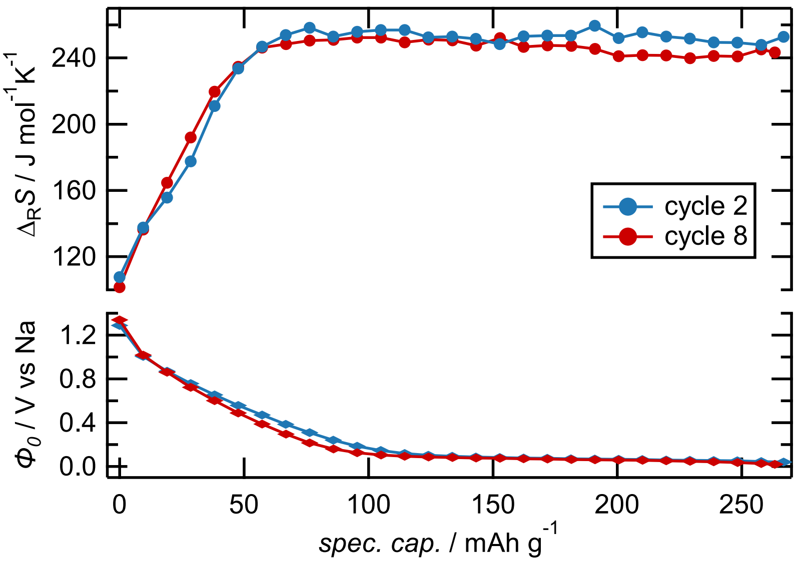

Figure 4.38: Comparison of the reaction entropy $\Delta_{\mathrm{R}}S$ and ϕ_0 in the charging cycle of a thin HC electrode (20 µm) in 1 M $NaPF_6$/diglyme in the 2nd and the 8th charging cycle.

4.38. A very similar reaction entropy was found in the 2nd and the 8th cycle. Note that this was also the case when 1 M $NaClO_4$/PC(+FEC) was used instead of 1 M $NaPF_6$/diglyme. Thus, although there might be changes of the composition and the thickness of the SEI with varying SoC, they did not significantly influence the reaction entropy determined with microcalorimetry.

Nevertheless, at a SoC of 54 % the polarization of the electrode upon sodiation and desodiation pulses was only half as strong in the 8th cycle compared to the 2nd cycle (see Figure 4.37 (c) and (d)), which consequently led to less polarization heat in the 8th cycle. Such a lower polarization can, e.g., be rooted in a lower charge-transfer resistance or a higher double layer capacitance. With EIS Lv *et al.* found that the charge-transfer resistance of HC in 1 M $NaPF_6$/diglyme decreases by about 30 % from the 1st to the 10th cycle. This in contradiction to the EIS study by Aniskevich *et al.*, who found that for HC in 1 M $NaPF_6$/PC+FEC the charge-transfer resistance increases by about 40 % and the double layer capacitance decreases by about 25 % from the 1st to the 10th cycle.[55] With the information of the EIS studies the reason for the higher polarization of the HC electrode at a SoC of 54 % in 1 M $NaPF_6$/diglyme in the 2nd cycle compared to the 8th cycle could not be clarified. In addition, it should be noted that such a higher polarization was not observed for the microcalorimetric pulse measurements with 1 M $NaClO_4$/PC electrolyte solution.

5

Charging Process of Sodium Vanadium Phosphate

In general, three different material classes are investigated for the positive electrode in SIBs: layered oxides, Prussian blue analogues and polyanionic compounds.[7] This diversity is also reflected in the commercialization of SIBs, for which different manufacturers pursue the application of different chemistries for the positive electrode in SIBs.[6] Layered oxides have a high intrinsic electronic conductivity and exhibit the highest energy density among the three material classes.[7] However, layered oxide electrodes tend to degrade faster due to phase transitions with high volume expansion during charging/discharging, ultimately leading to a poor cycling stability.[4, 7] This is in contrast to the Prussian blue analogues and the polyanionic compounds, in which the strong covalent bonds lead to a robust network, which allows for long-term cycling.[7] In addition, Prussian blue analogues can possibly be cheaper than the layered oxides due to, e.g., low cost raw materials, although the final electrode materials have to be vacancy free and have to have a low water content.[4] Polyanionic compounds are promising due to their tunable redox potential, as well as their low-energy Na^+ ion migration pathways in their open structure. Yet, low intrinsic electronic conductivity, and their heavy mass, which leads to low specific capacity, pose possible drawbacks.

In the following chapter the charging mechanism of $Na_3V_2(PO_4)_3$ (NVP) will be investigated. NVP is a typical representative of the polyanionic compounds. It was used within the POLiS Cluster of Excellence as material for the positive electrode in the SIB reference system, due to its high cycling stability.[40] First, an overview of the current state of research is given in chapter 5.1. In chapter 5.2 microcalorimetric measurements of the reaction entropy of the charging/discharging process will be discussed. Lastly, the determination of the cell reaction entropy of NVP/C|HC coin cells with entropy profiling is shown in chapter 5.3.

5.1 Current State of Research

$Na_3V_2(PO_4)_3$ has a NASICON (NA-Super-Ionic-CONductor) structure.[8] The structure consists of PO_4 tetrahedrons and VO_6 octahedrons, which create a 3D framework with large tunnels for Na^+ ion diffusion.[4] The crystal structure of $Na_3V_2(PO_4)_3$ with the two distinct sites for Na is shown in Figure 5.1. Although a rhombohedral unit cell is commonly reported for NVP, Chotard *et al.* found with powder and single crystal XRD, that it should rather be indexed in the monoclinic space group C2/c.[99]

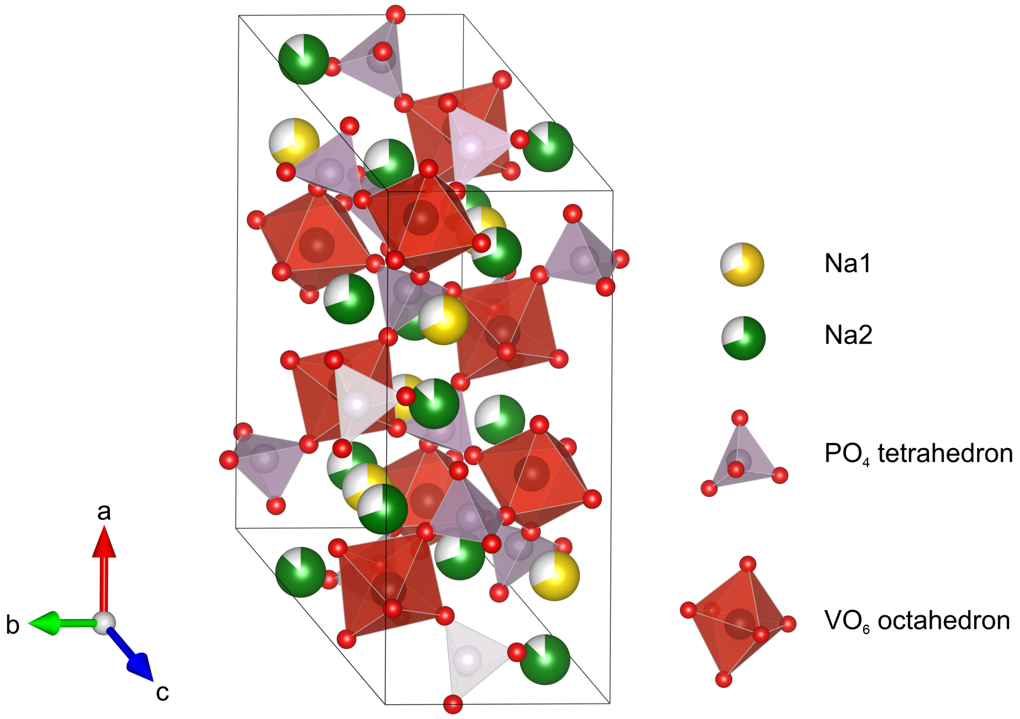

Figure 5.1: Crystal structure of $Na_3V_2(PO_4)_3$ in the monoclinic space group C2/c. The structure parameters reported by Park *et al.* were used.[9] The structure was visualized using VESTA.[98]

Na^+ ions can be either inserted into or extracted from $Na_3V_2(PO_4)_3$, i.e., NVP can be used as material for the negative or the positive electrode.[100] The insertion of one Na^+ ion per formula unit takes place at 1.7 V and leads to $Na_4V_2(PO_4)_3$. More common is the the usage as positive electrode, since at a potential of around 3.4 V two Na^+ ions can be extracted per $Na_3V_2(PO_4)_3$ formula unit to form $NaV_2(PO_4)_3$.[8] Based on *in situ* XRD measurements, Jian *et al.* proposed that during charging/discharging a two-phase reaction with a volume change of 8.26 % takes place.[101]

$$Na_3{V_2}^{+III}(PO_4)_3 \rightleftharpoons Na_1{V_2}^{+IV}(PO_4)_3 + 2Na^+ + 2\,e^- \tag{5.1}$$

In a further study, they found that in $Na_3V_2(PO_4)_3$ two different sites exists for Na (Na1 and Na2 in Figure 5.1), but in $NaV_2(PO_4)_3$ only one coordination environment exists for Na (Na1).[102] They concluded that only the Na^+ ions from the Na2 site are extracted during charging. This was confirmed by DFT simulations by Wang *et al.*, albeit they showed that the Na1 site is involved in the solid diffusion of Na^+ ions in NVP as well.[103] More recently, Park *et al.* could resolve the structure of an intermediate phase $Na_2V_2(PO_4)_3$ with *operando* synchrotron XRD.[9] The intermediate phase appeared during charging/discharging, i.e., under non-equilibrium conditions. Since the unit cell volume of $Na_2V_2(PO_4)_3$ lies between those of $NaV_2(PO_4)_3$ and $Na_3V_2(PO_4)_3$, the interfacial strain during the phase transition is reduced when the intermediate phase is involved. Additionally, they observed that the maximum phase fraction of the intermediate phase was different during charging and discharging.

A well-known problem of phosphate-based frameworks for the application as electrode material is their low electronic conductivity.[4] This can be solved by carbon coating of the active material, which was first reported for NVP by Jian *et al.* in 2012.[104] Since then, carbon coated NVP, herein referred to as NVP/C, is used. NVP/C showed high cycling stability in symmetrical cells,[100] as well as in combination with HC.[39] The experiments presented herein were also performed with NVP/C composite electrodes. The active material NVP/C was produced by spray drying in the group of Dr. Joachim Binder (IAM-ESS, KIT).[40] The electrodes were processed by Marcus Müller in the group of Dr. Werner Bauer (IAM-ESS, KIT).

In addition to the investigations of the structural changes of NVP, the heat generation during charging/discharging of cells with NVP was measured.[105, 106] For example Mohsin *et al.* found with isothermal calorimetry that less heat was generated during charging of a NVP/C|HC cell compared to discharging.[105] They ascribed this to reversible heat generation, such as through entropic changes, which has to be endothermic during charging and exothermic during discharging. In general, the reaction entropy of charging/discharging processes can give insights into the charging mechanism. It can, e.g., be distinguished between a solid solution or a two-phase charging mechanism.[63] Wei *et al.* determined the cell reaction entropy of a NVP/C|Na metal cell with entropy profiling. A constant value of around $-15\,\mathrm{J\,mol^{-1}\,K^{-1}}$ was found in the potential plateau (between a SoC of 10 % and 90 %), which indicated that a two-phase reaction is taking place.[64]

Research Questions

The overview of the current state of research shows that the charging mechanism of NVP is not fully understood. To contribute to a better understanding of the charging mechanism, the reaction entropy of charging/discharging of NVP/C is determined with electrochemical microcalorimetry and entropy profiling. Among others, the following questions will be addressed in the following chapters.

- What are the main contributions to the reaction entropy of the charging/discharging of NVP/C?
- Which insights about the charging mechanism of NVP/C can be derived from the SoC-dependent reaction entropy of charging/discharging of NVP/C? Are there, e.g., differences in the charging and the discharging cycle?

5.2 Microcalorimetric Measurements

5.2.1 Measurement Procedure

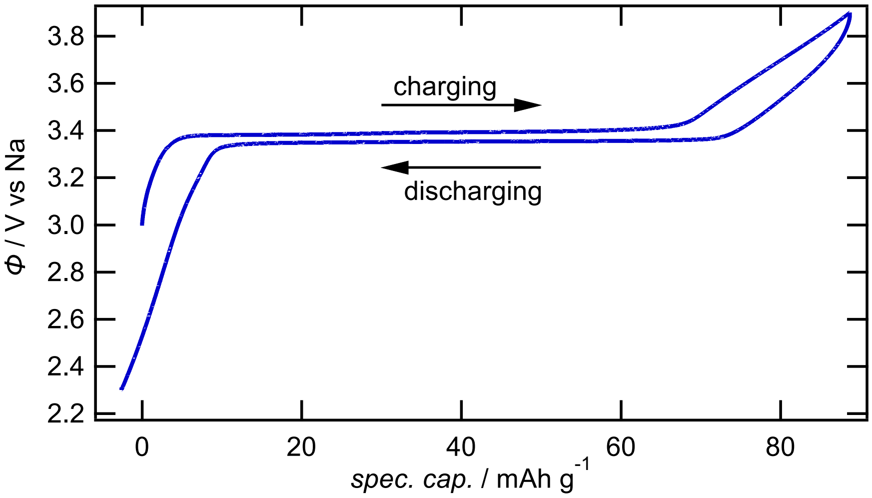

Figure 5.2: Charging and discharging curve of the 1st cycle with a current of ±20 µA (≈C/8) of a NVP/C composite electrode in 1 M $NaPF_6$/EC,PC+FEC with an upper potential limit of 3.9 V and a lower potential limit of 2.3 V. The specific capacity is referenced to the mass of the NVP/C in the composite electrode.

Before the microcalorimetric pulse measurements, the NVP/C electrode was charged and discharged once with a rate of about C/8 between 2.3 V and 3.9 V. The resulting potential curve of the 1st cycle is shown in Figure 5.2. A potential plateau around 3.4 V can be seen. The values of the potential plateaus during charging/discharging differ by about 40 mV, which can be explained with the iR-drop as well as polarization of the electrode during charging/discharging. A specific capacity of around 90 mAh g^{-1} (referenced to the mass of the NVP/C) was reached, which is in accordance with the literature.[39] The microcalorimetric measurements were performed in the 2nd cycle. The measurement protocol was similar to that used for the HC electrodes (see chapter 4.2). CC phases (20 min, C/11 rate) were followed by OC phases (40 min). After the relaxation phase at OC conditions, 10 ms current pulses with alternating and different amplitudes were applied for the microcalorimetric measurements.

In Figure 5.3 the current, potential and temperature transients of an exemplary 10 ms (a) discharging and (b) charging pulse of a NVP/C electrode at a SoC of 49 % in 1 M $NaPF_6$/EC,PC+FEC are shown. Current flow in the external circuit was only allowed during the current pulse from t = 10 ms to 20 ms and OC conditions were applied before and after the pulse. Since short pulses were used, the SoC of the electrode only changed by about 10^{-5} of the full capacity with a single current pulse. As soon as the current was applied at t = 10 ms, the potential was de-/increasing

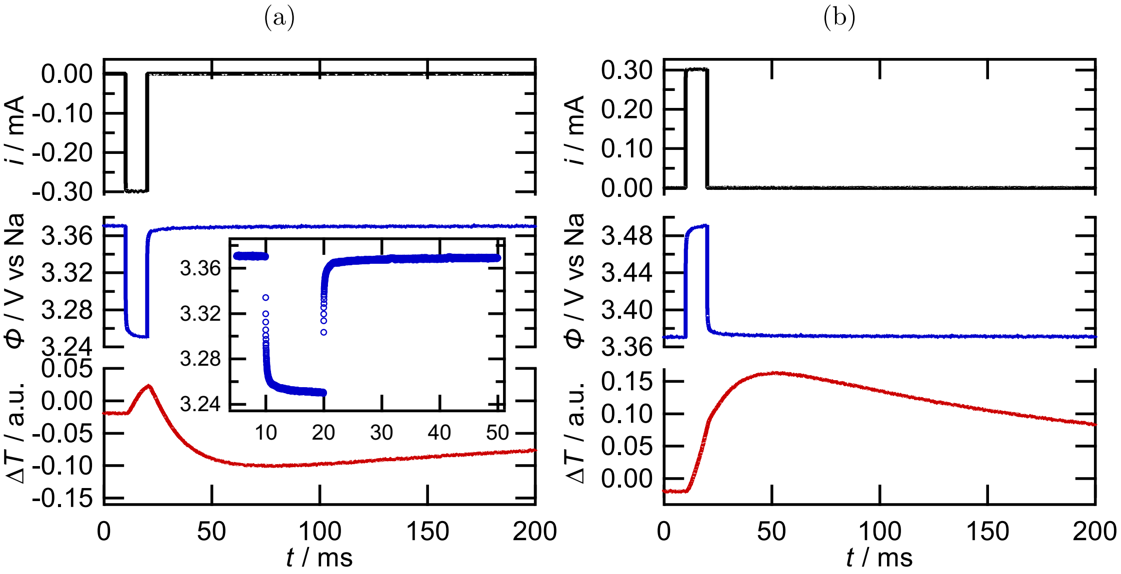

Figure 5.3: Current i, potential ϕ and temperature ΔT transients resulting from a 10 ms (a) negative and (b) positive current pulse of a NVP/C composite electrode at a SoC of 49 % in 1 M $NaPF_6$/EC,PC+FEC. In the inset in (a) the single data points of the potential transient are shown from $t = 5$ ms to $t = 50$ ms.

stepwise by more than 100 mV. During the current pulse the potential only varied by less than 15 mV. When the cell was set to OC conditions at $t = 20$ ms, the potential was in-/decreasing stepwise again. The following relaxation of the potential was finished at around $t = 50$ ms. When the current was switched off at $t = 20$ ms, the potential changed only by about 54 mV between two consecutive data points ($t = 20.00$ ms and $t = 20.01$ ms) for the negative and the positive current pulse (see the inset in Figure 5.3 (a)). Consequently, only the half of the stepwise potential change can be ascribed to iR-drop through the electrolyte solution, while the other half might be caused by the charge-transfer resistance of the electrochemical reaction at the NVP/C electrode. The fast equilibration of the electrode potential, after the cell is set to OC conditions for $t > 20$ ms, indicates a fast charge-transfer reaction at the NVP/C electrode.

While the potential transients are very similar for the discharging and the charging pulse, the temperature transients differ significantly. For the discharging pulse (Figure 5.3 (a)) the temperature of the electrode was increasing from $t = 10$ ms to $t = 20$ ms, followed by a temperature decrease for $t > 20$ ms. A minimum of the temperature was reached at around $t = 80$ ms, followed by a relaxation of the temperature toward the initial temperature. In the case of charging (Figure 5.3 (b)), the temperature was increasing during the current pulse as well as after the current pulse. The temperature reached a maximum at $t = 50$ ms. The differences between the temperature transients caused by a discharging and a charging pulse indicate that for $t < 20$ ms irreversible heat contributions are dominating, and for $t > 20$ ms reversible heat contributions are dominating (for a detailed discussion see chapter 5.2.4). However, *a priori*, it is not clear whether this is caused by different time constants of the processes causing the heat exchange, or due to slow heat transfer within the 99 µm thick and porous NVP/C electrode. The different causes for a delayed temperature transient can be differentiated by deconvolving the temperature transient to yield the heat transient (see chapter 3.1). For that purpose the thermal response function of the NVP/C electrode-sensor stack is needed. As it will be discussed in the following chapter, this presented a challenge of the microcalorimetric experiments with the NVP/C electrodes, since the electrochemical processes are probably not confined to the electrode surface but can occur throughout the entire composite electrode thickness.

5.2.2 Thermal Response of the NVP/C Electrode

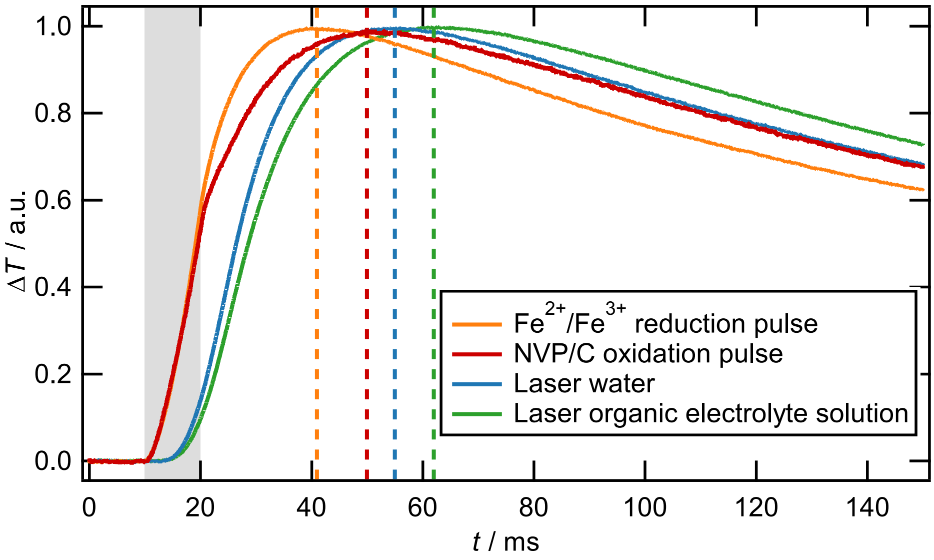

Figure 5.4: Temperature transients of the 99 µm thick NVP/C electrode upon 10 ms heat inputs from different sources (time interval marked in gray, experimental conditions described in the text). The maxima are normalized to one. The vertical dashed lines indicate the time, at which the temperature maxima were reached.

In Figure 5.4 the temperature transients of the 99 µm thick NVP/C electrode upon heat inputs from the following different sources are compared. All temperature transients were recorded within one microcalorimetric experiment, i.e., with the same electrode-sensor stack. The measurements were performed in the order shown here.

- A 10 ms positive current pulse (300 µA) of the NVP/C electrode in 1 M $NaPF_6$/EC,PC+FEC, (cf. Figure 5.3) (shown in red).
- Laser irradiation (10 ms) of the NVP/C electrode with 1 M $NaPF_6$/EC,PC +FEC in the electrochemical cell (shown in green).

- Laser irradiation (10 ms) of the NVP/C electrode with water in the electrochemical cell (shown in blue).
- A 10 ms negative current pulse (−800 µA) of the NVP/C electrode in 0.1 M $K_3[Fe(CN)_6]/K_4[Fe(CN)_6]$ aqueous electrolyte solution (shown in orange). The electron transfer reaction in the $[Fe(CN)_6]^{4-}/[Fe(CN)_6]^{3-}$ redox system was used for the calibration of the microcalorimeter.

It can be clearly seen that the times at which the temperature maxima are reached (marked with the dashed lines in Figure 5.4) differ from each other. To understand these differences two main characteristics of the heat inputs have to be known: (I) when is the heat evolved (only for $t \leq 20\,\mathrm{ms}$ or also for $t > 20\,\mathrm{ms}$), and (II) where is the heat evolved (at which distance to the temperature sensor). For the Fe^{3+} reduction, it can be assumed that its heat input is completed shortly after $t = 20\,\mathrm{ms}$, since the electrochemical $[Fe(CN)_6]^{4-}/[Fe(CN)_6]^{3-}$ redox reaction is known to be a fast electrochemical reaction.[107–109] This might be different for the NVP/C oxidation. Slower processes, such as slow solvation of the Na^+ ions might contribute to the heat input, as it was, e.g., observed during desodiation of HC. Such a delayed heat input could explain why the thermal responses of the Fe^{3+} reduction and the NVP/C oxidation equal each other for $t < 20\,\mathrm{ms}$, but for $t > 20\,\mathrm{ms}$ the temperature transient caused by the NVP/C oxidation is increasing slower and the temperature maximum is reached later.

For the irradiation of the electrode with a laser, the time interval of the heat input is precisely defined. But only the top layer of the electrode is heated and the heat has to be transferred over the complete thickness of the NVP/C electrode until the temperature change is measured by the sensor. The composite electrode is soaked with electrolyte solution and the electrochemical processes can take place in the complete volume of the composite electrode. Thus, the heat inputs caused by the electrochemical reactions (Fe^{3+} reduction, NVP/C oxidation) are presumably spatially distributed within the porous electrode. This could explain why the temperature maxima caused by the electrochemical reactions are reached earlier than those caused by irradiation with a laser. In order to asses whether slow heat transfer through the NVP/C electrode can realistically account for the delayed temperature maxima found after irradiation of the electrode with a laser, the thermal relaxation time of the NVP/C electrode can be calculated. The thermal relaxation time τ is an estimation of the time, in which a temperature gradient that extends over a spatial region of the length d decays. It can be calculated with the density ρ, the specific heat capacity c_m and the thermal conductivity λ.[110]

$$\tau = \frac{d^2 \rho c_m}{\lambda} \tag{5.2}$$

Unfortunately, no values for the specific heat capacity and the thermal conductivity for NVP/C composite electrodes were available. However, these parameters were found for two typical positive composite electrodes for LIBs: a $LiFePO_4$ composite electrode without electrolyte solution,[111] and a $LiCoO_2$ composite electrode, which was soaked with electrolyte solution.[112] The thickness of the herein investigated NVP/C composite electrodes was used as length $d = 99\,\mu m$. The parameters and the resulting thermal relaxation times are summarized in Table 5.1.

	$\rho/\mathrm{kg\,m^{-3}}$	$c_m/\mathrm{J\,kg^{-1}K^{-1}}$	$\lambda/\mathrm{W\,m^{-1}K^{-1}}$	τ/ms
dry $LiFePO_4$ composite electrode	2310[111]	778[111]	0.27[111]	67
wet $LiCoO_2$ composite electrode	2329[112]	1269[112]	1.58[112]	19

Table 5.1: Thermal relaxation time τ calculated with the density ρ, the specific heat capacity c_m and the thermal conductivity λ according to equation 5.2. Two different positive composite electrodes for LIBs are compared. A thickness of $d = 99\,\mu m$ was assumed.

Relaxation times of 67 ms for the $LiFePO_4$ composite electrode, and 19 ms for the $LiCoO_2$ composite electrode were found. In the experiment with laser irradiation of the electrode (see Figure 5.4), the temperature maxima were reached 35 ms or 42 ms after the laser irradiation was stopped, when the cell was filled with water or organic electrolyte solution, respectively. Since these values are in the same order of magnitude, it seems to be realistic that slow heat transfer through the NVP/C electrode causes the delayed temperature maximum after laser irradiation of the electrode.

The starting point of this section was to evaluate which heat source is appropriate to generate the thermal response function of the NVP/C electrode-sensor stack for the deconvolution of the temperature transients. In general, laser irradiation of the electrode is used for this purpose (as it was, e.g., employed for the microcalorimetric measurements with the HC electrodes), since the time interval of the irradiation can be controlled precisely. However, with laser irradiation only the top part of the 99 µm thick NVP/C electrode is heated. In contrast, during charging/discharging of the NVP/C, heat is evolved in the complete volume of the porous composite electrode. Thus, a process, which is temporally confined and whose heat is evolved in the complete volume of the composite electrode is needed. The heat evolved by the electrochemical reduction of Fe^{3+} in 0.1 M $K_3[Fe(CN)_6]/K_4[Fe(CN)_6]$ aqueous electrolyte solution fulfills these requirements. Consequently, 2 ms Fe^{3+} reduction pulses are used to generate the thermal response function of the NVP/C electrode-sensor stack.

5.2.3 Reaction Entropy of Charging/Discharging of NVP/C

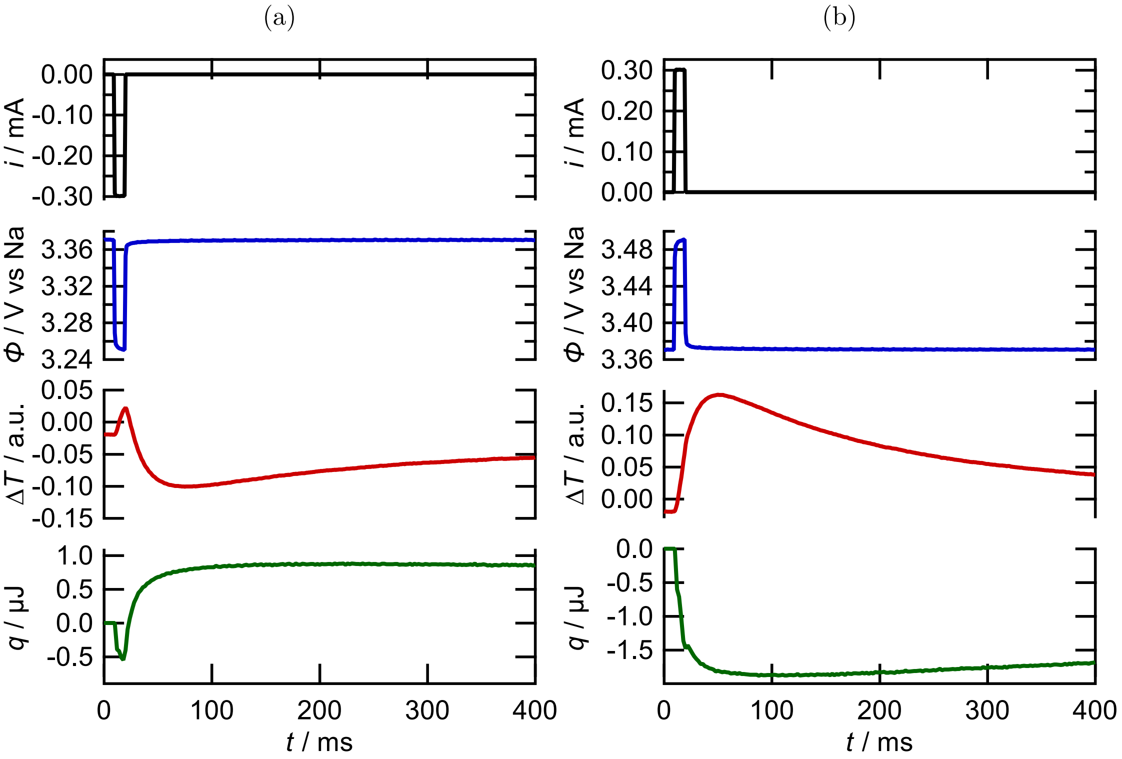

Figure 5.5: Current i, potential ϕ and temperature ΔT transients and the heat q resulting from a 10 ms (a) negative and (b) positive current pulse with an amplitude of ±300 µA of a NVP/C composite electrode at a SoC of 49 % in 1 M $NaPF_6$/EC,PC+FEC.

In Figure 5.5 the exemplary charging/discharging pulses of a NVP/C electrode at a SoC of 49 % in 1 M $NaPF_6$/EC,PC+FEC (shown above in Figure 5.3) are extended by the corresponding heat transients. Note that all transients are shown up to $t = 400$ ms. During the discharging pulse (Figure 5.5 (a)), i.e., from $t = 10$ ms to $t = 20$ ms, the heat is decreasing. For $t > 20$ ms the heat is increasing and is reaching a constant positive value at around $t = 200$ ms. Upon charging (Figure 5.5 (b)), the heat is decreasing during the current pulse as well as after the pulse for $t > 20$ ms. For $t > 200$ ms the heat is still slightly increasing. Such instabilities in the heat evolution over time for $t > 200$ ms were not exclusively found upon charging pulses, but occurred also upon discharging pulses. They might be caused by thermal drift progressively disturbing the measurement. Alternatively, they could also be explained with inaccuracies of the deconvolution of the temperature transients due to the slow heat transfer within the NVP/C composite electrodes. In the following, it is assumed that all processes contributing to the heat are finished for $t = 200$ ms. In consequence, the heat at $t = 200$ ms is used for the determination of the reaction entropy. The temporal behavior of the heat evolution for $t < 200$ ms will be discussed in detail in chapter 5.2.4.

As described in chapter 4.2, the reversibly exchanged molar heat can be obtained

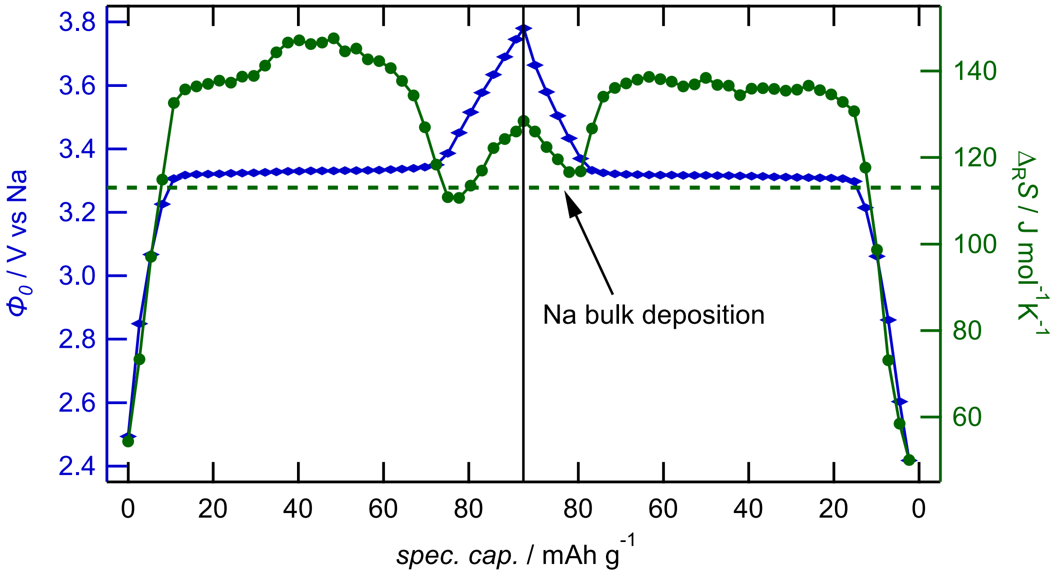

Figure 5.6: Reaction entropy $\Delta_{\mathrm{R}}S$ and equilibrium potential ϕ_0 in the 2nd charging/discharging cycle of NVP/C in 1 M NaPF$_6$/EC,PC+FEC. The reaction entropy of Na metal deposition from the respective electrolyte solution (113 J mol^{-1} K^{-1}) is indicated for comparison with the horizontal dashed line.

by measuring the heat for different and alternating current amplitudes and subsequent interpolation to zero overpotential. Before doing so, the heat values were normalized to the reaction conversion in moles of electrons. Note here, that all values are given in the cathodic direction, which corresponds to discharging of NVP/C. An exemplary interpolation of the molar heat at $t = 200$ ms to zero overpotential for the NVP/C electrode at a SoC of 49 % in 1 M NaPF$_6$/EC,PC+FEC is shown in the appendix in Figure C.5. A reversibly exchanged molar heat of $q_{\mathrm{m,\,rev}} = 43.7$ kJ mol^{-1} was obtained. After correction for the entropy of transport for the respective electrolyte solution (see Table 4.1), this corresponds to a reaction entropy of $\Delta_{\mathrm{R}}S = 137$ J mol^{-1} K^{-1}.

In Figure 5.6 the reaction entropy of the complete 2nd charging and discharging cycle of NVP/C in 1 M NaPF$_6$/EC,PC+FEC is shown together with the equilibrium potential ϕ_0. From 0 mAh g^{-1} to 10 mAh g^{-1} a steep increase of the reaction entropy from 54 J mol^{-1} K^{-1} to 133 J mol^{-1} K^{-1} is observed. In the potential plateau the reaction entropy shows a maximum. At the end of the potential plateau at around 70 mAh g^{-1}, the reaction entropy is suddenly decreasing and a minimum is reached, before the reaction entropy is increasing again. During discharging almost all features of the reaction entropy are found in a reversed order, except the maximum of the reaction entropy in the potential plateau. In the discharging cycle in the potential plateau, the reaction entropy is almost constantly around 135 J mol^{-1} K^{-1}.

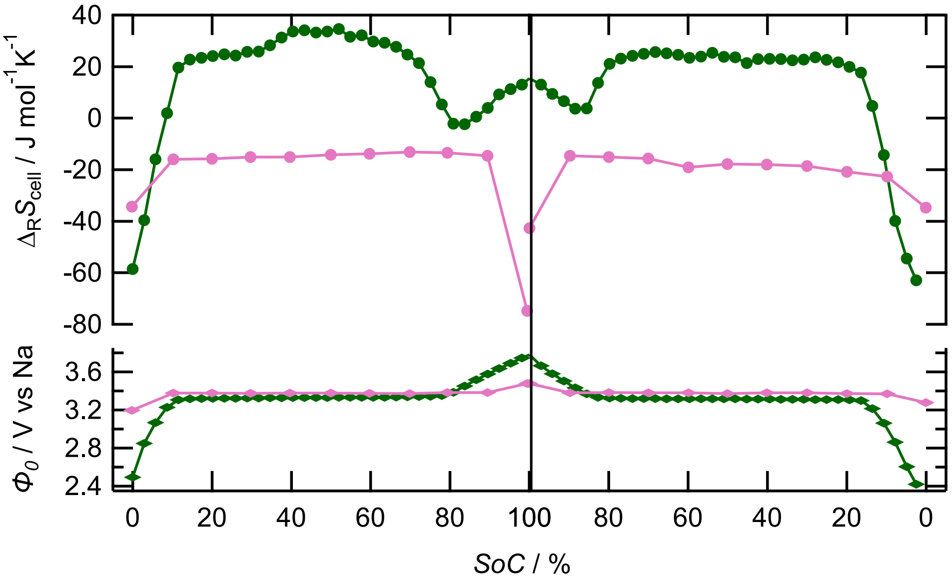

Figure 5.7: Comparison of the reaction entropy and the equilibrium potential of NVP/C in 1 M $NaPF_6$/EC,PC+FEC obtained with microcalorimetry (shown in green) with the cell reaction entropy $\Delta_R S_{cell}$ and the equilibrium cell voltage of NVP/C|Na metal cells determined with entropy profiling by Wei *et al.* (shown in pink).[64] The reaction entropy of NVP/C was shifted by the reaction entropy of Na metal dissolution from the respective electrolyte solution ($-113\,J\,mol^{-1}\,K^{-1}$).

Comparison with the Literature

With entropy profiling Wei *et al.* determined the cell reaction entropy of a NVP/C|Na metal cell with 1 M $NaClO_4$/EC,diethyl carbonate (DEC)+FEC.[64] The results of their study are compared in Figure 5.7 with the microcalorimetric results of this study. For the comparison, the reaction entropy of NVP/C determined with electrochemical microcalorimetry was shifted by the reaction entropy of Na metal dissolution from the respective electrolyte solution ($-113\,J\,mol^{-1}\,K^{-1}$). During charging Wei *et al.* found an almost constant $\Delta_R S_{cell}$ of around $-15\,J\,mol^{-1}\,K^{-1}$ in the potential plateau (between a SoC of 10 % and 90 %). During discharging a slight decrease of the cell reaction entropy in the potential plateau was observed. Next to the potential plateau (at SoCs below 10 % or above 90 %), a reduced cell reaction entropy was observed. At a SoC of 100 % two different cell reaction entropies were reported (one at the end of charging and one at the beginning of discharging), which differ by more than $30\,J\,mol^{-1}\,K^{-1}$. The entropy profiling measurements of Wei *et al.* took more than 10 h at each SoC. In the reported raw cell voltage transients a significant drift of the OCV was observed at a SoC of 100 %. This drift could interfere with the determination of the temperature coefficient of the equilibrium cell voltage. Ultimately, this would explain the different cell reaction entropies found by Wei *et al.* at a SoC of 100 %.

When comparing the results by Wei *et al.* (Figure 5.7, pink) and the microcalorimetric results (green), it can be seen that the absolute values differ by up to

50 J $\mathrm{mol}^{-1}\,\mathrm{K}^{-1}$. A possible reason for the different absolute values might be the difficult calibration of the microcalorimetric experiments with NVP/C as discussed in chapter 3.1.3. The variation of the cell reaction entropy in both studies is somehow similar. A reduced cell reaction entropy is found at low ($< 10\,\%$) and high ($> 90\,\%$) SoCs. At SoCs in the potential plateau, the cell reaction entropy is rather constant. However, Wei *et al.* did not observe a significant difference of the cell reaction entropy between charging and discharging. The differences in the variation of the cell reaction entropy with the SoC could be rooted in the different relaxation times used in the experiments. While the entropy profiling measurements of Wei *et al.* took more than 10 h at each SoC, herein the cell was set to OC conditions for only 40 min before the microcalorimetric pulse measurements were performed. During the relaxation time slow processes, such as the degradation of an intermediate phase, may take place. This could lead to different probed states of the NVP/C electrode in both studies.

Influence of the Electrolyte Solution

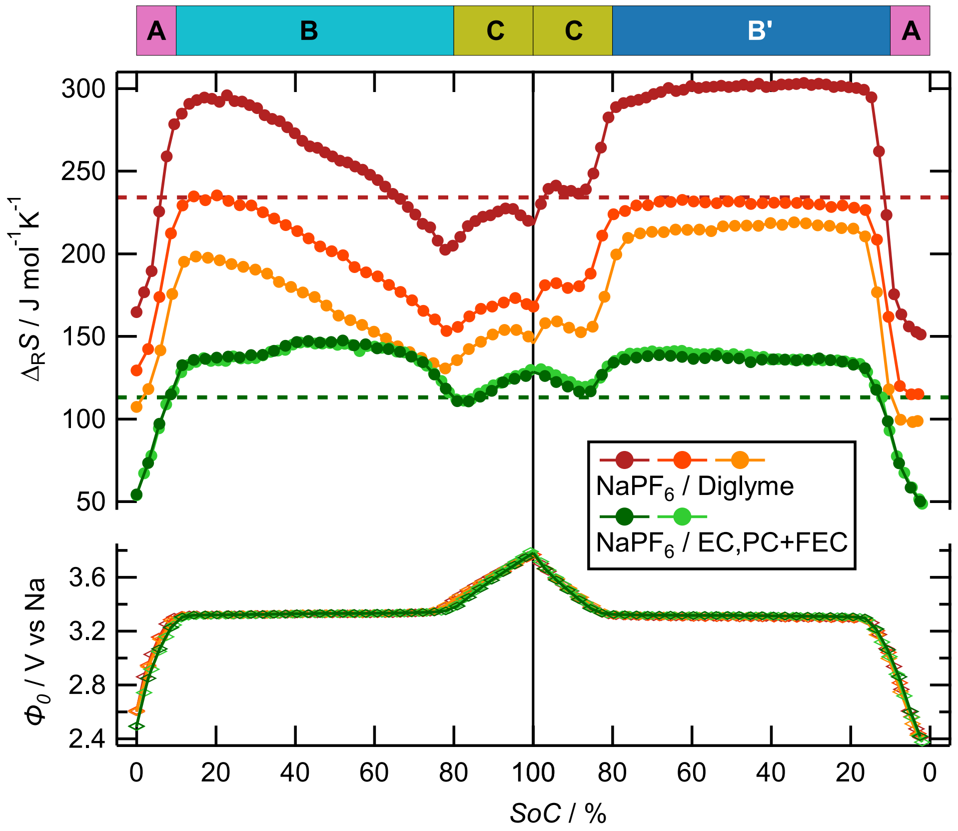

Figure 5.8: Comparison of the reaction entropy $\Delta_\mathrm{R}S$ and ϕ_0 in the charging/discharging cycle of NVP/C in 1 M $\mathrm{NaPF_6}$/diglyme and 1 M $\mathrm{NaPF_6}$/EC,PC+FEC electrolyte solution. The reaction entropies of Na metal deposition from the respective electrolyte solutions are indicated with the horizontal dashed lines. The colored bars indicate the different regions during charging/discharging of NVP/C discussed in the text. For a discussion of the low reproducibility of the experiments with $\mathrm{NaPF_6}$/diglyme see chapter 3.1.3.

To evaluate the influence of the electrolyte solution on the reaction entropy of the charging/discharging of NVP/C, the microcalorimetric experiments were repeated with 1 M $NaPF_6$/diglyme electrolyte solution. The resulting reaction entropy and the equilibrium potential are compared in Figure 5.8 with the results obtained with 1 M $NaPF_6$/EC,PC+FEC. It can be clearly seen that absolute values of the reaction entropy obtained with $NaPF_6$/diglyme were poorly reproducible. This is presumably caused by difficulties of the calibration, as discussed in chapter 3.1.3. Nonetheless, the variation of the reaction entropy with the SoC is rather similar among the three experiments with $NaPF_6$/diglyme electrolyte solution. In general, the reaction entropy of NVP/C is higher in 1 M $NaPF_6$/diglyme than in 1 M $NaPF_6$/EC,PC+FEC. This is expected, since the desolvation entropy in $NaPF_6$/diglyme is larger than in $NaPF_6$/EC,PC+FEC as already discussed for the sodiation of HC.

Following the variation of the reaction entropy and the equilibrium potential with the SoC, the charging and discharging of NVP/C can be separated into four regions (indicated in Figure 5.8 with the colored bars). In region A, ϕ_0 is increasing from 2.5 V to the value of the potential plateau of 3.3 V with increasing SoC. Simultaneously, the reaction entropy is steeply increasing by about $80\,\mathrm{J\,mol^{-1}\,K^{-1}}$ for $NaPF_6$/EC,PC+FEC, and $100\,\mathrm{J\,mol^{-1}\,K^{-1}}$ for $NaPF_6$/diglyme. In the potential plateau during the charging cycle (region B), the reaction entropy is decreasing with increasing SoC for $NaPF_6$/diglyme, but a maximum of the reaction entropy is found for $NaPF_6$/EC,PC+FEC. Between region B and C the reaction entropy has a minimum, before the reaction entropy increases again in region C. In the discharging cycle the behavior is qualitatively reversed in region C and A, but in the potential plateau (region B') the reaction entropy is almost constant for all experiments. In order to understand the variation of the reaction entropy with the SoC, the processes taking place in the different regions will be discussed in the following paragraph.

Discussion

The discharging of NVP/C, i.e., the insertion of Na^+ ion into NVP/C can be generally described with the following equation.

$$\mathrm{Na_xV_2(PO_4)_3 + yNa^+(solv)_n + ye^- \longrightarrow Na_{x+y}V_2(PO_4)_3 + y \cdot n \cdot solv} \tag{5.3}$$

The variable x is defined as the average composition of $\mathrm{Na_xV_2(PO_4)_3}$. The reaction entropy of the reaction 5.3 corresponds to the $\Delta_\mathrm{R}S$ of the insertion of Na^+ ions into NVP/C, which was measured with microcalorimetry. It is determined by two main contributions.

(1) The positive entropy change caused by the desolvation of the Na^+ ions concomitant with the insertion into NVP/C.

(2) The change of the entropy of $\mathrm{Na_xV_2(PO_4)_3}$ due to the insertion of y Na^+ ions, which is $s\Big(\mathrm{Na_{x+y}V_2(PO_4)_3}\Big) - s\Big(\mathrm{Na_xV_2(PO_4)_3}\Big)$.

For the first contribution a positive entropy change of around 151 $\mathrm{J\,mol^{-1}\,K^{-1}}$ for 1 M $NaPF_6$/EC,PC+FEC, and 272 $\mathrm{J\,mol^{-1}\,K^{-1}}$ for 1 M $NaPF_6$/diglyme is expected,[29] when the Na^+ ions are completely desolvated during the insertion into NVP/C. At the beginning of the charging cycle and the end of the discharging cycle (SoCs $< 10\,\%$), a significantly reduced reaction entropy was found (see Figure 5.8). It might be argued, that at SoCs below 10 % the desolvation of the Na^+ ions during the insertion into NVP/C is not completed at $t = 200\,\mathrm{ms}$ (the time at which the heat was used for the calculation of $\Delta_\mathrm{R}S$). However, the microcalorimetric pulse measurements at SoCs below 10 % showed no indication for slow desolvation of the Na^+ ions. The electrode potential was equilibrated already 30 ms after the end of the current pulse and no significant delayed heat exchange was observed for $t > 200\,\mathrm{ms}$. Thus, it is expected that the the desolvation of the Na^+ ions is fast and is completed at $t = 200\,\mathrm{ms}$. This can be corroborated by comparing the reaction entropy of charging/discharging of NVP/C in the two tested electrolyte solutions. Given that the desolvation entropy is almost twice as large for 1 M $NaPF_6$/diglyme compared to 1 M $NaPF_6$/EC,PC+FEC, stronger variations of the reaction entropy would be expected for the same variation of the solvation state of the Na^+ ions with the SoC in $NaPF_6$/diglyme. This was not the case. As described above, the increase of the reaction entropy from 0 % to 10 % SoC was rather similar for both electrolyte solutions (80 $\mathrm{J\,mol^{-1}\,K^{-1}}$ for $NaPF_6$/EC,PC+FEC, 100 $\mathrm{J\,mol^{-1}\,K^{-1}}$ for $NaPF_6$/diglyme). Therefore, it is assumed that the desolvation of the Na^+ ions is completed at $t = 200\,\mathrm{ms}$ at all SoCs. Following this assumption, the contribution of the desolvation of Na^+ ions to the reaction entropy cannot account for the variation of the reaction entropy with the SoC.

The second contribution to the reaction entropy of the insertion of Na^+ ions into NVP/C is the change of the entropy of $Na_xV_2(PO_4)_3$ due to the change of its composition. This contribution can vary with the SoC and might give insights into the processes taking place in the NVP/C material. For instance, a different variation of the reaction entropy with the SoC is expected when one phase or two phases are existing in the active material.[113] When one phase is existing, the charging/discharging could be described with a solid solution model (see chapter 4.4.1). When two phases are coexisting, charging causes one phase to grow while the other shrinks, and discharging reverses the process. To understand how such a process is reflected in the reaction entropy, the general variation of the entropy of a material during a first-order phase transition is presented first. The description is based on the work by McKinnon *et al.*,[114] and Huang *et al.*[63] During a first-order phase transition two phases α and β coexist in the so-called miscibility gap, which ranges between the average composition $x = x_1$ and $x = x_2$. The entropy change in the miscibility gap ΔS_MG can be calculated with the molar entropy $s_\alpha(x_1)$ of the phase

α at $x = x_1$, and the molar entropy $s_\beta(x_2)$ of the phase β at $x = x_2$.[63, 114]

$$\Delta S_{\mathrm{MG}} = \left(\frac{\partial s}{\partial x}\right)_T = \frac{s_\alpha(x_1) - s_\beta(x_2)}{x_1 - x_2} \tag{5.4}$$

This means that ΔS_{MG} is constant within the miscibility gap. Unfortunately, the molar entropy of $Na_3V_2(PO_4)_3$ or $Na_1V_2(PO_4)_3$ was not found in the literature. Thus, the variation of the reaction entropy with the SoC can only qualitatively be discussed. With increasing SoC (i.e., decreasing x in $Na_xV_2(PO_4)_3$) a constant reaction entropy is expected, when a first-order phase transition takes place within a two-phase region. In contrast, an increasing reaction entropy is expected with increasing SoC for a solid solution-type process (see chapter 4.4.1).

In region A, i.e., at SoCs below 10 %, the equilibrium potential and the reaction entropy is increasing with increasing SoC (see Figure 5.8). This indicates that at these SoCs only one phase may exist and a solid solution-type process might take place. This is in accordance with the XRD measurements of Park *et al.*, who found only $Na_3V_2(PO_4)_3$ in this region.[9]

In region B the equilibrium potential does not change with the SoC indicating a two-phase regime, i.e., a miscibility gap. As described in chapter 5.1, the potential plateau during charging/discharging of NVP is in general explained with a first-order phase transition from $Na_3V_2(PO_4)_3$ to $Na_1V_2(PO_4)_3$. However, the reaction entropy is changing with the SoC in region B, which is not expected for the entropy change of NVP/C within a two-phase region of a first-order phase transition (see equation 5.4). With *operando* XRD Park *et al.* found that in this region during charging an intermediate phase $Na_2V_2(PO_4)_3$ is appearing.[9] They proposed that in region B an out-of-equilibrium "three-phase" reaction takes place. Such a reaction could be understood as an overlap of two two-phase reactions ($Na_3V_2(PO_4)_3$ to $Na_2V_2(PO_4)_3$, and $Na_2V_2(PO_4)_3$ to $Na_1V_2(PO_4)_3$). In the case of a stable intermediate phase, two distinct plateaus would be expected in the reaction entropy.[113] This could not clearly be observed in the measured reaction entropy in 1 M $NaPF_6$/EC,PC+FEC electrolyte solution. This may be due to the instability of the intermediate phase $Na_2V_2(PO_4)_3$, which was only observed under non-equilibrium conditions (i.e. charging/discharging).[9] In addition, it should be noted that the variation of the reaction entropy in region B was different for the two electrolyte solutions.

In region C the equilibrium potential as well as the reaction entropy is increasing during charging and decreasing during discharging. This is similar to region A, but the increase/decrease of the reaction entropy is less pronounced in region C compared to region A. Still, the variation of the entropy in region C indicates as well a solid solution-type process. In region C, XRD measurements showed that mainly $Na_1V_2(PO_4)_3$ is present.[9] It is expected that in this region charging occurs through homogeneous filling of the particle with Na^+ ions.[115]

In region B', i.e., in the potential plateau during discharging, the reaction entropy is almost constant. A constant reaction entropy could indicate a two-phase regime. Indeed, Park *et al.* found with *operando* XRD that a two-phase reaction between $Na_1V_2(PO_4)_3$ and $Na_2V_2(PO_4)_3$ takes place in the potential plateau during discharging.[9] At the end of the potential plateau, i.e., just before the potential is decreasing, they found a rapid transition from $Na_2V_2(PO_4)_3$ to $Na_3V_2(PO_4)_3$.

In conclusion, the reaction entropy of the insertion of Na^+ ions into NVP/C revealed an asymmetry between the charging and the discharging process of NVP/C, which is in accordance with *operando* XRD measurements by Park *et al.*[9] In particular, the almost constant reaction entropy in the potential plateau during discharging indicated a two-phase reaction, while in the potential plateau during charging a more complex mechanism, involving an intermediate phase, is expected.

5.2.4 Temporal Behavior of the Heat Evolution Upon Charging/Discharging of NVP/C

It was already touched upon that the temporal behavior of the heat evolution upon short charging/discharging pulses of NVP/C is of further interest, as it contains information about the ongoing processes during and after the current pulses. In Figure 5.9 the current, potential, temperature and heat transients resulting from 10 ms positive and negative current pulses with different current amplitudes of NVP/C in 1 M $NaPF_6$/EC,PC+FEC are shown for a SoC of 49 % ((a) and (b)) and 0 % ((c) and (d)). Independent of the pulse polarity and the SoC, heating takes place during the current pulses from $t = 10\,\mathrm{ms}$ to $20\,\mathrm{ms}$. The heating is more pronounced for the higher current amplitudes, i.e., a higher overpotential leads to more heating during the pulse. For $t > 20\,\mathrm{ms}$ the heat evolutions differ for the different pulse polarities and SoCs (cf. Figure 5.9). Nevertheless, all heat transients are approaching a rather constant value for $t = 200\,\mathrm{ms}$ and no significant heat exchange was observed for $t > 200\,\mathrm{ms}$. Consequently, it was assumed that the charging/discharging of NVP/C with the short current pulses is completed at $t = 200\,\mathrm{ms}$, as discussed in chapter 5.2.3.

The potential responses upon the short current pulses with different pulse amplitudes differ solely by a sign reversal. This indicates that the charging/discharging of NVP/C with short current pulses is a reversible process. In addition, the amount of the pulse charge was the same for the positive and the negative current pulse. Thus, it can be assumed that the charging/discharging process is equally advanced at all points of time. This allows to separate the heat at different points of time into a reversible and an irreversible contribution. Since the reversibly exchanged heat q_{rev} changes its sign upon changing the pulse polarity and the irreversibly exchanged heat q_{irrev} does not, the contributions can be calculated with the heat upon a cathodic pulse q_{cat} and an anodic pulse q_{an} as follows.

$$q_{\mathrm{rev}} = \frac{q_{\mathrm{cat}} - q_{\mathrm{an}}}{2} \tag{5.5}$$

$$q_{\mathrm{irrev}} = \frac{q_{\mathrm{cat}} + q_{\mathrm{an}}}{2} \tag{5.6}$$

The resulting values with the heat measured at $t = 20\,\mathrm{ms}$ and $t = 200\,\mathrm{ms}$ are shown in Table 5.2. Additionally, the polarization heat q_{pol} was calculated with the mean overpotential η during the pulse and the pulse charge dQ.

$$|\delta q_{\mathrm{pol}}| = -zF|\eta|d\xi = -|\eta dQ| \tag{5.7}$$

It should be noted that the polarization heat might be overestimated, as the mean overpotential also contains contributions of the iR-drop through the electrolyte solution.

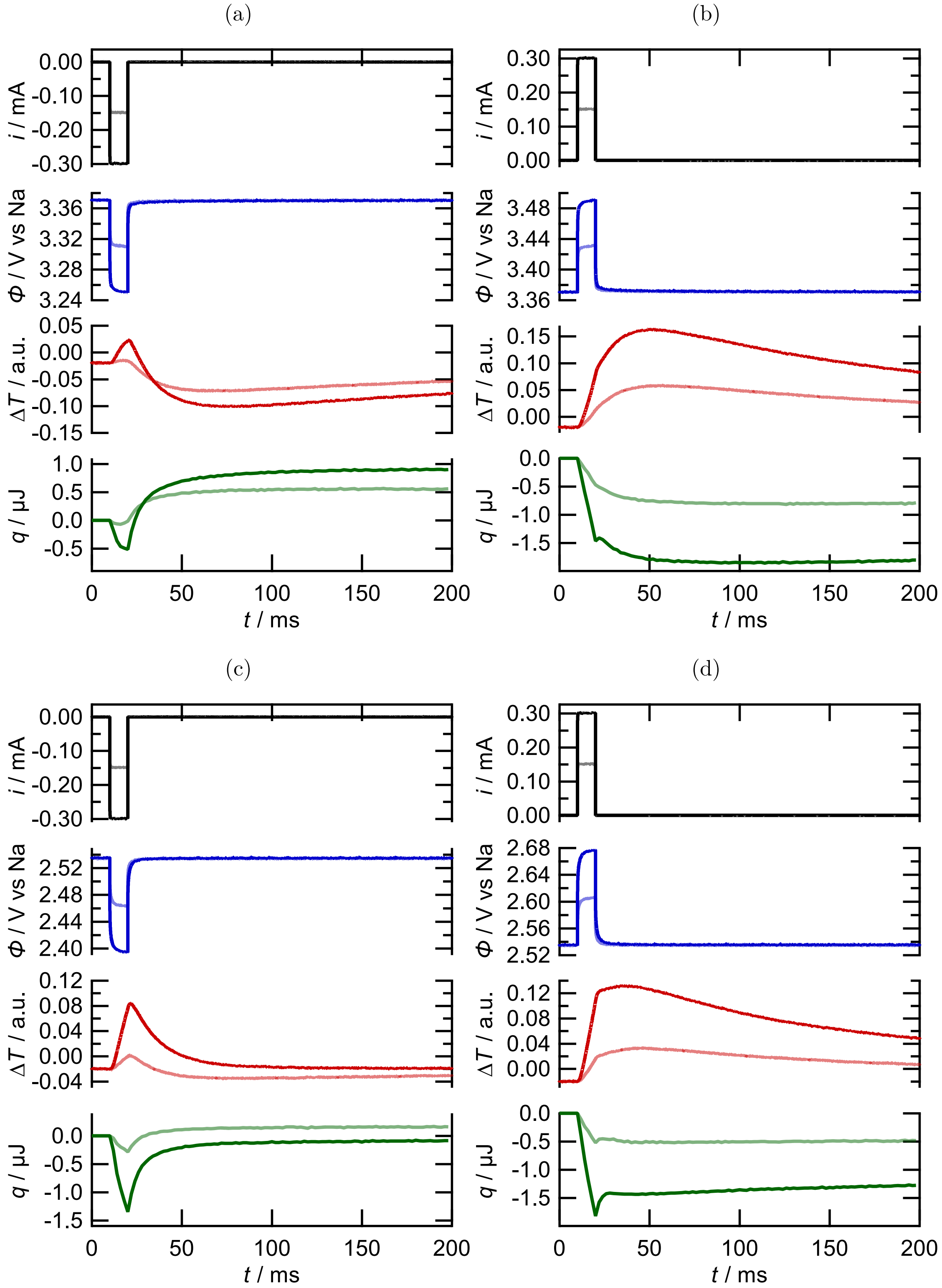
(a)

(b)

(c)

(d)

Figure 5.9: Current i, potential ϕ and temperature ΔT transients and the heat q resulting from 10 ms negative and positive current pulses with an amplitude of ±150 µA (light colors) and ±300 µA (dark colors) of a NVP/C composite electrode in 1 M $NaPF_6$/EC,PC+FEC at a SoC of (a),(b) 49 % and (c),(d) 0 %.

	$q_{\mathrm{rev}}(20\,\mathrm{ms})$	$q_{\mathrm{rev}}(200\,\mathrm{ms})$	$q_{\mathrm{irrev}}(20\,\mathrm{ms})$	$q_{\mathrm{irrev}}(200\,\mathrm{ms})$	q_{pol}
SoC 49 %	0.48	1.35	-0.99	-0.45	-0.35
SoC 0 %	0.24	0.60	-1.59	-0.68	-0.40

Table 5.2: Reversibly exchanged heat q_{rev} and irreversibly exchanged heat q_{irrev} determined with the heat measured at $t = 20\,\mathrm{ms}$ and $t = 200\,\mathrm{ms}$ after 10 ms current pulses (±300 µA, cf. Figure 5.9). The polarization heat q_{pol} was calculated according to equation 5.7. All values are given in µJ.

The reversibly exchanged heat q_{rev} increases with increasing time. With q_{rev} at $t = 200\,\mathrm{ms}$, i.e., when the charging/discharging process is assumed to be complete, the reaction entropy can be calculated. An $\Delta_{\mathrm{R}}S$ of $136\,\mathrm{J\,mol^{-1}\,K^{-1}}$ and $55\,\mathrm{J\,mol^{-1}\,K^{-1}}$ was determined at a SoC of 49 % and 0 %, respectively. This in accordance with the reaction entropy shown above in Figure 5.6.

The value of the irreversibly exchanged heat q_{irrev} at $t = 20\,\mathrm{ms}$ is significantly lower than the calculated polarization heat at both SoCs. In other words, up to $t = 20\,\mathrm{ms}$ more heating was observed, than it is expected from polarization heat. From $t = 20\,\mathrm{ms}$ to $t = 200\,\mathrm{ms}$ q_{irrev} increases, i.e., independent of the pulse polarity a process, which leads to cooling, takes place for $t > 20\,\mathrm{ms}$. In consequence, q_{irrev} is approaching the calculated q_{pol} at $t = 200\,\mathrm{ms}$.

In summary, independent of the pulse polarity, additional heating was observed during the current pulse up to $t = 20\,\mathrm{ms}$ beside the polarization heat and the reversible heat. This additional heat was almost completely "compensated" by a cooling process after the current pulse from $t = 20\,\mathrm{ms}$ to $t = 200\,\mathrm{ms}$. Hence, there must be a process, which leads to heating during current flow and cooling during the relaxation phase regardless of whether a charging or a discharging pulse was applied. Such a behavior is rather unusual, since irreversible processes in general lead to heating. The process, which was observed here after the current pulse, leads to irreversible cooling.

During the current pulse, concentration gradients of, e.g., $\mathrm{Na^+}$ ions in the electrolyte solution or in the NVP/C particles, could arise. When the current flow is interrupted, these concentration gradients equalize. Thomas and Newman found that these processes can be accompanied by the exchange of heat.[116, 117] They wrote that "heat is exchanged during formation of concentration gradients as current is passed, and an equal and opposite amount of heat is exchanged upon relaxation of those gradients", and termed this heat the heat of mixing.[116] They derived that the sign of the heat of mixing depends on the change of the partial molar enthalpy with its concentration $\frac{\partial \overline{H}}{\partial c}$. When $\frac{\partial \overline{H}}{\partial c}$ is positive, the relaxation of the concentration gradient is an exothermic process.[116] Further, Thomas and Newman named four types of concentration gradients, which can occur in electrochemical cells with porous insertion electrodes.

Concentration gradients

(1) across the electrolyte solution due to mass transfer,

(2) radially within the pores filled with electrolyte solution,

(3) radially within the particles of insertion material,

(4) or across the insertion electrode due to nonuniform current distribution.

In the following these different concentration gradients and their possible influence on the heat of mixing will be qualitatively discussed for the herein investigated charging/discharging of NVP/C with short current pulses.

(1) The amount of Na^+ ions inserted/extracted from the NVP/C electrode due to the short charging/discharging pulses can be estimated. A 10 ms pulse with a current amplitude of 300 µA has a pulse charge of 3.0 µC. This corresponds to 3.1×10^{-11} mol Na^+ ions, when it is assumed that per electron one Na^+ ion is inserted into or extracted from the NVP/C electrode. In the 1 M electrolyte solution this amount of Na^+ ions is found in 3.1×10^{-11} l. Such a volume corresponds to a cylinder with the electrode area 0.2 cm^2 and a height of about 1.6 nm. Simply put, there are enough Na^+ ions within a distance of 1.6 nm above the electrode in the electrolyte solution to account for the pulse charge. Since mass transport on such length scales should be fast, considerable concentration gradients across the electrolyte solution are not expected and ultimately this component of heat of mixing should be small.

(2) According to Thomas and Newman concentration gradients radially within the pores filled with electrolyte solution are very small in practical systems, so that this component of heat of mixing is negligible.[116, 117]

(3) Concentration gradients radially within the particles of the insertion material arise when particles sizes are large, high charging rates are used or the solid diffusivity is low within the particles.[116] The diameter of the particles of the herein investigated NVP/C was around 12.2 µm. A current pulse amplitude of 300 µA corresponded to a 1.7 C rate. Thus, concentration gradients of Na^+ ions within the NVP/C particles may arise during the current pulses.

(4) A nonuniform current distribution across the composite electrode can lead to concentration gradients across the porous electrode. Such a nonuniformity of the current is promoted by high charging rates and small variations of the equilibrium potential of the electrode with its SoC. The NVP/C electrode potential is constant between 10 % and 80 % SoC (cf. the potential plateau, e.g., in Figure 5.6). Therefore, the NVP/C particles within the composite electrode might be charged/discharged to a different degree during the short current pulses.

In conclusion, charging/discharging of NVP/C with short current pulses could lead to considerable concentration gradients within the particles (3) or across the composite electrode (4). The resulting heat of mixing from such concentration gradients depends on the variation of the enthalpy potential with the SoC.[116] For NVP/C this variation is presumably small, since the equilibrium potential (corresponding to $\Delta_\mathrm{R}G$) is almost constant from 10 % to 80 % SoC. The variations of the reaction entropy $\Delta_\mathrm{R}S$ found for 1 M $NaPF_6$/EC,PC+FEC in this SoC region are also rather small compared to $\Delta_\mathrm{R}G$. Thus, it remains unclear how large the contribution of the heat of mixing could be for the charging/discharging of NVP/C. In addition, the sign of this contribution, i.e., whether heating or cooling is expected during relaxation of the concentration gradients, could not be predicted.

Thomas and Newman found that for typical LIB negative electrode materials, the relaxation of the concentration gradients are exothermic processes, which is contradiction to the experimentally observed behavior upon charging/discharging of NVP/C with short current pulses. However, in more recent simulations of heat generation within LIBs, additional heating was observed during the charging when the heat of mixing was considered.[118, 119] This should lead to cooling during the relaxation of the concentration gradients. Finally, a definitive explanation for the unusual temporal behavior of the heat evolution upon short charging/discharging pulses of NVP/C could not be found. A possible cause might be the heat of mixing due the formation and relaxation of concentration gradients of Na^+ ions within the NVP/C particles or across the composite electrode.

5.3 Entropy Profiling of NVP/C|HC Cells

It was already mentioned that a SIB reference system was established within the POLiS Cluster of Excellence.[40] The final SIB cell consisted of HC as negative electrode material, NVP/C as positive electrode material and 1 M $NaPF_6$/EC,PC as electrolyte solution. In a round robin study, NVP/C|HC coin cells were build from these materials at different research institutes to test the repeatability and reproducibility. In the following, entropy profiling experiments of such coin cells are presented. The variation of the equilibrium cell voltage caused by fast temperature steps was determined in the same way as it was done for the HC|Na metal cells in chapter 4.3.

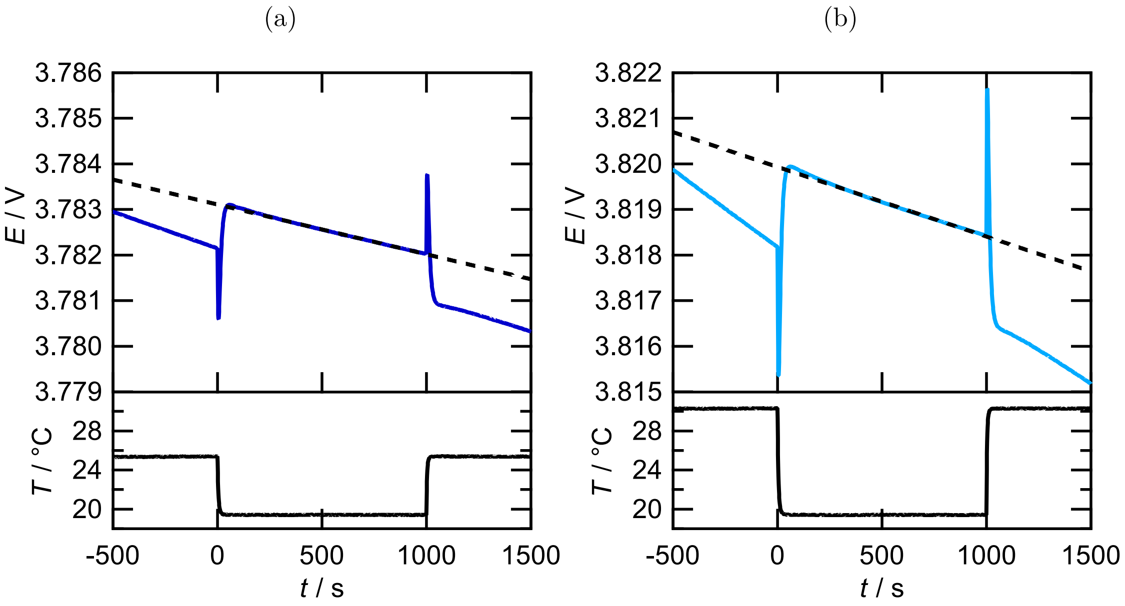

Figure 5.10: Cell voltage transients of a NVP/C|HC cell with 1 M $NaPF_6$/EC,PC at OC conditions at a SoC of 100 % caused by the shown temperature steps of (a) $\Delta T = -5.9\,\mathrm{K}$ and (b) $\Delta T = -10.9\,\mathrm{K}$. The black dashed lines indicate the cell voltage drift at the lower temperature (linear fit from $t = 200\,\mathrm{s}$ to $t = 1000\,\mathrm{s}$).

The NVP/C|HC coin cells used for these experiments were prepared by Salimeh Saleh at the University of Ulm. For the round robin study the cells were charged/ discharged 1000 times between 2.3 V and 3.9 V. During the cycling the specific capacity decreased from initially around 65 mAh g^{-1} to below 25 mAh g^{-1}. This means that degradation of the cells took already place, before they were investigated with entropy profiling.

For the entropy profiling, the charging/discharging of the NVP/C|HC cells (±30 µA) was interrupted periodically by OC phases in the same way as it was done for the HC|Na metal cells (see Figure 4.12). During the OC phases the temperature of the cell was changed in a stepwise manner. Two exemplary cell voltage transients of a NVP/C|HC cell at a SoC of 100 % caused by temperature steps with different heights are shown in Figure 5.10. In both cases a negative spike of the cell voltage occurred immediately after the temperature was switched ($t < 10\,\mathrm{s}$). For $t > 100\,\mathrm{s}$ these deteriorations leveled off and a linear regime of the cell voltage was reached. When the temperature was switched back, the reversed behavior of the cell voltage was observed. Throughout the complete depicted time interval in Figure 5.10 the OCV is drifting toward lower cell voltages. The slope of the OCV drift is smaller at the lower temperature compared to the higher temperature.

The characteristics of the cell voltage transients upon fast temperature steps were discussed in detail for HC|Na metal cells in chapter 4.4.3. The sharp negative voltage spike after switching the temperature of the cell was attributed to temperature gradients across the coin cell and the temperature sensitivity of the electrode potentials. Since the NVP/C|HC coin cells were constructed in the same way as the HC|Na metal cells, it stands to reason that the negative voltage spikes observed for the NVP/C|HC cells are also caused by temperature gradients across the coin cell. The influence of the baseline drift of the OCV on the cell voltage variation due to the temperature change was corrected by extrapolating the cell voltage at the lower temperature to $t = 0\,\mathrm{s}$. For this purpose a linear fit between $t = 200\,\mathrm{s}$ and $t = 1000\,\mathrm{s}$ was used (indicated with the black dashed lines in Figure 5.10). The difference between the linear fit and the measured cell voltage at $t = 0\,\mathrm{s}$ was used for the determination of the cell reaction entropy. For the examples shown in Figure 5.10 this resulted in a $\Delta_\mathrm{R}S_\mathrm{cell}$ of $-15.6\,\mathrm{J\,mol^{-1}\,K^{-1}}$ in both cases.

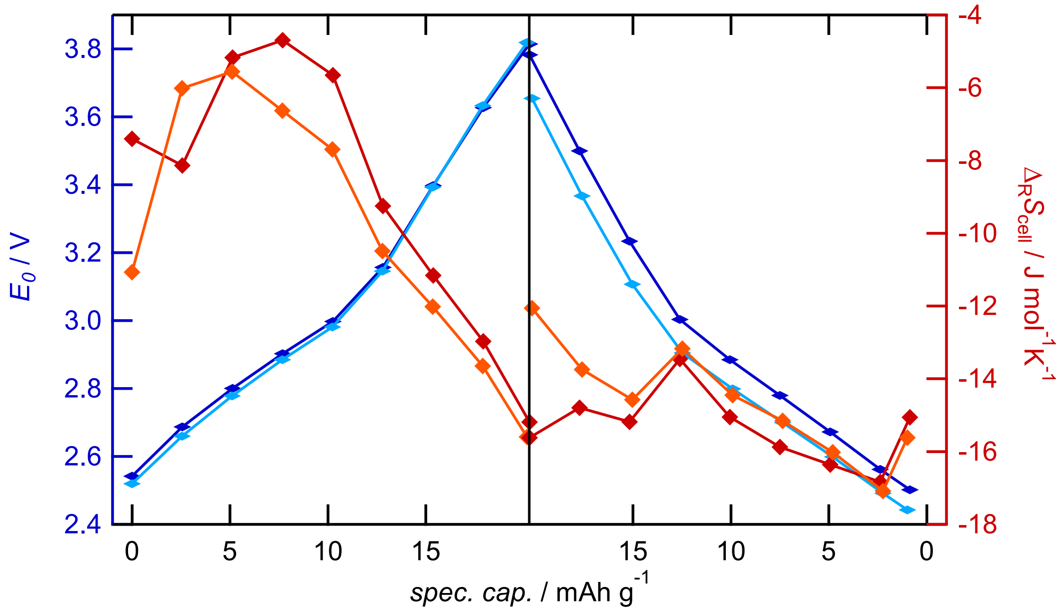

Figure 5.11: Cell reaction entropy and the equilibrium cell voltage E_0 of a NVP/C|HC coin cell with 1 M NaPF$_6$/EC,PC in the charging and the discharging cycle. The data was obtained in two consecutive cycles with a temperature step height of $\Delta T = -5.9\,\mathrm{K}$ (red) and $\Delta T = -10.9\,\mathrm{K}$ (orange).

The cell reaction entropy and the equilibrium cell voltage of a NVP/C|HC coin cell with 1 M $NaPF_6$/EC,PC in the charging and the discharging cycle is shown in Figure 5.11 for two consecutive cycles. A temperature step height of $\Delta T = -5.9\,\mathrm{K}$ (red) and $\Delta T = -10.9\,\mathrm{K}$ (orange) was used. Within the cell voltage limit of 2.3 V and 3.9 V the coin cell showed a specific capacity of around $20\,\mathrm{mAh\,g^{-1}}$. Note here that the equilibrium cell voltage, obtained ca. 6000 s after the charging/discharging was interrupted, ranges only between 2.5 V and 3.8 V, due to the relaxation of the cell voltage in the OC phase. With increasing/decreasing SoC the equilibrium cell voltage in-/decreased. A cell voltage plateau was not observed. The cell voltage profile of NVP/C|HC cells normally shows such a plateau.[40] The missing cell voltage plateau in Figure 5.11 is presumably a result of the degradation of the NVP/C|HC coin cell, which were already charged/discharged 1000 times.

The obtained cell reaction entropy of the NVP/C|HC is negative and varies between $-4\,\mathrm{J\,mol^{-1}\,K^{-1}}$ and $-18\,\mathrm{J\,mol^{-1}\,K^{-1}}$. In the charging cycle $\Delta_R S_{cell}$ has a maximum before it decreases to around $-16\,\mathrm{J\,mol^{-1}\,K^{-1}}$. In the discharging cycle the cell reaction entropy is rather constant at values between $-12\,\mathrm{J\,mol^{-1}\,K^{-1}}$ and $-18\,\mathrm{J\,mol^{-1}\,K^{-1}}$. The results obtained in two consecutive cycles with different temperature step heights are rather similar. The reproducibility of the entropy profiling with NVP/C|HC cells was examined by repeating the experiment with a total of four coin cells. In Figure C.6 the resulting $\Delta_R S_{cell}$ is shown dependent on the equilibrium cell voltage. Despite one coin cell, the same variation of $\Delta_R S_{cell}$ (maximum in the charging cycle, rather constant in the discharging cycle) was found for the different cells.

There are two aspects that will be discussed the following: (I) the absolute value of $\Delta_R S_{cell}$, and (II) the variation of $\Delta_R S_{cell}$ with the SoC. With the sign convention applied in this work, a negative $\Delta_R S_{cell}$ corresponds to an entropy decrease during discharging. Thus, the reversible heat contribution should lead to heating during discharging and cooling during charging. This is in accordance with calorimetric measurements of NVP/C|HC cells by Mohsin *et al.*,[105] who found less total heat generation during charging compared to discharging. The cell reaction entropy of the NVP/C|HC coin cell consists of the contribution of the HC and the NVP/C electrode, i.e., $\Delta_R S_{cell} = \Delta_R S_{NVP/C} - \Delta_R S_{HC}$. Consequently, in the herein investigated NVP/C|HC cell, $\Delta_R S_{HC}$ is larger than $\Delta_R S_{NVP/C}$. With microcalorimetry a reaction entropy of around $128\,\mathrm{J\,mol^{-1}\,K^{-1}}$ for HC (cf. Figure 4.9) and $137\,\mathrm{J\,mol^{-1}\,K^{-1}}$ for NVP/C (cf. Figure 5.6) was found in 1 M $NaPF_6$/EC,PC at a SoC of 50 %. This is in contradiction with the negative $\Delta_R S_{cell}$ of the NVP/C|HC cell determined with entropy profiling. It could be explained with deviations of the absolute values of $\Delta_R S_{NVP/C}$ due to difficulties in the calibration of the microcalorimetric experiments with the NVP/C electrodes (see chapter 3.1.3).

For the discussion of the variation of $\Delta_R S_{cell}$ with the SoC, it has to be noted that in the 2-electrode NVP/C|HC coin cell no RE was included. Thus, the electrode potentials and the SoCs of the HC and the NVP/C electrode could not be determined. The variation of $\Delta_\mathrm{R}S_\mathrm{cell}$ with the SoC differed between the charging and the discharging cycle. Such an asymmetry between the charging and the discharging cycle was only observed for the reaction entropy of NVP/C and not for the reaction entropy of HC (determined with electrochemical microcalorimetry). Therefore, the variation of $\Delta_\mathrm{R}S_\mathrm{cell}$ of the NVP/C|HC cell with the SoC is ascribed to the reaction entropy of the NVP/C electrode.

In conclusion, the cell reaction entropy of NVP/C|HC cells is negative and varies differently with the SoC during the charging and the discharging cycle. The negative $\Delta_\mathrm{R}S_\mathrm{cell}$ can be explained with $\Delta_\mathrm{R}S_\mathrm{HC}$ being larger than $\Delta_\mathrm{R}S_\mathrm{NVP/C}$. The differences in the variation of $\Delta_\mathrm{R}S_\mathrm{cell}$ between the charging and the discharging cycle are ascribed to the reaction entropy of the NVP/C electrode, in accordance with the microcalorimetric results of the reaction entropy of NVP/C.

5.4 Conclusions

The reaction entropy of the charging/discharging of NVP/C consists of the solvation/desolvation of the $\mathrm{Na^+}$ ions and the entropy change of the NVP/C. While the first contribution is independent of the SoC, the second one is presumably causing the measured variation of the reaction entropy of the charging/discharging of NVP/C with the SoC. A different variation of $\Delta_\mathrm{R}S_\mathrm{NVP/C}$ with the SoC was found in the charging cycle compared to the discharging cycle. The rather constant reaction entropy found in the potential plateau (10 % to 80 % SoC) during discharging could be attributed to a two-phase reaction. At identical SoCs during charging, $\Delta_\mathrm{R}S_\mathrm{NVP/C}$ was varying with the SoC, which might be related to an intermediate phase $\mathrm{Na_2V_2(PO_4)_3}$ as found by Park *et al.*[9] At SoCs below 10 % and above 80 %, the variation of the reaction entropy with the SoC indicated the existence of a single phase in each case, which might be sodiated/desodiated *via* a solid solution-type process.

The heat exchange upon the short charging/discharging pulses of NVP/C used for the microcalorimetric measurements was not only caused by contributions of the entropy change and the polarization. An additional process leading to heating during external current flow and to cooling when when the cell was set to OC conditions was observed independent of the pulse polarity. It could possibly caused by the formation and relaxation of concentration gradients of $\mathrm{Na^+}$ ions within the NVP/C particles or across the NVP/C composite electrode.

6

Conclusions

The aim of this work was to improve the understanding of the charging/discharging processes in SIBs by measuring the concomitant entropy changes. The reaction entropy of charging/discharging of HC and NVP/C at varying SoC was determined with two distinct methods covering different timescales. With electrochemical microcalorimetry the entropy production could be resolved with millisecond time resolution, but only processes which were completed within less than a second were captured. Entropy profiling, i.e., measuring the temperature dependence of the equilibrium cell voltage, yielded the cell reaction entropy, which also contained contributions of slow relaxation processes.

For both, the sodiation of HC and the insertion of Na^+ ions into NVP/C, the increase of the entropy caused by the concomitant desolvation of the Na^+ ions dominated the reaction entropy and led to a positive reaction entropy of the processes at the single electrode. Therefore, the reaction entropy was highly dependent on the electrolyte solution. For instance, reaction entropies of up to $250\,\mathrm{J\,mol^{-1}\,K^{-1}}$ and $90\,\mathrm{J\,mol^{-1}\,K^{-1}}$ were found for HC or NVP/C in $1\,\mathrm{M}$ $NaPF_6$/diglyme and $1\,\mathrm{M}$ $NaClO_4$/PC, respectively. The second contribution to the reaction entropy of charging/discharging HC or NVP/C was the entropy change of the active material due to the insertion/extraction of Na^+ ions. This contribution varied with the SoC of the composite electrodes and gave insights into the respective charging mechanism. For the sodiation/desodiation of HC, the variation of the reaction entropy with the SoC was attributed to the variation of the entropy of the Na species in the HC. It could be explained with an extended solid solution model based on the work by Mercer *et al.*[61] In particular, the variation of the sodiation entropy with the SoC speaks in favor of an adsorption-intercalation-pore filling model. In this model, with increasing SoC, Na^+ ion storage at defect sites is followed by intercalation of Na^+ ions into the graphitic layers. At SoCs above 50 %, the pores are subsequently filled with sodium. Statements about the kinetics of the sodiation of HC were possible by comparing the sodiation entropy of HC obtained with electrochemical microcalorimetry and entropy profiling, i.e., including contributions of processes completed within 0.4 s or 300 s, respectively. At SoCs below 20 %, a significantly reduced reaction entropy was found with microcalorimetry compared to entropy profiling. This could be explained with incomplete desolvation of the Na^+ ions during a fast capacitive adsorption process. This fast process was followed by a slow equilibration process leading to complete desolvation of the Na^+ ions within 300 s.

Consequently, a permanent co-intercalation of Na^+ ions and solvent molecules into HC was excluded. At SoCs above 20 %, the sodiation of HC exhibited faster kinetics, leading to complete desolvation of the Na^+ ions within 0.4 s. The SoC-dependent sodiation kinetics of HC were also reflected in the cell voltage response caused by the temperature steps used for the entropy profiling experiments. At SoCs below 10 % the sluggish sodiation kinetics of HC led to a slow equilibration of the HC electrode potential and ultimately to a slow relaxation of the cell voltage after the temperature step. In addition to the entropy measurements of the sodiation of HC, XPS was used to investigate the composition and the stability of the SEI on the HC electrode in the 6th charging cycle. It was found, that the thickness of the SEI is increasing with increasing SoC. However, this did not significantly influence the reaction entropy obtained with electrochemical microcalorimetry.

For charging/discharging NVP/C, the variation of the reaction entropy with the SoC was larger than for the sodiation/desodiation of HC. At SoCs below 10 %, a steep increase of the reaction entropy with increasing SoC indicated that the charging/discharging mechanism could be described by a solid solution-type depletion/filling of the single phase $Na_3V_2(PO_4)_3$. A similar mechanism is expected at SoCs above 80 %, with the present phase being $Na_1V_2(PO_4)_3$. The rather constant reaction entropy in the potential plateau (10 % to 80 % SoC) in the discharging cycle could be explained with a first-order phase transition within a two-phase regime, i.e., charging/discharging occurs through growth of one phase and shrinking of the other phase. However, in the charging cycle at identical SoCs, the reaction entropy was varying with the SoC, which could possibly be explained with the occurrence of an intermediate phase $Na_2V_2(PO_4)_3$ as found in *operando* XRD experiments by Park *et al.*[9] The cell reaction entropy of a NVP/C|HC coin cell determined with entropy profiling corroborated the entropy measurements of the single electrodes. The different variation of the cell reaction entropy, found in the charging cycle compared to the discharging cycle, was ascribed to the different mechanism during charging and discharging of NVP/C.

In this work, it was shown that time-resolved measurements of the entropy production can improve the understanding of charging/discharging processes in SIBs. The greatest potential for future studies is expected to be the ability of electrochemical microcalorimetry to identify not only electrochemical, but also chemical processes at the electrode-electrolyte interface. This allows, e.g., to obtain further information about desolvation processes of metal ions crucial for the improvement of the electrode's performance.

A

References

[1] M. L. Machala, X. Chen, S. P. Bunke, G. Forbes, A. Yegizbay, J. A. de Chalendar, I. L. Azevedo, S. Benson, W. A. Tarpeh, "Life cycle comparison of industrial-scale lithium-ion battery recycling and mining supply chains", *Nature Communications* **2025**, *16*, 988.

[2] A. Yao, S. M. Benson, W. C. Chueh, "Critically assessing sodium-ion technology roadmaps and scenarios for techno-economic competitiveness against lithium-ion batteries", *Nature Energy* **2025**, *10*, 404–416.

[3] J. Mitali, S. Dhinakaran, A. A. Mohamad, "Energy storage systems: a review", *Energy Storage and Saving* **2022**, *1*, 166–216.

[4] *Sodium-ion batteries: Materials, characterization, and technology*, First edition, (Eds.: M.-M. Titirici, P. Adelhelm, Y.-S. Hu), Wiley-VCH GmbH, Weinheim, **2023**.

[5] C. Matei Ghimbeu, A. Beda, B. Réty, H. El Marouazi, A. Vizintin, B. Tratnik, L. Simonin, J. Michel, J. Abou-Rjeily, R. Dominko, "Review: Insights on Hard Carbon Materials for Sodium-Ion Batteries (SIBs): Synthesis – Properties – Performance Relationships", *Advanced Energy Materials* **2024**, *14*, 2303833.

[6] N. Tapia-Ruiz et al., "2021 roadmap for sodium-ion batteries", *Journal of Physics: Energy* **2021**, *3*, 031503.

[7] B. Sayahpour, H. Hirsh, S. Parab, L. H. B. Nguyen, M. Zhang, Y. S. Meng, "Perspective: Design of cathode materials for sustainable sodium-ion batteries", *MRS Energy & Sustainability* **2022**, *9*, 183–197.

[8] Y. Ishado, A. Inoishi, S. Okada, "Exploring Factors Limiting Three-Na+ Extraction from Na3V2(PO4)3", *Electrochemistry* **2020**, *88*, 457–462.

[9] S. Park, Z. Wang, Z. Deng, I. Moog, P. Canepa, F. Fauth, D. Carlier, L. Croguennec, C. Masquelier, J.-N. Chotard, "Crystal Structure of Na2V2(PO4)3, an Intriguing Phase Spotted in the Na3V2(PO4)3–Na1V2(PO4)3 System", *Chemistry of Materials* **2022**, *34*, 451–462.

[10] J. W. Gibbs, "On the equilibrium of heterogeneous substances", *American Journal of Science* **1878**, *3*, 441–458.

[11] H. von Helmholtz, *Die Thermodynamik chemischer Vorgänge*, **1882**.

[12] M. Bouty, “Sur un phénomène analogue au phénomène de Peltier”, *Journal de Physique Théorique et Appliquée* **1879**, *8*, 341–346.

[13] E. Lange, J. Monheim, “Über elektrolytische Peltier-Wärmen und ihre Messung mittels isotherm-adiabatischer Differentialcalorimetrie”, *Zeitschrift für Physikalische Chemie* **1930**, *150A*, 177–202.

[14] E. D. Eastman, “Thermodynamics of non-isothermal systems”, *Journal of the American Chemical Society* **1926**, *48*, 1482–1493.

[15] J. N. Agar in *Advances in Electrochemistry and Electrochemical Engineering, Vol. 3*, (Ed.: P. Delahay), Interscience Publishers, London, **1963**, pp. 31–121.

[16] A. J. Bard, L. R. Faulkner, *Electrochemical methods: fundamentals and applications*, 2nd ed, Wiley, New York, **2001**.

[17] J. M. Gottfried, R. Schuster in *Surface and interface science*, (Ed.: K. Wandelt), Wiley-VCH, Weinheim, Germany, **2015**, pp. 73–126.

[18] I. Källquist, “Combining Electrochemistry and Photoelectron Spectroscopy for the Study of Li-ion Batteries”, Ph.D. Thesis, Acta Universitatis Upsaliensis, Uppsala, **2021**.

[19] H. Hertz, “Ueber einen Einfluss des ultravioletten Lichtes auf die electrische Entladung”, *Annalen der Physik* **1887**, *267*, 983–1000.

[20] A. Einstein, “Über einen die Erzeugung und Verwandlung des Lichtes betreffenden heuristischen Gesichtspunkt”, *Annalen der Physik* **1905**, *322*, 132–148.

[21] *Handbook of X-ray photoelectron spectroscopy: a reference book of standard spectra for identification and interpretation of XPS data*, (Eds.: J. F. Moulder, W. F. Stickle, P. E. Sobol, K. D. Bomben, J. Chastain, R. C. King Jr., Physical Electronics, Incorporation), Physical Electronics, Eden Prairie, Minn., **1995**.

[22] K. Siegbahn, “ESCA: atomic, molecular and solid state structure studies by means of electron spectroscopy”, *Nova Acta Regiae Societatis Scientiarum Upsaliensis* **1967**.

[23] J. R. Dahn, R. R. Haering, “Entropy measurements on Li_xTiS_2”, *Canadian Journal of Physics* **1983**, *61*, 1093–1098.

[24] J. R. Dahn, W. R. McKinnon, J. J. Murray, R. R. Haering, R. S. McMillan, A. H. Rivers-Bowerman, “Entropy of the intercalation compound LixMo6Se8 from calorimetry of electrochemical cells”, *Physical review. B Condensed matter* **1985**, *32*, 3316–3318.

[25] R. Schuster, R. Rösch, A. E. Timm, “Microcalorimetry of Electrochemical Reactions at Submonolayer Conversions”, *Zeitschrift für Physikalische Chemie* **2007**, *221*, 1479–1491.

[26] K. D. Etzel, K. R. Bickel, R. Schuster, “A microcalorimeter for measuring heat effects of electrochemical reactions with submonolayer conversions”, *Review of Scientific Instruments* **2010**, *81*, 034101.

[27] S. Frittmann, V. Halka, C. Jaramillo, R. Schuster, “An improved sensor for electrochemical microcalorimetry, based on lithiumtantalate”, *Review of Scientific Instruments* **2015**, *86*, 064102.

[28] F. Karcher, “Mikrokalorimetrische Untersuchungen zu Kinetik und Thermodynamik der elektrochemischen Natrium- und Magnesiumabscheidung aus nichtwässrigen Systemen”, Ph.D. Thesis, Karlsruher Institut für Technologie (KIT), **2023**.

[29] F. Karcher, M. Uhl, T. Geng, T. Jacob, R. Schuster, “Entropic Contributions to Sodium Solvation and Solvent Stabilization upon Electrochemical Sodium deposition from Diglyme and Propylene Carbonate Electrolytes”, *Angewandte Chemie International Edition* **2023**, 202301253.

[30] R. W. Whatmore, “Pyroelectric devices and materials”, *Reports on Progress in Physics* **1986**, *49*, 1335.

[31] K. R. Bickel, K. D. Etzel, V. Halka, R. Schuster, “Microcalorimetric determination of heat changes caused by overpotential upon electrochemical Ag bulk deposition”, *Electrochimica Acta* **2013**, *112*, 801–812.

[32] P. Boudeville, A. Tallec, “Electrochemistry and calorimetry coupling: IV. Determination of electrochemical peltier heat”, *Thermochimica Acta* **1988**, *126*, 221–234.

[33] M. J. Schmid, “Wärmeeffekte bei der Lithiumabscheidung und -interkalation - Mikrokalorimetrische Untersuchungen zur Reaktionsentropie in Lithium/Graphit-Halbzellen”, Ph.D. Thesis, Karlsruher Institut für Technologie (KIT), **2014**.

[34] K. Palanisamy, S. Daboss, J. Romer, D. Schäfer, M. Rohnke, J. K. Flowers, S. Fuchs, H. S. Stein, M. Fichtner, C. Kranz, “Microscopic and Spectroscopic Analysis of the Solid Electrolyte Interphase at Hard Carbon Composite Anodes in 1 M NaPF6/Diglyme”, *Batteries & Supercaps* **2024**, *7*, e202300482.

[35] K. Gotoh, T. Yamakami, I. Nishimura, H. Kometani, H. Ando, K. Hashi, T. Shimizu, H. Ishida, “Mechanisms for overcharging of carbon electrodes in lithium-ion/sodium-ion batteries analysed by operando solid-state NMR”, *Journal of Materials Chemistry A* **2020**, *8*, 14472–14481.

[36] F. Karcher, M. Uhl, T. Geng, T. Jacob, R. Schuster, “Detection of Charge-Neutral Near-Equilibrium Processes at Na-Metal Electrodes by Electrochemical Microcalorimetry”, *Advanced Energy Materials* **2023**, 2302241.

[37] H. Wang, D. Wang, B. Li, S. Sun, "Improved methods to determine the electrochemical Peltier heat using a thermistor II: Extremum and optimization methods", *Journal of Electroanalytical Chemistry* **1995**, *392*, 21–25.

[38] K. Palanisamy, S. Daboss, D. Schäfer, M. Rohnke, L. Derr, M. Lang, R. Schuster, C. Kranz, "Spray-coated Hard Carbon Composite Anodes for Sodium-Ion Insertion", *Batteries & Supercaps* **2024**, *7*, e202300402.

[39] P. Stüble, C. Müller, J. Klemens, P. Scharfer, W. Schabel, M. Häringer, J. R. Binder, A. Hofmann, A. Smith, "Enabling Long-term Cycling Stability of Na3V2(PO4)3/C vs. Hard Carbon Full-cells", *Batteries & Supercaps* **2024**, *7*, e202300375.

[40] P. Stüble et al., "From Powder to Pouch Cell: Setting up a Sodium-Ion Battery Reference System Based on Na3V2(PO4)3/C and Hard Carbon", *Batteries & Supercaps* **2024**, *7*, e202400406.

[41] J. Fondard, E. Irisarri, C. Courrèges, M. R. Palacin, A. Ponrouch, R. Dedryvère, "SEI Composition on Hard Carbon in Na-Ion Batteries After Long Cycling: Influence of Salts (NaPF6, NaTFSI) and Additives (FEC, DMCF)", *Journal of The Electrochemical Society* **2020**, *167*, 070526.

[42] L. Derr, M. Lang, K. Palanisamy, C. Kranz, R. Schuster, "Role of Desolvation upon the Sodiation of Hard Carbon in Sodium-Ion Batteries: A Microcalorimetric Study of the Sodiation Entropy", *The Journal of Physical Chemistry C* **2025**, *129*, 4025–4031.

[43] L. Derr, S. Braun, K. Palanisamy, C. Kranz, R. Schuster, "Entropy Profiling of Hard Carbon/Na Metal Cells with Stepwise Temperature Changes: Influence of the Sodiation Kinetics on the Cell Voltage Response", *Batteries & Supercaps* **2026**, *in press.*

[44] X. Dou, I. Hasa, D. Saurel, C. Vaalma, L. Wu, D. Buchholz, D. Bresser, S. Komaba, S. Passerini, "Hard carbons for sodium-ion batteries: Structure, analysis, sustainability, and electrochemistry", *Materials Today* **2019**, *23*, 87–104.

[45] D. A. Stevens, J. R. Dahn, "High Capacity Anode Materials for Rechargeable Sodium-Ion Batteries", *Journal of The Electrochemical Society* **2000**, *147*, 1271.

[46] X. Chen, C. Liu, Y. Fang, X. Ai, F. Zhong, H. Yang, Y. Cao, "Understanding of the sodium storage mechanism in hard carbon anodes", *Carbon Energy* **2022**, *4*, 1133–1150.

[47] D. A. Stevens, J. R. Dahn, "The Mechanisms of Lithium and Sodium Insertion in Carbon Materials", *Journal of The Electrochemical Society* **2001**, *148*, A803.

[48] I. Escher, G. A. Ferrero, M. Goktas, P. Adelhelm, “In Situ (Operando) Electrochemical Dilatometry as a Method to Distinguish Charge Storage Mechanisms and Metal Plating Processes for Sodium and Lithium Ions in Hard Carbon Battery Electrodes”, *Advanced Materials Interfaces* **2022**, *9*, 2100596.

[49] C. Bommier, T. W. Surta, M. Dolgos, X. Ji, “New Mechanistic Insights on Na-Ion Storage in Nongraphitizable Carbon”, *Nano Letters* **2015**, *15*, 5888–5892.

[50] M. A. Reddy, M. Helen, A. Groß, M. Fichtner, H. Euchner, “Insight into Sodium Insertion and the Storage Mechanism in Hard Carbon”, *ACS Energy Letters* **2018**, *3*, 2851–2857.

[51] S. Qiu et al., “Manipulating Adsorption–Insertion Mechanisms in Nanostructured Carbon Materials for High-Efficiency Sodium Ion Storage”, *Advanced Energy Materials* **2017**, *7*, 1700403.

[52] P. Bai, Y. He, X. Zou, X. Zhao, P. Xiong, Y. Xu, “Elucidation of the Sodium-Storage Mechanism in Hard Carbons”, *Advanced Energy Materials* **2018**, *8*, 1703217.

[53] J. M. Stratford, A. K. Kleppe, D. S. Keeble, P. A. Chater, S. S. Meysami, C. J. Wright, J. Barker, M.-M. Titirici, P. K. Allan, C. P. Grey, “Correlating Local Structure and Sodium Storage in Hard Carbon Anodes: Insights from Pair Distribution Function Analysis and Solid-State NMR”, *Journal of the American Chemical Society* **2021**, *143*, 14274–14286.

[54] F. Linsenmann, D. Pritzl, H. A. Gasteiger, “Comparing the Lithiation and Sodiation of a Hard Carbon Anode Using In Situ Impedance Spectroscopy”, *Journal of The Electrochemical Society* **2021**, *168*, 010506.

[55] Y. Aniskevich, J. H. Yu, J.-Y. Kim, S. Komaba, S.-T. Myung, “Tracking Sodium Cluster Dynamics in Hard Carbon with a Low Specific Surface Area for Sodium-Ion Batteries”, *Advanced Energy Materials* **2024**, *14*, 2304300.

[56] K. Schutjajew, T. Tichter, J. Schneider, M. Antonietti, C. Roth, M. Oschatz, “Insights into the sodiation mechanism of hard carbon-like materials from electrochemical impedance spectroscopy”, *Physical Chemistry Chemical Physics* **2021**, *23*, 11488–11500.

[57] X. Li, X. Zeng, T. Ren, J. Zhao, Z. Zhu, S. Sun, Y. Zhang, “The transport properties of sodium-ion in the low potential platform region of oatmeal-derived hard carbon for sodium-ion batteries”, *Journal of Alloys and Compounds* **2019**, *787*, 229–238.

[58] R. Dong, L. Zheng, Y. Bai, Q. Ni, Y. Li, F. Wu, H. Ren, C. Wu, “Elucidating the Mechanism of Fast Na Storage Kinetics in Ether Electrolytes for Hard Carbon Anodes”, *Advanced Materials* **2021**, *33*, 2008810.

[59] R. Väli, A. Jänes, E. Lust, “Alkali-Metal Insertion Processes on Nanospheric Hard Carbon Electrodes: An Electrochemical Impedance Spectroscopy Study”, *Journal of The Electrochemical Society* **2017**, *164*, E3429.

[60] Z. Lv, T. Li, X. Hou, C. Wang, H. Zhang, J. Yan, Q. Zheng, X. Li, “Solvation structure and solid electrolyte interface engineering for excellent Na+ storage performances of hard carbon with the ether-based electrolytes”, *Chemical Engineering Journal* **2022**, *430*, 133143.

[61] M. P. Mercer, S. Affleck, E. M. Gavilán-Arriazu, A. A. Zülke, P. A. Maughan, S. Trivedi, M. Fichtner, A. R. Munnangi, E. P. M. Leiva, H. E. Hoster, “Sodiation Of Hard Carbon: How Separating Enthalpy And Entropy Contributions Can Find Transitions Hidden In The Voltage Profile”, *ChemPhysChem* **2022**, *23*, 202100748.

[62] M. P. Mercer, M. Nagarathinam, E. M. Gavilán-Arriazu, A. Binjrajka, S. Panda, H. Au, M. Crespo-Ribadeneyra, M.-M. Titirici, E. P. M. Leiva, H. E. Hoster, “Sodiation energetics in pore size controlled hard carbons determined via entropy profiling”, *Journal of Materials Chemistry A* **2023**, *11*, 6543–6555.

[63] J. Huang, C. Delacourt, P. Desai, J.-M. Tarascon, “Operando Entropy Profiling of Sodium-Ion Batteries via Optical Fiber Sensing for Thermal Management and Ageing Monitoring”, *Journal of The Electrochemical Society* **2024**, *171*, 030516.

[64] F. Wei, P. Li, Q. Zhang, G. Shao, J. Mao, “Entropy Change Characteristics for Sodium Ion Half/Full Cells Based on Na3V2(PO4)3 and Hard Carbon Materials”, *Journal of The Electrochemical Society* **2022**, *169*, 050503.

[65] D. Schäfer et al., “Multiscale Investigation of Sodium-Ion Battery Anodes: Analytical Techniques and Applications”, *Advanced Energy Materials* **2024**, *14*, 2302830.

[66] G. G. Eshetu, T. Diemant, M. Hekmatfar, S. Grugeon, R. J. Behm, S. Laruelle, M. Armand, S. Passerini, “Impact of the electrolyte salt anion on the solid electrolyte interphase formation in sodium ion batteries”, *Nano Energy* **2019**, *55*, 327–340.

[67] M. Carboni, J. Manzi, A. R. Armstrong, J. Billaud, S. Brutti, R. Younesi, “Analysis of the Solid Electrolyte Interphase on Hard Carbon Electrodes in Sodium-Ion Batteries”, *ChemElectroChem* **2019**, *6*, 1745–1753.

[68] R. Mogensen, D. Brandell, R. Younesi, “Solubility of the Solid Electrolyte Interphase (SEI) in Sodium Ion Batteries”, *ACS Energy Letters* **2016**, *1*, 1173–1178.

[69] C. Bommier, D. Leonard, Z. Jian, W. F. Stickle, P. A. Greaney, X. Ji, “New Paradigms on the Nature of Solid Electrolyte Interphase Formation and Capacity Fading of Hard Carbon Anodes in Na-Ion Batteries”, *Advanced Materials Interfaces* **2016**, *3*, 1600449.

[70] R. P. Seward, E. C. Vieira, “The Dielectric Constants of Ethylene Carbonate and of Solutions of Ethylene Carbonate in Water, Methanol, Benzene and Propylene Carbonate”, *The Journal of Physical Chemistry* **1958**, *62*, 127–128.

[71] D. R. Lide, *CRC Handbook of chemistry and physics: 2005-2006 a ready-reference book of chemical and physical data*, 86th ed, CRC press Taylor & Francis Group, Boca Raton New York Washington, **2005**.

[72] D. Morales, L. G. Chagas, D. Paterno, S. Greenbaum, S. Passerini, S. Suarez, “Transport studies of NaPF6 carbonate solvents-based sodium ion electrolytes”, *Electrochimica Acta* **2021**, *377*, 138062.

[73] M. J. Schmid, K. R. Bickel, P. Novák, R. Schuster, “Microcalorimetric measurements of the solvent contribution to the entropy changes upon electrochemical lithium bulk deposition”, *Angewandte Chemie International Edition* **2013**, *52*, 13233–13237.

[74] G. Åvall, G. A. Ferrero, K. A. Janßen, M. Exner, Y. Son, P. Adelhelm, “In Situ Pore Formation in Graphite Through Solvent Co-Intercalation: A New Model for The Formation of Ternary Graphite Intercalation Compounds Bridging Batteries and Supercapacitors”, *Advanced Energy Materials* **2023**, *13*, 2301944.

[75] N. Jiang, L. Chen, H. Jiang, Y. Hu, C. Li, “Introducing the Solvent Co-Intercalation Mechanism for Hard Carbon with Ultrafast Sodium Storage”, *Small* **2022**, *18*, 2108092.

[76] P. Simon, Y. Gogotsi, “Materials for electrochemical capacitors”, *Nature Materials* **2008**, *7*, 845–854.

[77] Y. Li et al., “Origin of fast charging in hard carbon anodes”, *Nature Energy* **2024**, *9*, 134–142.

[78] D. R. Lide, *CRC Handbook of chemistry and physics : a ready-reference book of chemical and physical data*, 71st ed., CRC Press, **1990**.

[79] M. A. Villamañan, C. Casanova, G. Roux-Desgranges, J.-P. E. Grolier, “Thermochemical behaviour of mixtures of *n*-alcohol + aliphatic ether: heat capacities and volumes at 298.15 K”, *Thermochimica Acta* **1982**, *52*, 279–283.

[80] I. M. Bernstein, *Handbook of stainless steels*, (Ed.: D. Peckner), McGraw-Hill, New York, **1977**.

[81] A. Cruz-Orea, F. Sánchez-Sinencio, M. A. Algatti, J. L. Jiménez-Pérez, Z. N. Correa-Pacheco, A. García-Quiroz, “Thermal characterization of Diglyme by using photopyroelectric spectroscopy”, *Trends in Heat and Mass Transfer* **2013**, *13*, 51–55.

[82] J. Speight, *Lange’s Handbook of Chemistry, Seventeenth Edition*, 17th edition, McGraw-Hill Education, New York, N.Y, **2016**.

[83] C. F. Riadigos, R. Iglesias, M. A. Rivas, T. P. Iglesias, “Permittivity and density of the systems (monoglyme, diglyme, triglyme, or tetraglyme + *n*-heptane) at several temperatures”, *The Journal of Chemical Thermodynamics* **2011**, *43*, 275–283.

[84] W. Schmickler, E. Santos, *Interfacial electrochemistry*, Second edition, Springer, Berlin, **2010**.

[85] Y. Niu et al., “Deciphering and Enhancing Rate-Determining Step of Sodium Deposition towards Ultralow-Temperature Sodium Metal Batteries”, *Angewandte Chemie International Edition* **2025**, *64*, e202416720.

[86] G. Åvall, P. Adelhelm, “Solution to dissolution”, *Nature Energy* **2022**, *7*, 682–683.

[87] L. A. Ma, A. J. Naylor, L. Nyholm, R. Younesi, “Strategies for Mitigating Dissolution of Solid Electrolyte Interphases in Sodium-Ion Batteries”, *Angewandte Chemie International Edition* **2021**, *60*, 4855–4863.

[88] A. Ponrouch, R. Dedryvère, D. Monti, A. E. Demet, J. M. A. Mba, L. Croguennec, C. Masquelier, P. Johansson, M. R. Palacín, “Towards high energy density sodium ion batteries through electrolyte optimization”, *Energy & Environmental Science* **2013**, *6*, 2361–2369.

[89] L. Chen, B. Kishore, M. Walker, C. E. J. Dancer, E. Kendrick, “Nanozeolite ZSM-5 electrolyte additive for long life sodium-ion batteries”, *Chemical Communications* **2020**, *56*, 11609–11612.

[90] M. Dahbi, T. Nakano, N. Yabuuchi, S. Fujimura, K. Chihara, K. Kubota, J.-Y. Son, Y.-T. Cui, H. Oji, S. Komaba, “Effect of Hexafluorophosphate and Fluoroethylene Carbonate on Electrochemical Performance and the Surface Layer of Hard Carbon for Sodium-Ion Batteries”, *ChemElectroChem* **2016**, *3*, 1856–1867.

[91] Z. Zhu, F. Liang, Z. Zhou, X. Zeng, D. Wang, P. Dong, J. Zhao, S. Sun, Y. Zhang, X. Li, “Expanded biomass-derived hard carbon with ultra-stable performance in sodium-ion batteries”, *Journal of Materials Chemistry A* **2018**, *6*, 1513–1522.

[92] S. Alvin, D. Yoon, C. Chandra, H. S. Cahyadi, J.-H. Park, W. Chang, K. Y. Chung, J. Kim, “Revealing sodium ion storage mechanism in hard carbon”, *Carbon* **2019**, *145*, 67–81.

[93] L. Gehrlein, C. Njel, F. Jeschull, J. Maibach, “From Additive to Cosolvent: How Fluoroethylene Carbonate Concentrations Influence Solid–Electrolyte Interphase Properties and Electrochemical Performance of Si/Gr Anodes”, *ACS Applied Energy Materials* **2022**, *5*, 10710–10720.

[94] Z. Lu, H. Yang, Y. Guo, H. Lin, P. Shan, S. Wu, P. He, Y. Yang, Q.-H. Yang, H. Zhou, “Consummating ion desolvation in hard carbon anodes for reversible sodium storage”, *Nature Communications* **2024**, *15*, 3497.

[95] J. R. Fitzpatrick, B. E. Murdock, P. K. Thakur, T.-L. Lee, S. Fearn, A. J. Naylor, D. Biswas, N. Tapia-Ruiz, “An in-depth Study of the Solid Electrolyte Interphase Compositional Evolution in Sodium-Ion Batteries: Unravelling the Effects of a Na Metal Counter Electrode on the SEI”, *Advanced Science* **2025**, *12*, e04717.

[96] J. Maibach, F. Lindgren, H. Eriksson, K. Edström, M. Hahlin, “Electric Potential Gradient at the Buried Interface between Lithium-Ion Battery Electrodes and the SEI Observed Using Photoelectron Spectroscopy”, *The Journal of Physical Chemistry Letters* **2016**, *7*, 1775–1780.

[97] C. J. Powell, A. Jablonski, *NIST Electron Inelastic-Mean-Free-Path Database*, Version 1.2, National Institute of Standards and Technology, Gaithersburg, **2010**.

[98] K. Momma, F. Izumi, “VESTA 3 for three-dimensional visualization of crystal, volumetric and morphology data”, *Journal of Applied Crystallography* **2011**, *44*, 1272–1276.

[99] J.-N. Chotard, G. Rousse, R. David, O. Mentré, M. Courty, C. Masquelier, “Discovery of a Sodium-Ordered Form of Na3V2(PO4)3 below Ambient Temperature”, *Chemistry of Materials* **2015**, *27*, 5982–5987.

[100] T. Akçay, M. Häringer, K. Pfeifer, J. Anhalt, J. R. Binder, S. Dsoke, D. Kramer, R. Mönig, “Na3V2(PO4)3 - A Highly Promising Anode and Cathode Material for Sodium-Ion Batteries”, *ACS Applied Energy Materials* **2021**, *4*, 12688–12695.

[101] Z. Jian et al., “Superior Electrochemical Performance and Storage Mechanism of Na3V2(PO4)3 Cathode for Room-Temperature Sodium-Ion Batteries”, *Advanced Energy Materials* **2013**, *3*, 156–160.

[102] Z. Jian et al., “Atomic Structure and Kinetics of NASICON NaxV2(PO4)3 Cathode for Sodium-Ion Batteries”, *Advanced Functional Materials* **2014**, *24*, 4265–4272.

[103] Q. Wang, M. Zhang, C. Zhou, Y. Chen, “Concerted Ion-Exchange Mechanism for Sodium Diffusion and Its Promotion in Na3V2(PO4)3 Framework”, *The Journal of Physical Chemistry C* **2018**, *122*, 16649–16654.

[104] Z. Jian, L. Zhao, H. Pan, Y.-S. Hu, H. Li, W. Chen, L. Chen, “Carbon coated Na3V2(PO4)3 as novel electrode material for sodium ion batteries”, *Electrochemistry Communications* **2012**, *14*, 86–89.

[105] I. U. Mohsin, L. Schneider, M. Häringer, C. Ziebert, M. Rohde, W. Bauer, H. Ehrenberg, H. J. Seifert, “Heat generation and degradation mechanisms studied on Na3V2(PO4)3/C positive electrode material in full pouch / coin cell assembly”, *Journal of Power Sources* **2022**, *545*, 231901.

[106] L. U. Subasinghe, C. Wang, S. R. Gajjela, M. Law, B. Manikandan, P. Balaya, “A study on heat generation characteristics of Na3V2(PO4)3 cathode and hard carbon anode-based sodium-ion cells”, *Journal of Thermal Analysis and Calorimetry* **2022**, *147*, 8631–8649.

[107] C. H. Hamann, W. Vielstich, *Elektrochemie*, 4. Auflage, Wiley-VCH, Weinheim, **2005**.

[108] L. M. Peter, W. Dürr, P. Bindra, H. Gerischer, “The influence of alkali metal cations on the rate of the $Fe(CN)_6{}^{4-}/Fe(CN)_6{}^{3-}$ electrode process”, *Journal of Electroanalytical Chemistry and Interfacial Electrochemistry* **1976**, *71*, 31–50.

[109] M. Schönig, R. Schuster, “Sensitive and fast measurement of surface temperature with a thermogalvanic cell”, *Applied Physics Letters* **2020**, *116*, 091601.

[110] D. Meschede, *Gerthsen Physik*, 25. Aufl. 2015, Springer Berlin Heidelberg, Berlin, Heidelberg, **2015**.

[111] J. Nanda, S. K. Martha, W. D. Porter, H. Wang, N. J. Dudney, M. D. Radin, D. J. Siegel, “Thermophysical properties of LiFePO4 cathodes with carbonized pitch coatings and organic binders: Experiments and first-principles modeling”, *Journal of Power Sources* **2014**, *251*, 8–13.

[112] S. C. Chen, C. C. Wan, Y. Y. Wang, “Thermal analysis of lithium-ion batteries”, *Journal of Power Sources* **2005**, *140*, 111–124.

[113] S. W. Baek, M. Saber, A. Van der Ven, L. Pilon, “Thermodynamic Analysis and Interpretative Guide to Entropic Potential Measurements of Lithium-Ion Battery Electrodes”, *The Journal of Physical Chemistry C* **2022**, *126*, 6096–6110.

[114] W. R. McKinnon, J. R. Dahn, J. J. Murray, R. R. Haering, R. S. McMillan, A. H. Rivers-Bowerman, “Entropy of intercalation compounds. II. Calorimetry of electrochemical cells of the Chevrel compound LixMo6Se8 for $0 \leq x \leq 4$”, *Journal of Physics C: Solid State Physics* **1986**, *19*, 5135.

[115] T. Zhang, M. Sotoudeh, X. Yao, A. Groß, M. Kamlah, “3D chemo-mechanical modeling of microstructure evolution and anisotropic deformation in $\mathrm{Na_xV_2(PO_4)_3}$ cathode particles for sodium-ion batteries”, *International Journal of Solids and Structures* **2025**, *320*, 113525.

[116] K. E. Thomas, J. Newman, “Heats of mixing and of entropy in porous insertion electrodes”, *Journal of Power Sources* **2003**, *119-121*, 844–849.

[117] K. E. Thomas, J. Newman, “Thermal Modeling of Porous Insertion Electrodes”, *Journal of The Electrochemical Society* **2003**, *150*, A176.

[118] D. Chalise, W. Lu, V. Srinivasan, R. Prasher, “Heat of Mixing During Fast Charge/Discharge of a Li-Ion Cell: A Study on NMC523 Cathode”, *Journal of The Electrochemical Society* **2020**, *167*, 090560.

[119] R. Mehta, A. Gupta, “Significance of heat of mixing analysed using a pseudo two-dimensional thermo-electrochemical model of lithium-ion cells”, *Electrochimica Acta* **2024**, *475*, 143509.

List of Abbreviations

CC	constant current
CE	counter electrode
CV	cyclic voltammogram
DEC	diethyl carbonate
DFT	density functional theory
DMC	dimethyl carbonate
DBBB	2,5-di-tertbutyl-1,4-bis(methoxyethoxy)benzene
EC	ethylene carbonate
EIS	electrochemical impedance spectroscopy
FEC	fluoroethylene carbonate
FWHM	full width at half maximum
GITT	galvanostatic intermittent titration technique
HC	hard carbon
IMFP	inelastic mean free path
LIB	lithium-ion battery
NMR	nuclear magnetic resonance
NVP	$Na_3V_2(PO_4)_3$
NVP/C	$Na_3V_2(PO_4)_3/C$
OC	open circuit
OCV	open circuit voltage
PC	propylene carbonate
PEEK	polyether ether ketone
PDF	pair distribution function

POLiS	Post Lithium Storage
PVDF	polyvinylidene fluoride
RE	reference electrode
SEI	solid electrolyte interphase
SIB	sodium-ion battery
SoC	state of charge
SAXS	small-angle X-ray scattering
TEM	transmission electron microscopy
WE	working electrode
WAXS	wide-angle X-ray scattering
XPS	X-ray photoelectron spectroscopy
XRD	X-ray diffraction

C

Appendix

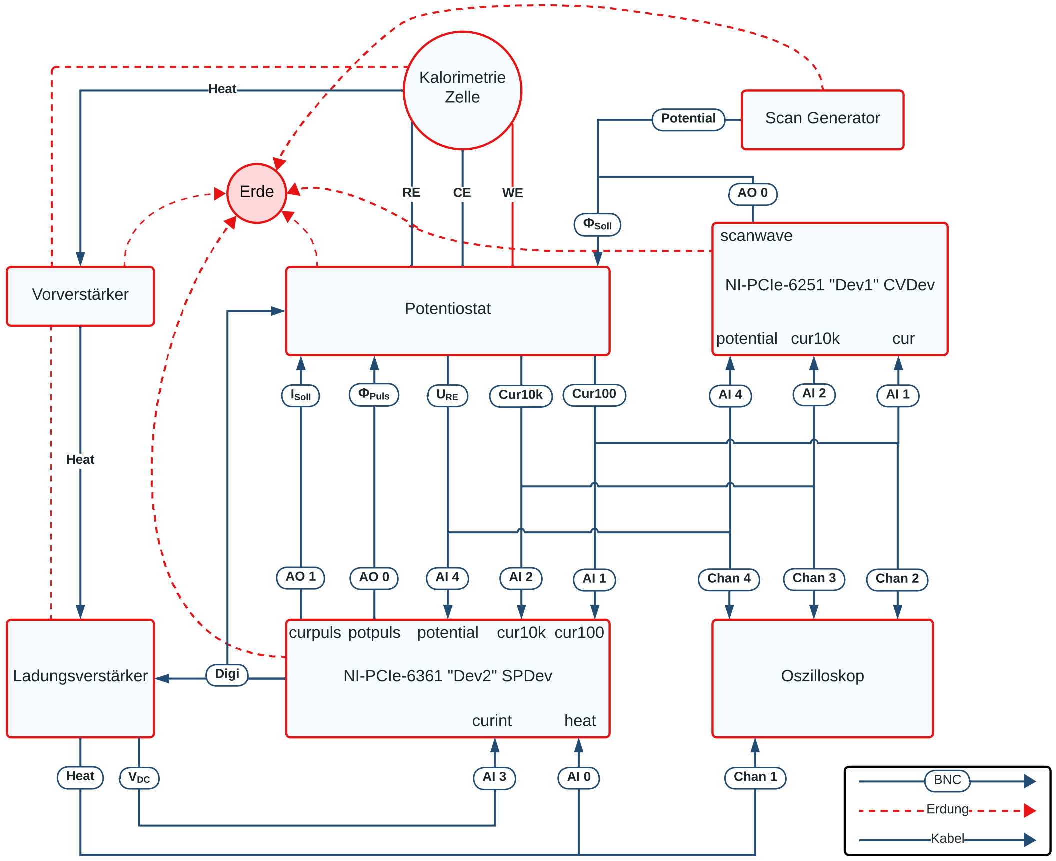

Figure C.1: Block diagram of the electrochemical microcalorimeter setup.

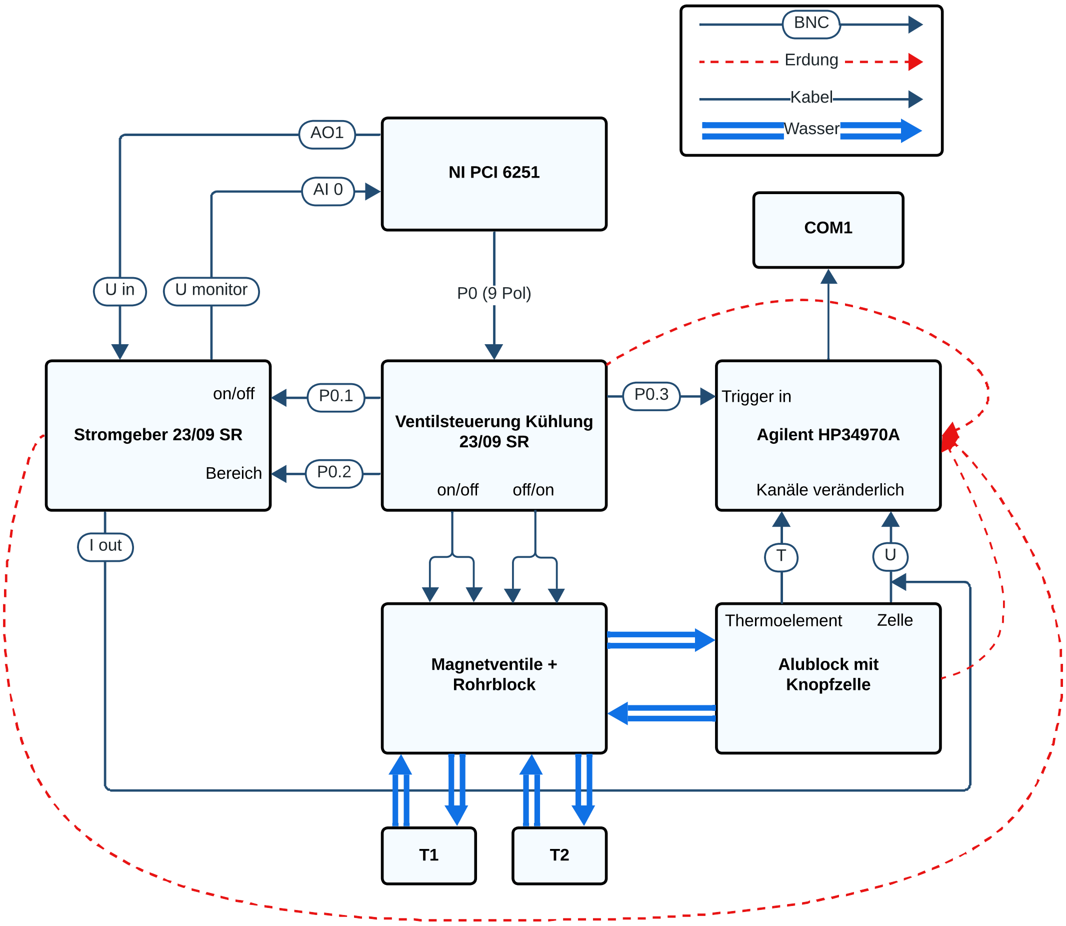

Figure C.2: Block diagram of the setup for the temperature step experiments.

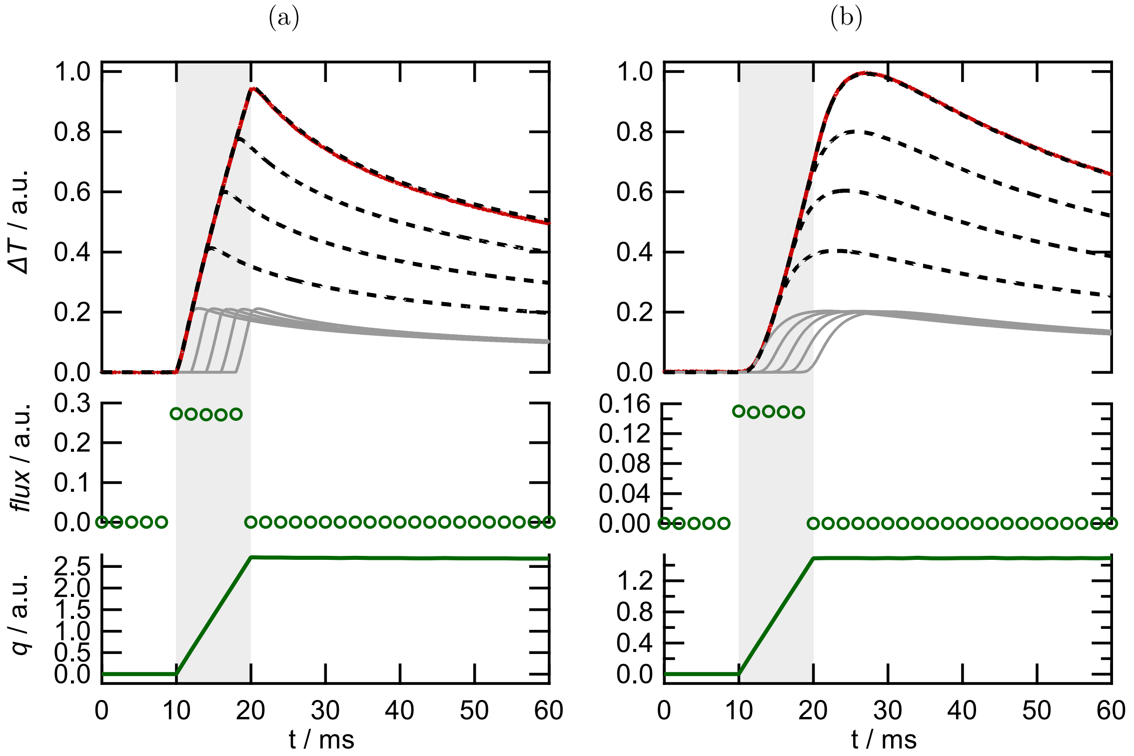

Figure C.3: Illustration of the disentanglement of the temperature transient obtained by 10 ms laser irradiation of an (a) Au on sapphire electrode (ca. 200 nm Au on a 50 µm thick sapphire) in water and a (b) thin HC electrode (20 µm) in 1 M $NaClO_4$/PC+FEC electrolyte solution. The measured signal (red) is reconstructed with the sum of five temperature transients obtained by 2 ms laser irradiation of the WE. As expected, the flux (green circles) is nonzero only during the 10 ms laser pulse and the heat *q* (green line) increases only during the 10 ms laser pulse.

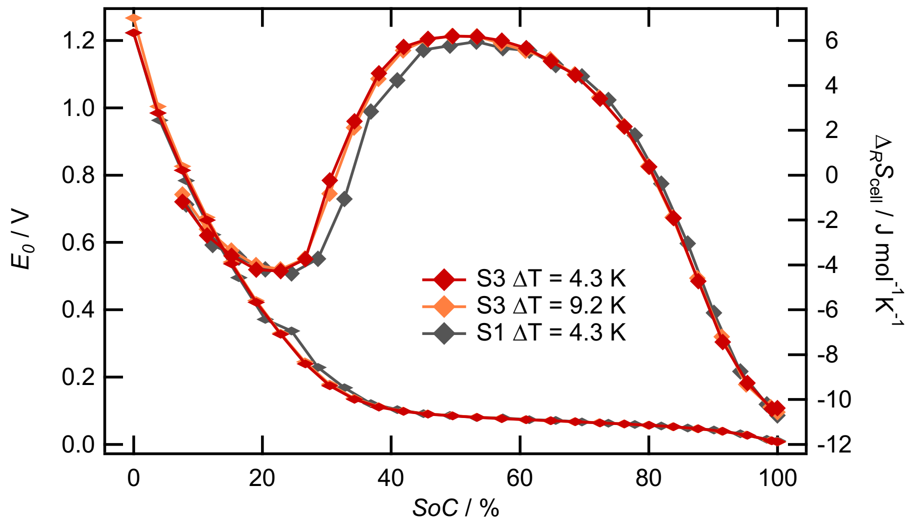

Figure C.4: Comparison of the cell reaction entropy and E_0 of two different HC/Na metal cells (S1 and S3) and of two different heights of the applied temperature steps in the charging cycle.

	Pristine		**Diglyme A**		**Diglyme B**		**Diglyme C**		**Diglyme D**	
Assignment	BE	FWHM	BE	FWHM	BE	FWHM	BE	FWHM	BE	FWHM
sp^{2}C	284.2	0.8	283.9	0.8	283.5	0.8	283.2	0.8	283.2	0.8
C–H/C–C	285.0	1.1	285.0	1.2	285.0	1.1	285.0	1.4	285.0	1.3
C–O	286.5	1.6	287.1	1.6	286.9	1.6	286.9	1.1	286.8	1.2
C=O	288.4	1.6	289.2	1.0	289.0	1.0	288.8	1.0	288.6	1.2
CO_3	-	-	290.7	1.1	290.5	1.2	290.3	1.0	290.2	1.0
Na_2O	-	-	530.7	1.5	530.5	1.5	530.3	1.1	530.2	1.1
C=O/CO_3	531.7	1.6	532.5	1.5	532.1	1.6	532.0	1.3	531.9	1.4
C–O	533.2	1.6	534.0	1.6	533.8	1.5	533.7	1.5	533.6	1.4
Na KLL	536.2	3	537.1	2.4	536.8	2.3	536.6	2.5	536.1	2.6

Table C.1: Fitting results of the XP spectra of the C 1s and the O 1s region of the Diglyme samples shown in Figure 4.31 (a) and 4.33 (a). All values are given in eV.

	Pristine		**Carbonate A**		**Carbonate B**		**Carbonate C**		**Carbonate D**	
Assignment	BE	FWHM	BE	FWHM	BE	FWHM	BE	FWHM	BE	FWHM
sp^2C	284.2	0.8	284.2	0.8	283.3	0.8	282.9	0.8	282.7	0.8
C–H/C–C	285.0	1.1	285.0	1.2	285.0	1.2	285.0	1.3	285.0	1.4
C–O	286.5	1.6	287.1	1.4	286.9	1.6	286.8	1.6	286.9	1.5
C=O	288.4	1.6	288.7	1.0	288.7	1.6	288.8	1.6	288.7	1.6
CO_3	-	-	289.8	1.6	290.2	1.5	290.2	1.2	290.3	1.2
FEC decomp.	-	-	291.4	1.5	291.6	1.0	291.3	1.6	291.4	0.9
Na_2O	-	-	530.0	1.1	530.4	1.6	530.4	1.4	530.6	1.5
C=O/CO_3	531.7	1.6	532.0	1.5	531.8	1.6	531.8	1.6	531.8	1.5
C–O	533.2	1.6	533.6	1.5	533.4	1.6	533.3	1.6	533.3	1.5
O–F_x	-	-	534.8	1.5	534.6	1.6	534.2	1.6	534.2	1.5
Na KLL	536.2	3.0	537.3	3.0	536.9	3.0	536.4	2.7	537.2	2.7

Table C.2: Fitting results of the XP spectra of the C 1s and the O 1s region of the Carbonate cells shown in Figure 4.31 (b) and 4.33 (b). All values are given in eV.

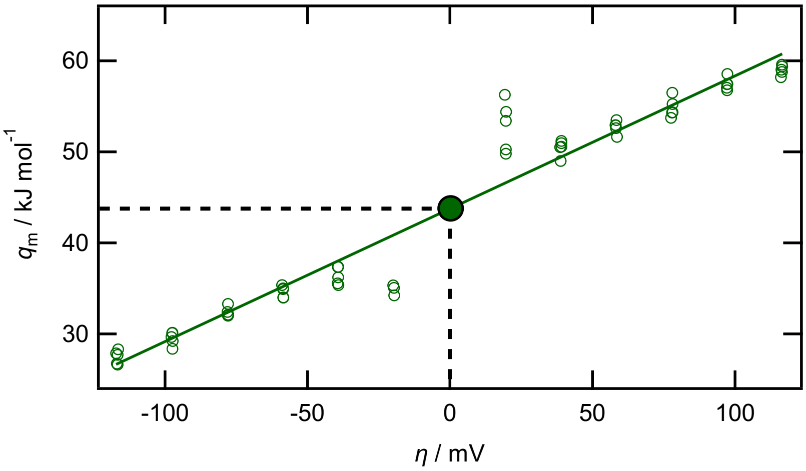

Figure C.5: Molar heat obtained for the charging/discharging of NVP/C in 1 M $NaPF_6$/EC,PC+FEC at an OCV of 3.315 V (SoC 49 %) at $t = 200$ ms with current pulses with alternating amplitudes (±50 µA to ±300 µA). With interpolation to $\eta = 0$ V the reversibly exchanged molar heat upon discharging of NVP/C at this SoC is found.

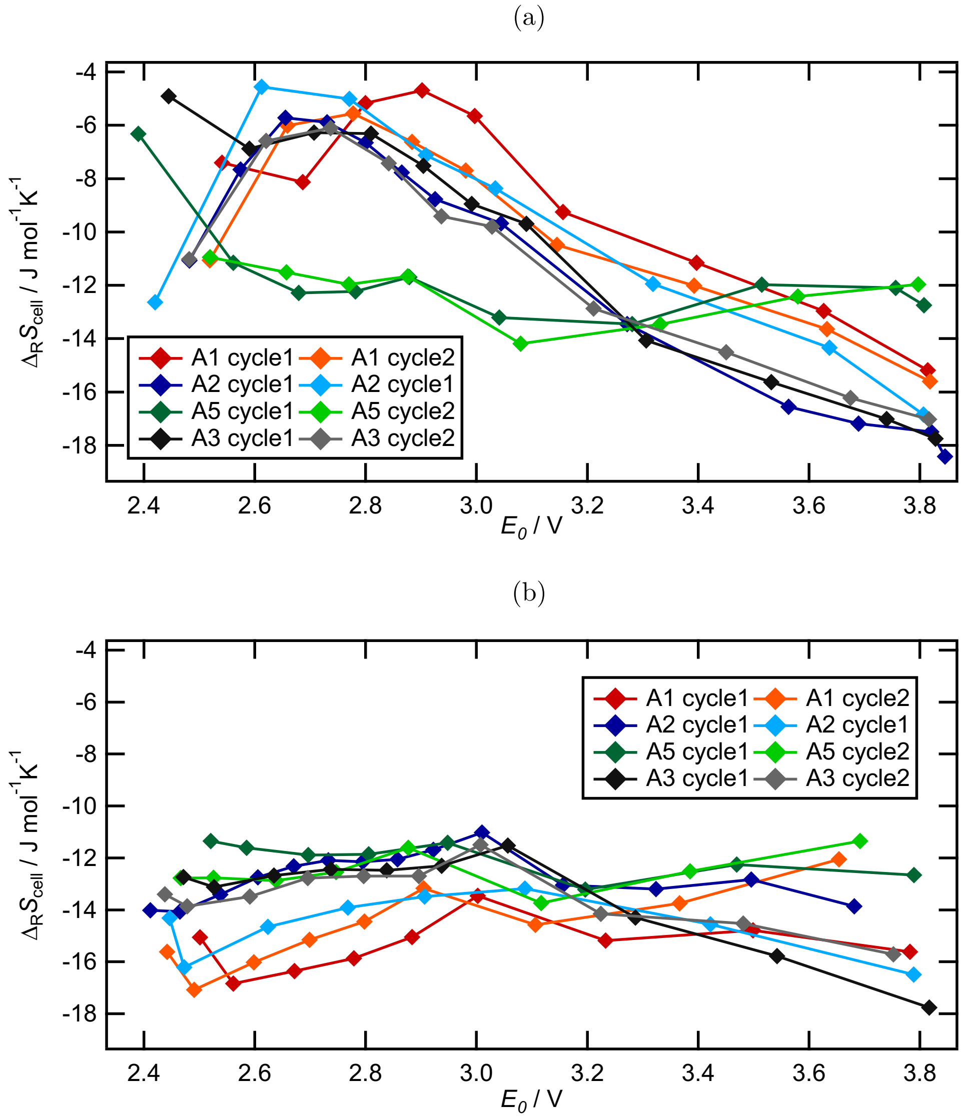

Figure C.6: Cell reaction entropy $\Delta_R S_{cell}$ vs the equilibrium cell voltage E_0 of four NVP/C|HC coin cells (A1, A2, A3 and A5) with 1 M $NaPF_6$/EC,PC in (a) charging and (b) discharging cycles.

D

List of Figures

E

List of Tables

F

List of Publications

[1] K. Palanisamy, S. Daboss, D. Schäfer, M. Rohnke, L. Derr, M. Lang, R. Schuster, C. Kranz, “Spray-coated Hard Carbon Composite Anodes for Sodium-Ion Insertion”, *Batteries & Supercaps* **2024**, 7, e202300402, DOI 10.1002/batt.202300402.

[2] D. Schäfer, K. Hankins, M. Allion, U. Krewer, F. Karcher, L. Derr, R. Schuster, J. Maibach, S. Mück, D. Kramer, R. Mönig, F. Jeschull, S. Daboss, T. Philipp, G. Neusser, J. Romer, K. Palanisamy, C. Kranz, F. Buchner, R. J. Behm, A. Ahmadian, C. Kübel, I. Mohammad, A. Samoson, R. Witter, B. Smarsly, M. Rohnke, “Multiscale Investigation of Sodium-Ion Battery Anodes: Analytical Techniques and Applications”, *Advanced Energy Materials* **2024**, 14, 2302830, DOI 10.1002/aenm.202302830.

[3] L. Derr, M. Lang, K. Palanisamy, C. Kranz, R. Schuster, “Role of Desolvation upon the Sodiation of Hard Carbon in Sodium-Ion Batteries: A Microcalorimetric Study of the Sodiation Entropy”, *The Journal of Physical Chemistry C* **2025**, 129, 4025–4031, DOI 10.1021/acs.jpcc.4c08586.

[4] L. Derr, S. Braun, K. Palanisamy, C. Kranz, R. Schuster, “Entropy Profiling of Hard Carbon/Na Metal Cells with Stepwise Temperature Changes: Influence of the Sodiation Kinetics on the Cell Voltage Response”, *Batteries & Supercaps* **2026**, *in press*, DOI 10.1002/batt.202500924.

[5] Q. Liu, L. King, H. Wagner, A. Križan, L. Derr, K. L. Browning, G. M. Veith, T. Ericson, R. Temperton, M. Hahlin, "A simple approach for operando interface probing for batteries: combining scanning APXPS with spectroscopic recognition", *ACS Applied Materials & Interfaces* **2026**, *in review.*

G

Acknowledgements

An erster Stelle möchte ich mich bei Prof. Dr. Rolf Schuster für die große Unterstüzung während meiner Promotion bedanken. Dafür, dass Ihre Tür immer für Diskussionen offen stand und Sie sich bei elektrotechnischen Problemen nicht nur um deren Lösung, sondern auch um mein Verständnis dieser gekümmert haben. Für die freundliche Übernahme des Korreferats danke ich Prof. Dr. Helmut Ehrenberg.

Außerdem danke ich all meinen aktuellen und ehemaligen Kolleg:innen im 7. Stocks des IPCs: Agnes, Bruna, Daniel, Detlef, Franzi, Janet, Jens, Karolin, Katarina, Katrin, Lisa, Marcel, Marco und Steffen. Jede:r von euch hat zum Gelingen dieser Arbeit auf unterschiedlichste Art und Weise beigetragen. Für verschiedene Messungen im Rahmen von Bachelor- und Vertieferarbeiten danke ich Steffen, Sebastian und Jonas.

Diese Arbeit wäre ohne die Kooperationen, die mich mit Elektrodenmaterialien und Elektrolytlösungen versorgt haben, nicht möglich gewesen. Insbesondere bedanke ich mich bei Krishnaveni Palanisamy und Christine Kranz für die gute Zusammenarbeit. Außerdem bedanke ich mich bei Sven Daboss, Salimeh Saleh, Pirmin Stüble, Andreas Hofmann und allen weiteren Partnern aus dem POLiS Cluster. Der feinmechanischen Werkstatt, also Torsten Franzke, Dieter Waltz, Martin Segner und Eric Fuhrmann, danke ich für das Lösen aller technischen Probleme.

For my research stay at Uppsala University in Sweden, I would like thank Maria Hahlin for hosting me, Qianhui for helping me with the XPS measurements and Darius for being my deskmate. Tack så mycket, 谢谢 and ممنون!

Zu guter Letzt möchte ich mich bei meinen Eltern und meinen Brüdern für die Unterstützung während des gesamten Studiums und der Promotion bedanken. Meiner Verlobten Sophia danke ich dafür, dass sie immer für mich da ist und dass sie mich, wenn nötig, aus der Welt der Ionen und Elektronen in die, in der ein Akku halt voll oder leer ist, zurückgeholt hat.

"our verbal machinery has no built-in cutoff"
P.W. Bridgman